

Es ist schwieriger, eine vorgefasste Meinung zu zertrümmern als ein Atom.

Albert Einstein

New applications for slowing down of high-energy heavy ions

Inauguraldissertation

zur

Erlangung des Doktorgrades

der Naturwissenschaften

der Justus-Liebig-Universität Gießen

Fachbereich 07

Physik, Mathematik und Informatik, Geographie

vorgelegt von

Michael Maier

aus München

Darmstadt, den 7. Juli 2004

Abstract

In this thesis the charge-state distribution and energy loss of relativistic nickel and xenon ions in the energy range from 30 to 500 MeV/u were studied. The experiments were performed using the magnetic spectrometer FRS at GSI. In several experimental runs the slowing down data for nickel and xenon ions in various target materials ranging from $Z = 4$ to 79 was measured. The main goal of this experiment was to obtain slowing-down data above 30 MeV/u to improve predictions in this energy regime.

Furthermore a technique to reduce the momentum spread of relativistic nickel and cobalt fragments, called “range focusing”, was investigated. The range-focusing technique was examined to improve the efficiency of stopping relativistic ion beams produced in fragmentation reactions in thin layers of matter. This technique, to thermalize ions for high precision experiments is an essential part for low energy experiments of future in-flight separators.

Finally the present status of the development and assembly of a setup for stopping relativistic ions using the range focusing technique, the FRS ion catcher, is described in the last part of this thesis.

Index

Abstract	4
Index	5
1 Introduction	7
2 Theory	11
2.1 <i>Production mechanisms for exotic nuclear beams</i>	11
2.1.1 Fragmentation	12
2.1.2 Fission	14
2.1.3 Fusion	16
2.2 <i>Separation methods</i>	16
2.2.1 ISOL method	18
2.2.2 In-flight method	19
2.2.3 The new hybrid separation method	21
2.3 <i>Slowing down of heavy ions in matter</i>	23
2.3.1 Charge-state distributions	23
2.3.1.1 Ionization	24
2.3.1.2 Electron capture	25
2.3.1.3 The computer code GLOBAL	26
2.3.2 Energy loss	27
2.3.2.1 Basic quantities	27
2.3.2.2 Classical calculation	29
2.3.2.3 Quantum mechanical treatment	31
2.3.2.4 Energy loss at medium velocities	33
2.3.2.5 Energy loss at low velocities	34
2.3.2.6 The computer code ATIMA	35
3 Experiment	36
3.1 <i>Slowing down experiment with ^{58}Ni and ^{136}Xe ions</i>	36
3.1.1 Ion-optical mode	36
3.1.2 Detectors	37
3.1.2.1 Multi sampling ionization chamber MUSIC	38
3.1.2.2 Multi wire proportional chambers	38
3.1.3 Targets	39
3.1.4 Data analysis	41
3.1.4.1 Charge-state distribution	41
3.1.4.2 Energy loss	43
3.1.4.3 Stopping power	47
3.1.4.4 Energy-loss straggling	49
3.2 <i>Range focusing of relativistic ^{56}Ni and ^{54}Co ions</i>	57
3.2.1 The degrader system	59
3.2.2 The magnetic spectrometer FRS	62
3.2.3 Measurement	63

4	Results and discussion	69
4.1	<i>Charge-state distributions</i>	69
4.2	<i>Stopping powers</i>	73
4.3	<i>Energy and range focusing</i>	78
5	FRS-Ion Catcher - a new instrumentation for research with exotic nuclear beams	80
5.1	<i>Setup of the FRS-IC</i>	80
5.2	<i>The gas cell</i>	81
5.3	<i>The vacuum system</i>	87
5.4	<i>The planned setup</i>	89
6	Summary	93
7	Zusammenfassung	95
8	Appendix	97
	<i>A: Target ladders</i>	97
	<i>B: Data tables</i>	99
	Charge-state distributions	99
	Stopping power	106
	Range focusing	107
	References	108
	List of figures	112
	Acknowledgements	118

1 Introduction

The goal of this work is to investigate the slowing down process of relativistic ions and to determine the best method to efficiently provide high precision experiments with exotic nuclei produced in fragmentation reactions.

As the radioactive nuclides cannot be found in nature, they must first be produced in a nuclear reaction. Radioactive nuclei can be produced using different projectiles (protons, neutrons, heavy ions) and a wide variety of nuclear reactions including fission, spallation, fragmentation, fusion evaporation, deep inelastic collisions and nuclear transfer reactions. After production, the nuclides of interest are separated from the other reaction products before they can be studied. The production and separation will be described for some cases of interest in chapter 2.1 and 2.2 respectively.

Radioactive ion beams offer unique opportunities to explore the properties far from the valley of stability. Studies of nuclear structure and reaction mechanisms have especially benefited from the availability of radioactive nuclear beams as wholly new possibilities to investigate the influence of extreme neutron-proton ratios or isospin dependence. Nuclei far from beta stability play a decisive role in astrophysical processes that build up heavier elements from lighter nuclei, e.g. the rp-process and r-process nuclei. And thus knowledge about such "exotic" nuclei can help us understand our own origin.

On a more applied level, radioactive nuclear beams are also used in many diverse fields as atomic physics, material research, solid state physics, nuclear chemistry and medicine. RIB-based research is in a strong phase of expansion, and a number of new accelerator and reactor-based facilities are being constructed in France, Germany, Japan, the United States and other places around the world.

The chart of the nuclides (see fig. 1-1) shows all nuclides that have been observed experimentally as a function of their proton number Z and neutron number N . The black squares indicate the stable isotopes. The colored squares represent radioactive nuclei sorted according to their dominant mode of decay: red = β^+ / EC, light blue = β^- , yellow = α , green = spontaneous fission, deep blue = neutron emitters and orange = proton emitters. Detailed data are currently only available for those nuclides that lie on or close to beta stability, and for many of the observed nuclei not even basic properties such as mass, shape, half-life and the lowest excited states are known. The white area enclosed by the dotted lines (black = neutron-, blue = proton- and green = fission-drip line) indicate nuclei that are predicted theoretically to exist. Although many of these nuclei will probably never be synthesized in a laboratory, with the advent of radioactive ion beams, our knowledge of nuclear structure and properties will be significantly increased as experiments strive to cover the unknown territory out to the extreme limits of nuclear stability.

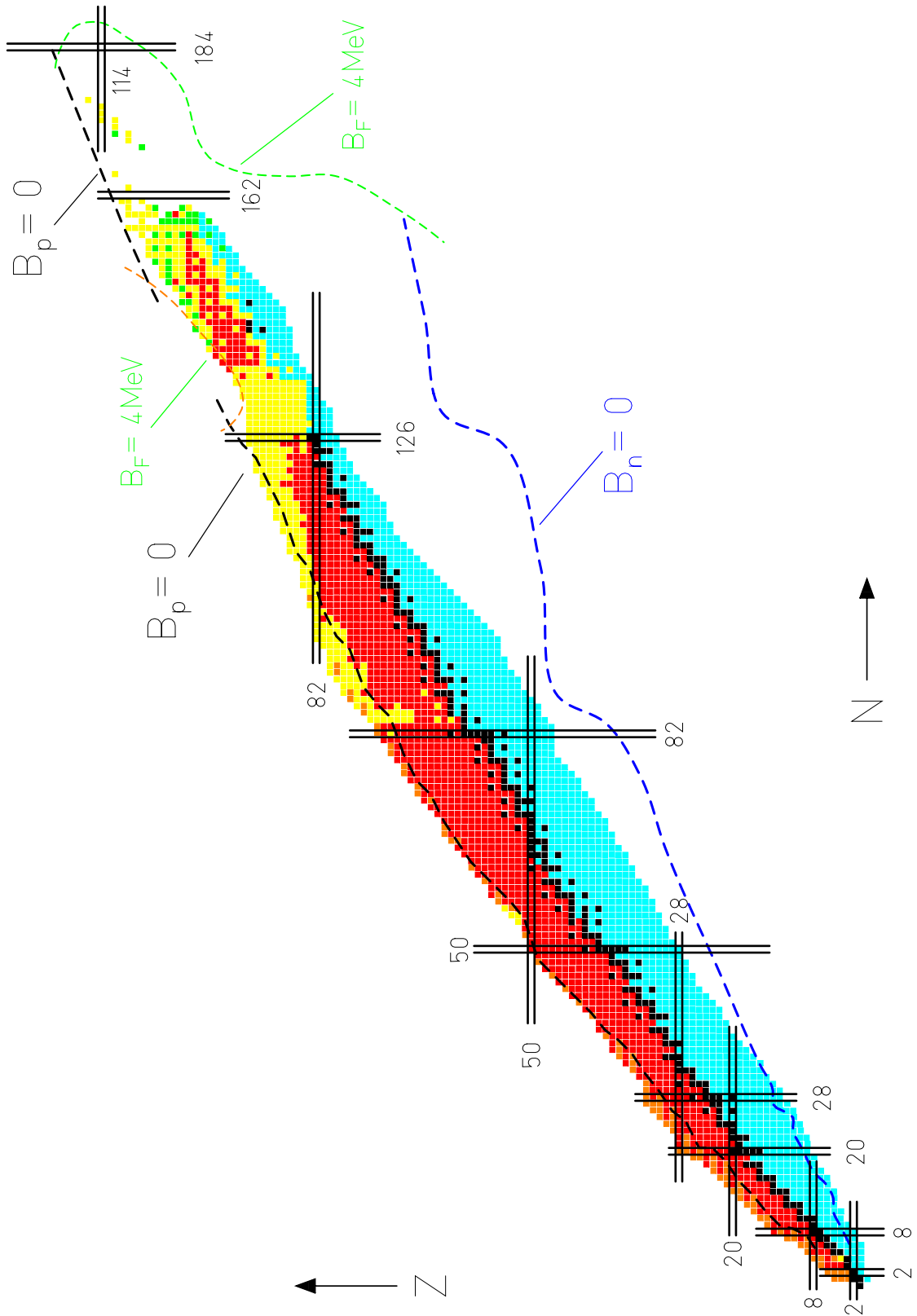


fig. 1-1 Chart of nuclides showing the proton number versus the number of neutrons. The colored squares represent radioactive nuclei sorted according to their dominant mode of decay: red = β^+ / EC, light blue = β^- , yellow = α , green = spontaneous fission and orange = proton emitters. The dotted lines indicate the proton and neutron drip lines, yet unexplored but the existence of these nuclei is expected from model calculations.

Many experiments that perform high-precision measurements on exotic nuclei require the nuclei to be slowed down and cooled or even stopped in thin layers of matter. Thus it is an essential requirement to fully understand the physical processes during the slowing down.

Today there is a lot of data (for example, collections on stopping-power measurements [PAU03]) and simulation programs available concerning the energy loss of ions in matter, yet there is a gap in the available data ranging from about 30 to 100 MeV/u and above depending on the ion-target combination. In order to improve the simulation programs for slowing down the charge-state distributions, energy loss, stopping powers and energy-loss straggling of nickel and xenon ions on various target materials in this missing energy regime are presented and compared to the predictions of different codes.

Future facilities like RIA [RIA00] and the planned international facility at GSI [CDR01] will include a low-energy branch for slowed down exotic nuclei. (See fig. 1-2.) An important part of the low-energy branch is an energy buncher shown in fig. 1-3, which basically consists of a dispersive magnetic dipole stage combined with a monoenergetic degrader [GEI89]. The latter is a specially shaped energy degrader of variable thickness along the dispersive plane, which has extremely small shape and surface tolerances. With this combination, the separated fragment beams can be slowed down and their large momentum spread can be reduced drastically. This provides narrow range distributions and the possibility to implant the isotopes into thin materials, which is advantageous for spectroscopy experiments. The results obtained using this range focusing technique for ^{56}Ni and ^{54}Co fragments at the FRS are presented in this thesis.

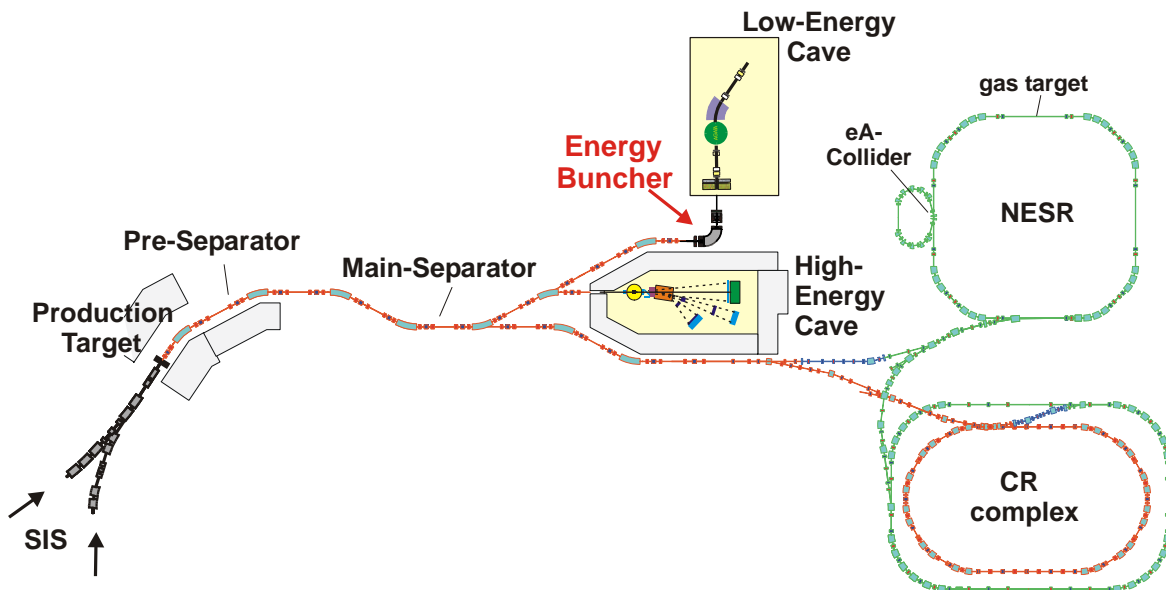


fig. 1-2 Schematic overview of the Super-conducting Fragment Separator, Super-FRS [GEI03], behind the projected heavy-ion synchrotron SIS 100/300 as proposed for the future international facility at GSI [CDR01]. It consists of a Pre-separator and a Main-separator delivering beams to three different experimental areas: the Ring Branch, the High-Energy branch, and the Low-Energy branch.

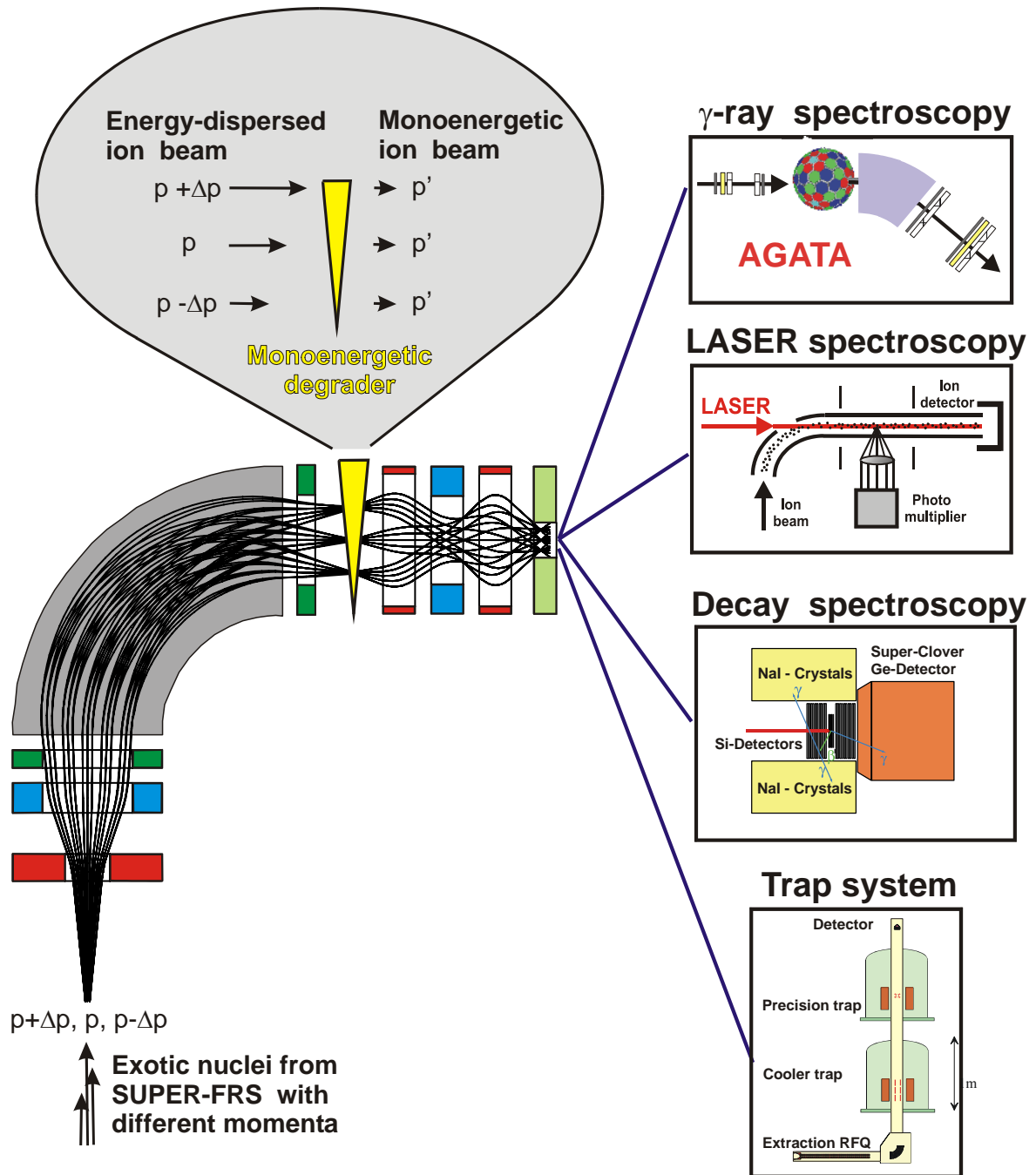


fig. 1-3 Schematic view of the energy buncher stage for the Low-Energy Branch of the planned Super-FRS at GSI. It consists of a magnetic dipole stage to spatially separate the exotic nuclei according to their momentum. The momentum spread is compensated by a specially shaped monoenergetic degrader by variation of its thickness and respective energy loss. It will serve many high precision experiments like γ -ray-, laser- and decay spectroscopy and Penning trap mass spectrometry.

The design of a gas cell station planned at GSI behind the FRS, called the FRS-Ion Catcher [FRS03], is described in the last chapter where for the first time relativistic heavy ions will be stopped in a gas cell [SAV03], cooled and extracted to different experimental setups. This is part of the Ion-Catcher network [ICA03] for developing techniques to effectively slow down, stop, and extract radioactive ions.

2 Theory

Chapter 2.1 will briefly cover production mechanisms of exotic nuclei, as these are the processes determining the initial kinematical properties which are to be investigated. In chapter 2.2 the three main approaches to separation of nuclear beams are described. These are namely the in-flight separation, the isotope separation on-line (ISOL) and a new technique called ion-catcher, combining the advantages of the two as developed for the next generation of nuclear accelerator facilities. In chapter 2.3 the basics of the theoretical description of the physical processes involved during the slowing down of ions in matter are treated. The outcomes of these processes are the energy loss, the energy-loss straggling and the charge-state distribution of the ions. Finally, the important quantities in order to fully stop an ion beam, the total range and the range straggling of decelerated ion beams, are discussed.

2.1 Production mechanisms for exotic nuclear beams

Radioactive nuclear beams can be produced with a wide variety of techniques. A common factor is that the isotope of interest is produced in a nuclear reaction, between an accelerated primary projectile beam and a stationary target. The list of reactions that are used for RIB experiments is long: fission, fusion-evaporation, spallation, and fragmentation to name a few. All these reactions are two-step processes. In the first step an intermediate nucleus is formed. Due to the excitation energy from the production process, this nucleus is highly excited. In the second step this nucleus then equilibrates. This de-excitation process is independent of the formation and the competing channels for the de-excitation are neutron, proton or α evaporation, prompt fission and γ emission.

The choice of the reaction depends to a large degree on which radioactive nucleus one wants to produce. This is indicated in fig. 2-1 where the preferable production mechanism is shown superimposed on a chart of the nuclides. As the average binding energy for neutrons is lower than for protons, the neutrons are preferentially evaporated, leaving residues with lower isospin than the projectile/target combination. Hence, it is difficult to produce neutron-rich residues from nuclear reactions, although fission and some fragmentation reactions can be used. Overall, the probability to produce a certain nuclide, based on the production cross section, decreases rapidly with the distance from the β -stability line no matter what method is employed.

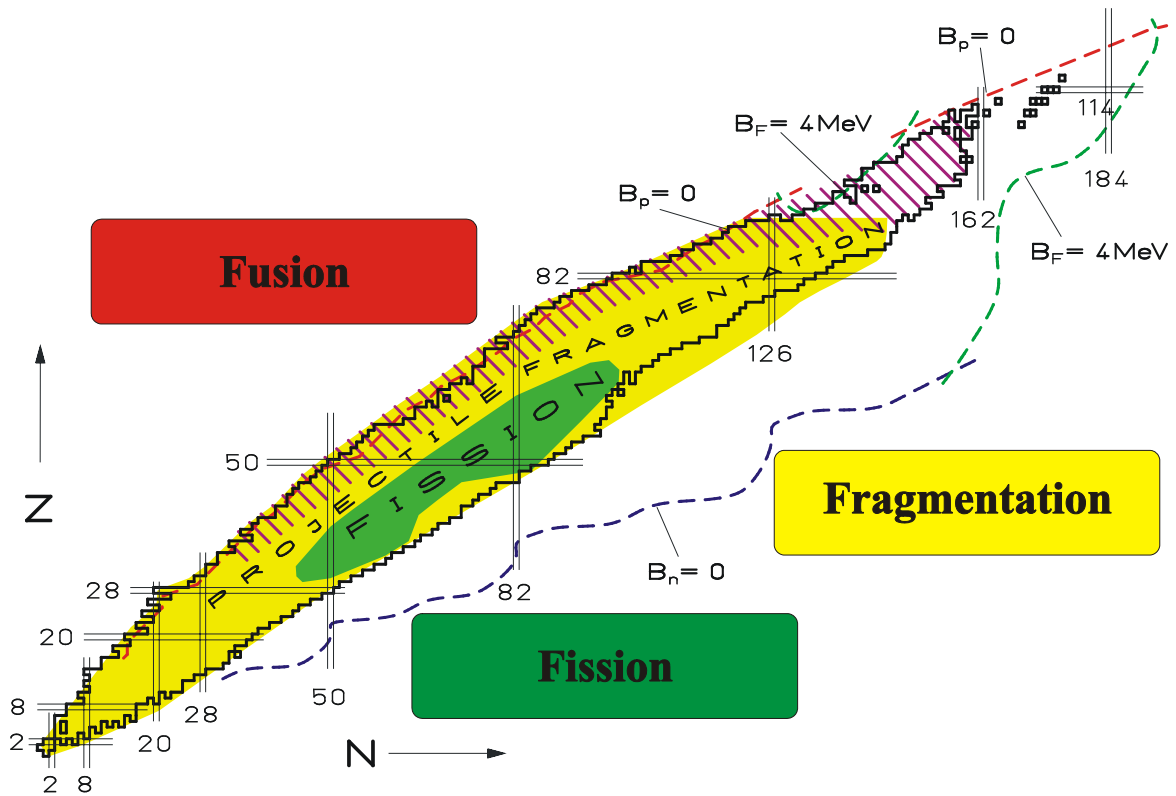


fig. 2-1 The chart of nuclei, showing schematically the different production mechanisms for exotic nuclear beams: fusion (red), fission (green), and fragmentation (yellow).

2.1.1 Fragmentation

To obtain radioactive ion beams at accelerator facilities one can use fragmentation of stable heavy nuclei impinging on a target material. If a projectile nucleus hits a target nucleus with an impact parameter smaller or equal to the sum of their radii, a nuclear reaction takes place and both target and projectile fragments are produced. The reaction products are characterized accordingly as target or projectile fragments. Light fragments are produced with high multiplicity in central collisions. The fragments close to the projectile mass are produced in reactions with large impact parameters.

The heavy fragments which are of interest here are mainly produced in peripheral collisions at relativistic energies [GRE85]. The created projectile fragments are emitted with projectile velocities and angles around zero degrees with respect to the laboratory frame. These kinematical properties allow magnetic separators to be efficiently used for isotopic separation of the reaction products as will be discussed in more detail in chapter 2.2.2.

The total cross section of fragmentation reactions can be described by the geometrical Kox parameterization [KOX87]

$$\sigma_R = \pi R_{\text{int}}^2 \left(1 - \frac{B_C}{E_{c.m.}} \right),$$

eq. 2-1

where $E_{c.m.}$ is the center of mass energy and B_C is the Coulomb barrier of the projectile/target nuclei combination given by

$$B_C = \frac{Z_2 Z_1 e^2}{r_C (A_2^{1/3} + A_1^{1/3})}.$$

eq. 2-2

with $r_C = 1.3 \text{ fm}$, $Z_{(T,P)}$ as the atomic numbers of the target and projectile nuclei, $A_{(T,P)}$ as their mass numbers and R_{int} as the interaction radius. This interaction radius is where the actual parameterization comes in. It can be divided into a volume and a surface component

$$R_{int} = R_{Vol} + R_{Surf}.$$

eq. 2-3

Collisions at small impact parameters give rise to nuclear reactions independent of mass and energy and can be parameterized using the volume component of the interaction radius

$$R_{Vol} = r_0 (A_2^{1/3} + A_1^{1/3})$$

eq. 2-4

with $r_0 = 1.1 \text{ fm}$. The nuclear surface contribution is described as

$$R_{Surf} = r_0 \left(a \cdot \frac{A_2^{1/3} \cdot A_1^{1/3}}{A_2^{1/3} + A_1^{1/3}} - c \right),$$

eq. 2-5

with a as the mass asymmetry term related to the volume overlap of projectile and target, and c as an energy dependent parameter taking care of the increasing surface transparency as the projectile energy increases. Both parameters are dimensionless. The value for $a = 1.85$ and c varies between 0.65 and 2.05 .

For very heavy systems another additional correction is added to the surface term (R_{surf}) to include the neutron skin excess

$$R_{surf}(\text{heavy}) = R_{surf} + D,$$

eq. 2-6

with

$$D = \frac{5(A_2 - 2Z_2)Z_1}{A_2 A_1}.$$

eq. 2-7

To obtain cross sections for single isotopes produced in fragmentation reactions, the abrasion-ablation model is commonly used. It is based on the simple idea that when two relativistic heavy ions pass so close to each other that part of their volumes overlap, the overlapping regions are sheared off (abrasion). The remaining chunk of projectile matter continues its path essentially undisturbed and thus with the same velocity, yet the remaining projectile part after abrasion is in an excited state and loses its energy by emitting particles (ablation). These two processes then determine the proton and neutron number of the isotope produced in the fragmentation reaction [GAS91],[IKG95]. To calculate the yield of a certain fragment in the reaction one can also use empirical parameterization formulas like the code EPAX [SÜM90].

The momentum width of projectile-like fragments emitted in fragmentation reactions can be described using the Goldhaber model [GOL74]. In this model the momentum width is determined by the intrinsic Fermi motion of the constituent nucleons which are removed from the projectile during the breakup. If $(A_0 - A_f)$ nucleons are suddenly removed from a nucleus with originally A_0 nucleons a nucleus of A_f nucleons will emerge. The momentum width of the fragment A_f in the projectile system is

$$\sigma_{A_f} = \sigma_0 \sqrt{\frac{A_f \cdot (A_0 - A_f)}{A_0 - 1}},$$

eq. 2-8

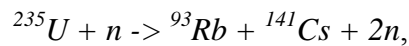
where σ_0 , the reduced momentum width, is related to the intrinsic Fermi motion of a single nucleon. If the projectile nucleons have a mean square momentum in the projectile frame equal to $3/5 \cdot P_F^2$, with P_F being the Fermi momentum, then a momentum dispersion of $\sigma_0^2 = 1/5 \cdot P_F^2$ is expected. The reduced momentum width σ_0 thus amounts to $\sim 90 \text{ MeV}/c$.

2.1.2 Fission

Nuclear fission is the final barrier for the mass of a nucleus and was first discovered in 1939 by Hahn, Straßmann [HAS39] and Meitner [Mei39]. Shortly after that Bohr and Wheeler [BoW39] realized that heavy nuclear systems become unstable against shape oscillations due to the Coulomb repulsion of the protons. In the framework of the liquid drop model they did a thorough investigation of the energetic properties.

The fission barrier depends on the two deformation terms: the surface and the volume term. Shell effects are not included in this model yet they have a decisive impact on the fission properties [KRA88] such as the change of the asymmetric mass distribution for lighter nuclei, the fission probability and the existence of fission isomers to name a few. Still the liquid drop model is not only helpful analytically to describe the kinematics but it also provides an eidetic image of the physical process.

One distinguishes between spontaneous fission sources (e.g. ^{252}Cf) and induced fission. The typical mass distribution of fission fragments is shown in fig. 2-2 for a ^{252}Cf source. A typical neutron induced fission reaction is



which is possible for incident neutrons at thermal energies. As there are more neutrons released than needed to trigger the fission process these types of nuclear reactions can be used for controlled chain reactions like in nuclear reactors.

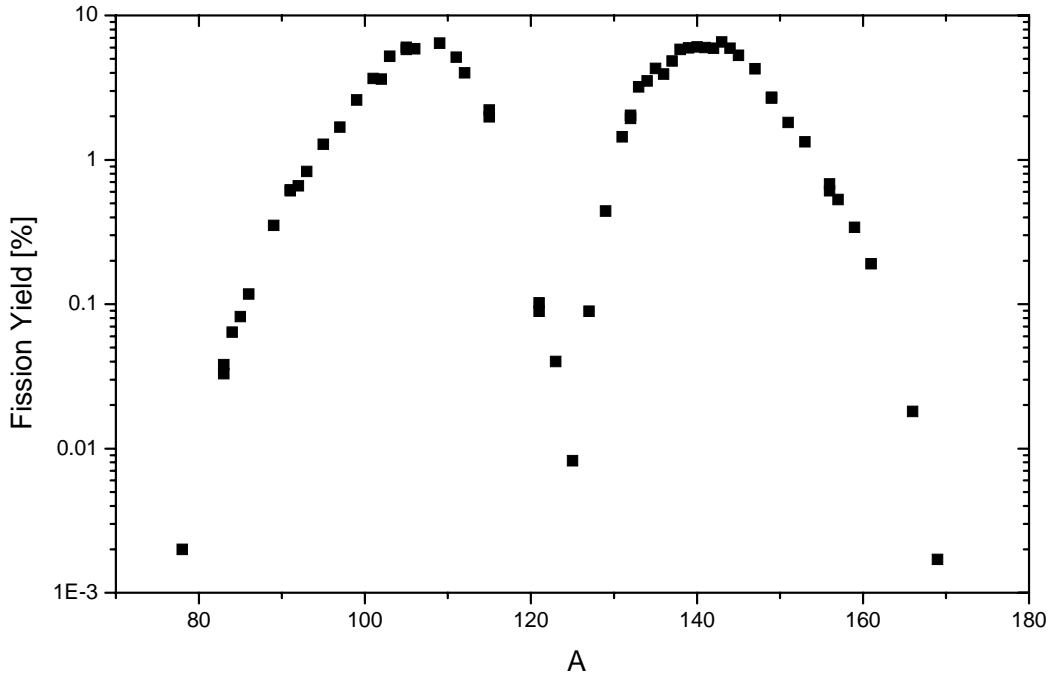


fig. 2-2 The fission yield for ^{252}Cf versus the mass number. The two humps correspond to fragments around ^{108}Tc with 103 MeV and ^{143}Xe with 78 MeV. A source of this type has been used at Argonne to investigate the properties of the prototype gas cell [SAV03] described later.

The kinematics of the fission fragments is isotropic as they are simply driven apart by Coulomb repulsion at the point of separation. The kinetic energy of these residues can be for example calculated using the Brosa [BRO89] or Viola [VIO85] parameterization.

$$E_K(\text{Brosa}) = 0.14 \frac{Z_1 Z_2}{A^{1/3}} - 30 \text{MeV}$$

$$E_K(\text{Viola}) = 0.1189 \frac{Z_1 Z_2}{A^{1/3}} - 7.3 \text{MeV}$$

eq. 2-9

where Z_1 and Z_2 are the nuclear-charge of the two fission products and A is the mass number of the mother nuclei. Thus the most probable energy in the laboratory frame can be predicted as a simple function of the Coulomb parameter ($Z^2/A^{1/3}$).

At relativistic energies, nuclear disintegration after Coulomb excitation becomes important. The Lorentz-contracted Coulomb field of relativistic heavy ions with large proton numbers mainly excites the giant dipole resonance of the projectile; for an energetic heavy nucleus the probability of Coulomb excitation in the field of a heavy target exceeds the geometrical cross section [BER88].

The isotopic distributions created by induced fission are determined by the excitation energy. For example, fission of ^{238}U , induced by thermal neutrons from nuclear reactors, creates the well-known double-humped fragment distribution forced by the strong shell

effects [WAG91]. For increasing excitation energy, the influence of the shells disappears and the valley in the double-humped distribution is filled [ARM95].

2.1.3 Fusion

Fusion is the energy source of the stars as our sun. The first process in stellar environments that ignites is the hydrogen burning where four protons form a ${}^4\text{He}$ nucleus. For most applications of fusion, from controlled fusion reactors to solar processes the reacting particles have kinetic energies in the range of 1-10 keV. These are small compared to the Q-values which are in the range of several MeV. In nature these processes only occur in drastic environments because of the substantial limitations imposed by the Coulomb barrier. Once this barrier is overcome fusion becomes very likely as the two overlapping nuclei quickly reach a state of minimum energy.

The Coulomb barrier for two reacting particles X and Y with the radii r_X and r_Y just touching their surfaces is given by

$$V_C = \frac{e^2}{4\pi\epsilon_0} \cdot \frac{Z_X \cdot Z_Y}{R_X + R_Y}.$$

eq. 2-10

The effect of the Coulomb barrier on the fusion reaction is very similar to the same effect in α -decay, so the product $Z_X Z_Y$ will ultimately appear in an exponential barrier penetration probability. Therefore the essence of controlling fusion reactions and to extract usable energy is very challenging. It requires heating the thermonuclear fuel to temperatures of 10^8 K while simultaneously keeping the plasma density high enough.

In accelerator experiments the situation is somewhat different as it is possible to accelerate the projectile to energies at the Coulomb barrier. At these energies central collisions of heavy ions with the target atoms lead to complete fusion. This production mechanism is best suited to obtain neutron deficient nuclei and for the production of the super-heavy elements. The heavy ion fusion products recoil from the target with center of mass velocity. The velocity spread of the recoils is hereby determined by the momentum transfer of the evaporated nucleons and by atomic straggling effects in the target.

2.2 Separation methods

Since in most cases the production reaction is non-selective the reaction products must be subsequently separated if any degree of isotope purity is desired. The force (\vec{F}) used to deflect the ions in electro-magnetic separators is the Lorentz force given by

$$\vec{F} = \frac{d\vec{p}}{dt} = q(\vec{E} + \vec{v} \times \vec{B})$$

eq. 2-11

where \vec{p} is the momentum and q the charge of the particle. \vec{E} and \vec{B} are the electric and magnetic field respectively and \vec{v} is the velocity of the projectile. One defines a quantity called magnetic rigidity $B\rho$ and electric rigidity $E\rho$ with the bending radius ρ .

$$B\rho = \frac{p}{q} = \frac{\gamma m_0 v}{q}$$

eq. 2-12

$$E\rho = \frac{pv}{q} = \frac{\gamma m_0 v^2}{q}$$

eq. 2-13

These formulas are valid for a homogeneous magnetic field perpendicular to the ions' path and a radial electric field respectively.

An electro-magnetic separator consists of different components. The most commonly used ones are magnetic or electric dipole-, quadrupole- and multipole-fields of higher order as well as magnetic solenoids. Combinations of electric and magnetic fields are used as velocity filters, i.e. the Wien filter shown in fig. 2-3. Sending a beam through electric and magnetic field lines crossed perpendicular one can filter different velocities. The counteracting Lorentzian and electric force from the crossed fields yields a velocity dependence in the sense that for each velocity a combination of forces can be found with a resulting force zero. The selected velocity can be calculated as

$$F_{el} = F_B$$

$$qE = qvB$$

$$\Rightarrow v = \frac{E}{B}$$

eq. 2-14

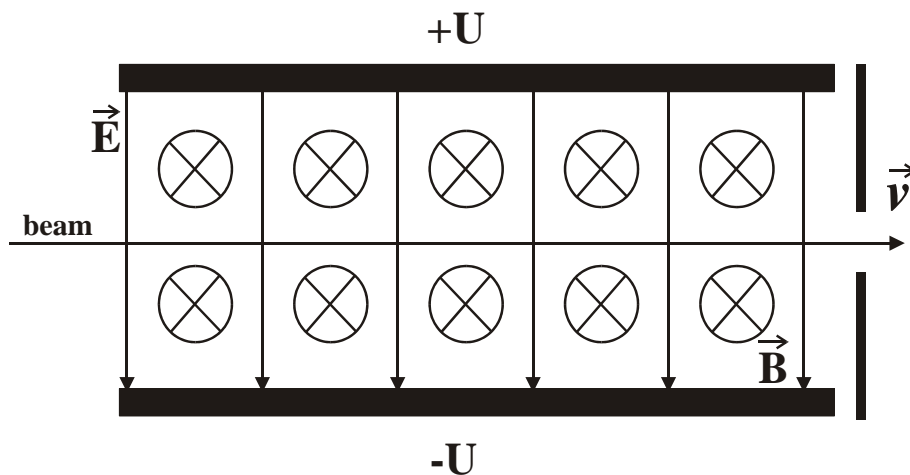


fig. 2-3 Schematic illustration of the working principle of a Wien filter. The ions enter the perpendicular magnetic and electric field and only the ions with a certain velocity pass through.

Yet due to the technical limitations in the electric field strength this is only applicable for lower beam energies and therefore used for fusion-evaporation produced secondary beams

like for the famous production of super-heavies at SHIP [HOF00] and not for fragmentation reactions.

The most basic magnetic separator is a simple magnetic dipole. But as seen from eq. 2-12 it allows only for a m/q separation. This means that projectiles with the same mass but different charge are not projected to the same position. In order to collect all charge states of a certain mass it is common to use gas-filled separators [ENG67] as shown in fig. 2-4. The concept herein is that the projectiles constantly change their charge due to collisions with the buffer gas. Therefore they have a mean charge \bar{q} and are all projected to the same location on the focal plane as can be seen from the equations. From equation eq. 2-12 and the mean charge

$$\bar{q} = Z_1^{1/3} \frac{v}{v_0}$$

eq. 2-15

follows that

$$B\rho = \frac{mv_0}{Z_1^{1/3}}$$

eq. 2-16

and thus is independent of the velocity of the ions. Therefore they can be separated by slits at the focal plane from other contaminants.

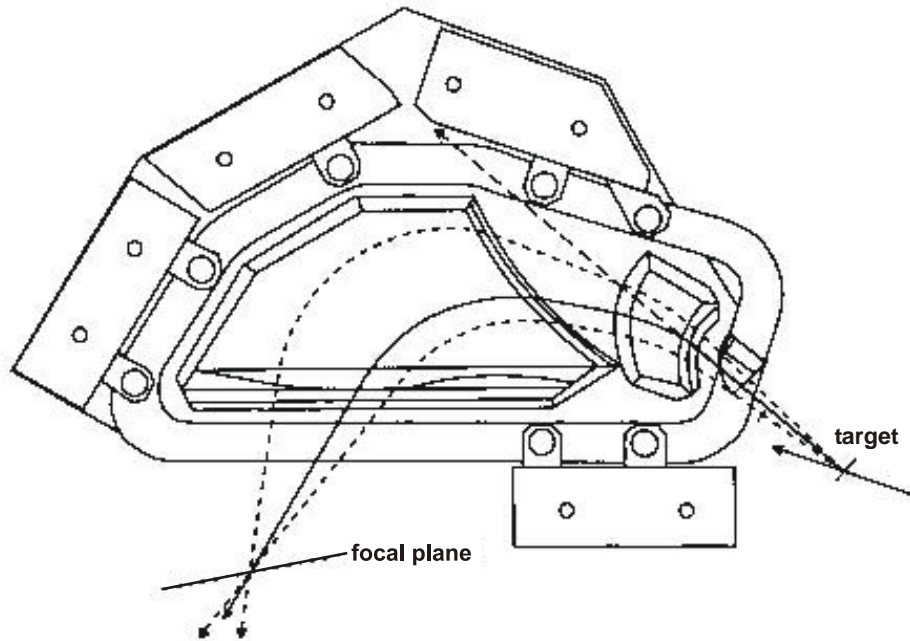


fig. 2-4 Gas filled magnetic separator ENGE [ENG67]. Due to the collisions of the projectiles with the buffer gas, ions of a mean charge are focused to the same position on the focal plane.

2.2.1 ISOL method

The isotope separation on-line (ISOL) technique illustrated in fig. 2-5, has been used very successfully over the past decades to produce exotic nuclei [BEY03]. In the ISOL method the radioactive particles are created by a light high-energy ion beam (e.g. protons) impinging on a thick target. The created radioactive atoms have to be released from this

target, for example by heating it. The residues are collected (e.g., in a catcher foil or in a gas), transported via diffusion or gas-jet techniques into an ion source where they are ionized, and then extracted by a relatively low, typically a few 10 keV, acceleration potential. The resulting ion beam can then be electro-magnetically mass separated.

However, in order to leave the target by diffusion the particles have to be chemically inert, as the release time ranging from around 10 ms up to many seconds depends on the chemical properties of the ion and target material. A detailed review of the properties using an ISOL type facility can be found in [BEY03]. This again limits the possible candidates to considerably long-lived isotopes and does not allow the exploration of the borders of the nuclear chart.

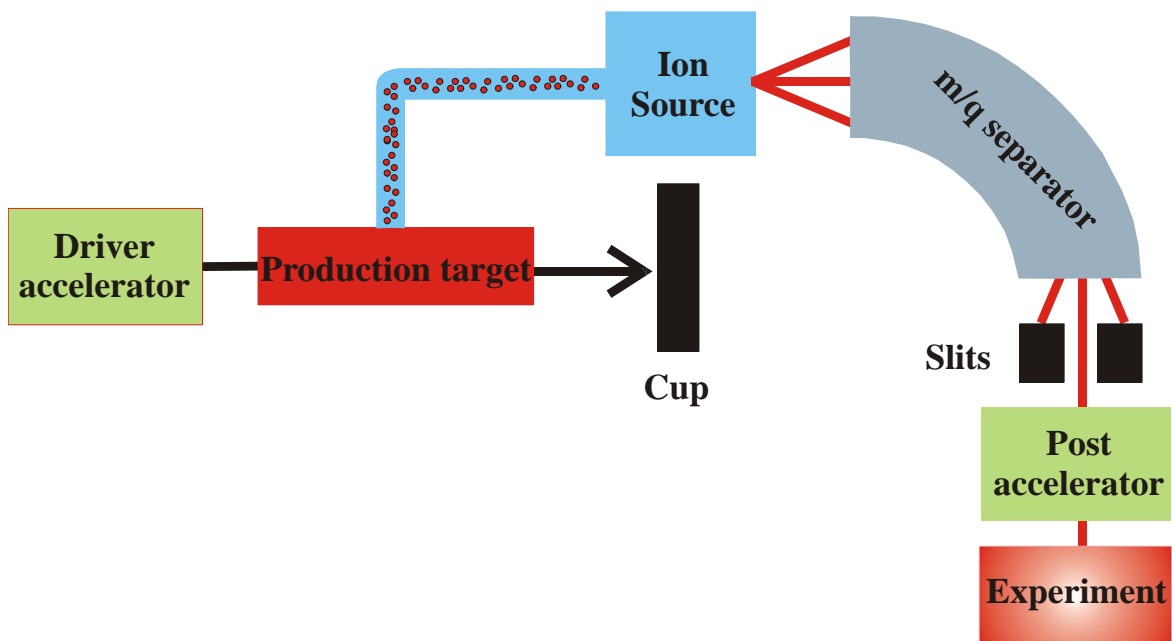


fig. 2-5 Illustration of the Isotope Separation On-Line (ISOL) technique [RAV79]. The light projectiles (protons) impinge on a thick target producing the radioactive nuclei which are stopped in the target. By heating the target they are released, transported to an ion source where they are re-ionized for post acceleration.

Ion beams produced by ISOL techniques have low energies, typically 10-100 keV and are easy to implant. However, event-by-event particle identification is normally not possible due to the low energies, which can be a drawback especially when the separated beam is not isotopically pure. Often the ISOL beams contain several nuclides with the same mass, unless special element-selective ion sources like laser ionization [LET98] are used.

2.2.2 In-flight method

Opposing the ISOL technique in-flight separation, see fig. 2-6, uses heavy ions as projectiles and thin targets to produce the secondary beam. The projectile fragments are not stopped but leave the target with almost the same velocity as the primary beam that entered. After the target they can be separated in an electro-magnetic separator directly following the production target as due to the high energies a post acceleration is not needed.

As the projectile fragments have an angular and energy distribution due to the nuclear reaction and the energy loss in the target, the separator should have a large acceptance and

must focus the beam back onto a small area to keep a high yield. To achieve overall achromatism fragment separators use a back-to-back geometry as indicated in fig. 2-6. The dispersion of the first stage does the selection. The position of the fragments at the intermediate focus depends on the magnetic rigidity. The second stage compensates the dispersion of the first.

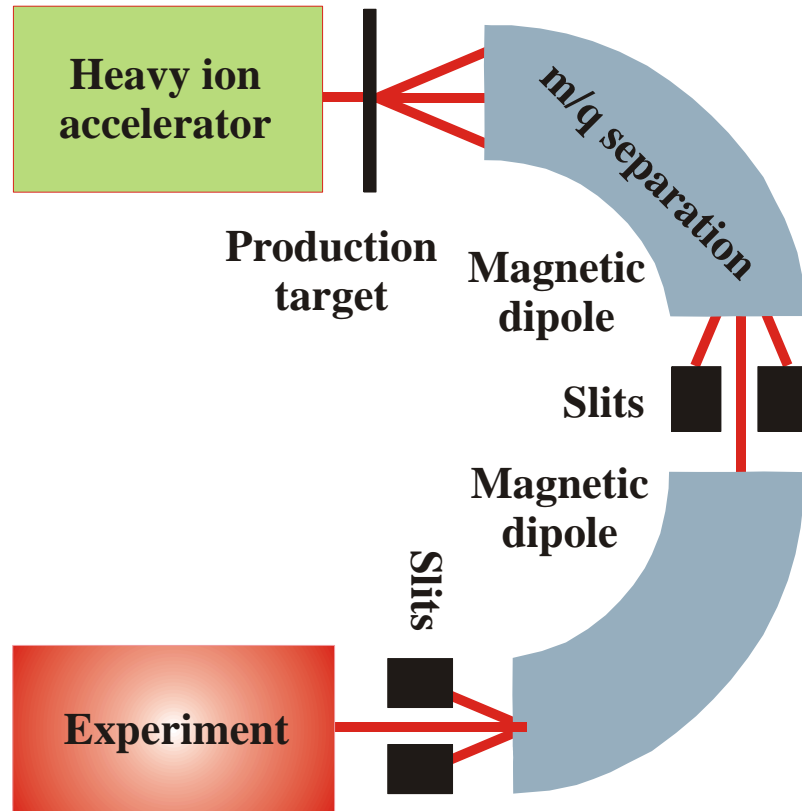


fig. 2-6 Illustration of the In-flight separation technique. The heavy ion beam from an accelerator impinges on a thin target where the nuclei of interest are produced in projectile fragmentation reactions. They leave the target with almost the same velocity as the primary beam and thus need not to be reaccelerated for separation. The two-stage separation allows the system to be kept achromatic while separating in mass and charge.

To finally achieve separation of single nuclei a degrader has to be used, as the magnetic separator alone cannot separate ions of the same m/q . A degrader is nothing but a piece of matter the projectiles have to pass. As we will see in chapter 2.3.1 the energy loss is roughly proportional to q^2 . Thus different elements with different q will have different velocities after passing the degrader and will therefore be separated according to their magnetic rigidity in the second dispersive stage. To preserve the achromatism of the device, the degrader has to be wedge shaped [GEI89]. It has to be thicker on the high velocity side and thinner on the low velocity side. Degraders of this type are called achromatic or monoenergetic degrader.

The working principle of the fragment separator FRS [GEI92], shown in fig. 2-7, illustrates the calculated separation of ^{78}Ni fragments. A ^{86}Kr beam with 500 MeV/u delivered by the heavy ion synchrotron SIS18 impinges on a 1 g/cm^2 beryllium target producing ^{78}Ni in a fragmentation reaction. The FRS consists of four dipoles, quadrupole triplets and duplets for x and y focusing and four sextupoles for second order optical corrections. In between each dipole stage is a focus (F_1 to F_4). In the first half of the FRS from the target to F_2 the

first selection according m/q is done. The selected area of the chart of nuclei is shown on the bottom left.

At the second focal plane the wedge shaped degrader is placed just behind slits to keep the achromaticity condition and to separate the fragments according to their energy loss in the degrader. The second half then is again a $B\rho$ separation with the new $B\rho$ depending on the charge. It compensates the dispersion from the first half. This method is called the $B\rho - \Delta E - B\rho$ separation.

To conclude, in-flight separation is a very fast (sub μs range) and chemically independent method giving access to all nuclei up to uranium. It provides isotopic clean secondary beams. Yet, the beam quality is poor compared to the ISOL approach discussed before. The fragments typically have a large momentum distribution only limited by the acceptance of the device. But fragmentation reactions are used at high kinetic energies (50-1000 MeV/u), which makes it possible to still obtain a well-focused secondary beam. For the FRS the momentum acceptance is in the order of $\Delta p / p = \pm 1\%$, sufficient for most reactions.

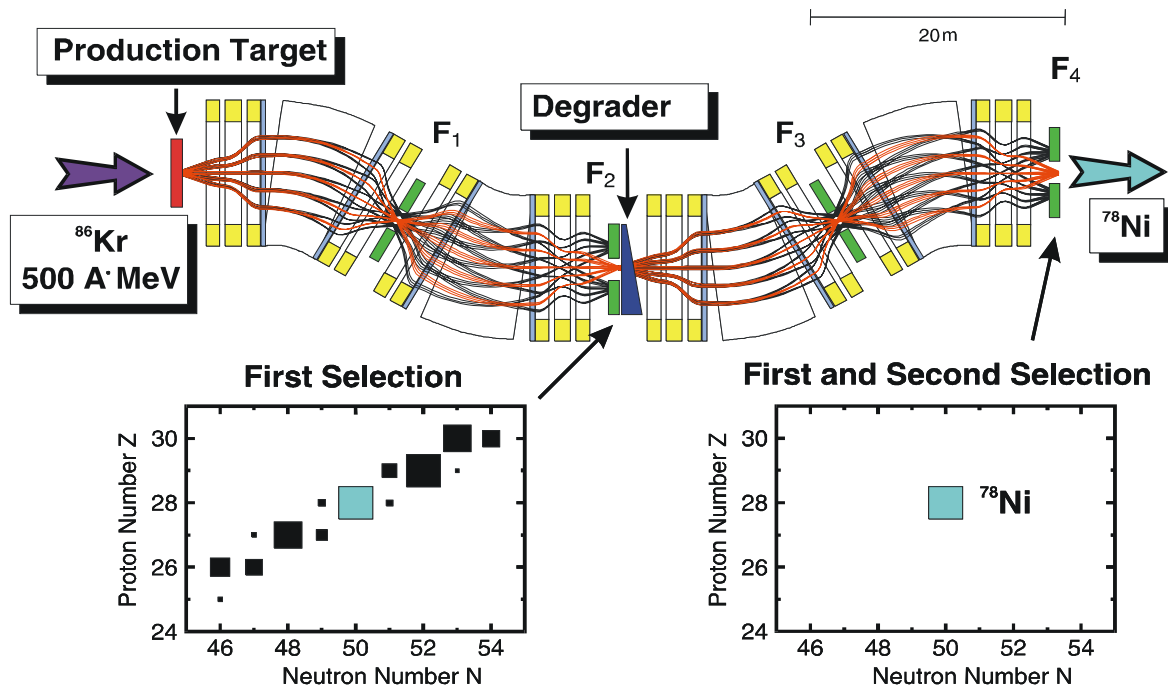


fig. 2-7 Calculated separation performance of the fragment separator FRS at GSI for the production of ^{78}Ni . A ^{86}Kr beam from the SIS with $500 \text{ MeV}/u$ impinges on the $1 \text{ g}/\text{cm}^2$ Be production target to produce ^{78}Ni in a fragmentation reaction. The first stage selects nuclei with the same m/q from the chart of nuclei and the second cut reduces the selection to ^{78}Ni only.

Such beams are well suited for experiments where event-by-event particle identification is required (e.g. searches for new nuclides) and for reaction mechanism studies where the separated radioactive beam interacts with a secondary target. It is, however, difficult to perform investigations requiring that the secondary beam is slowed down and implanted, e.g. decay studies - because of the high energy, thick degraders must be used, which lead to losses due to angular and range straggling as well as nuclear reactions.

2.2.3 The new hybrid separation method

A new approach to the production of low energy radioactive beams are ion catchers. The principle, shown in fig. 2-8, is to slow down and thermalize a fast beam coming from fragmentation, in-flight fission or fusion-evaporation reactions in a degrader and gas cell setup. The degrader has two main objectives. The first is to slow down the beam to energies suitable for stopping in a gas cell and secondly to reduce the energy spread. In the gas cell the recoils lose their residual energy in high purity helium, recapturing electrons until they come to rest. A large fraction of the ions will be in a singly ionized charge state due to the high ionization potential of atomic helium (He^{1+} 24.6 eV). From the gas cell the mainly singly charged ions can be extracted by means of applied electric DC, RF fields and the gas flow through a nozzle into a low pressure region. After extraction the ions kept in the potential of an ion guide and are separated from the helium gas by means of differential pumping. Then they are further directed to high precision experiments or post acceleration.

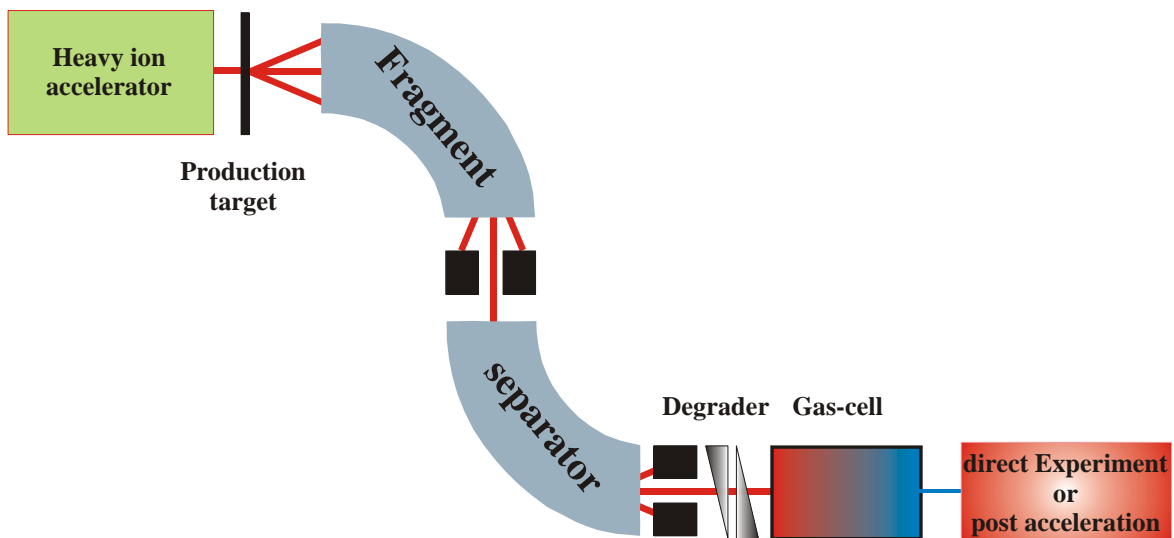


fig. 2-8 Illustration of the ion catcher technique. Behind a fragment separator a degrader system is used to slow down the projectiles far enough to finally stop them in a noble gas. Due to the high ionization potential of the noble gas a large fraction of the projectiles can leave the cell through a nozzle in a single ionized state. From there they can be further directed to experimental setups or post-accelerated.

This hybrid of the ISOL and In-flight technique removes the limitations due to chemical and lifetime properties as present in the ISOL case. Yet it delivers a low energy beam with small emittance suited for high precision experiments.

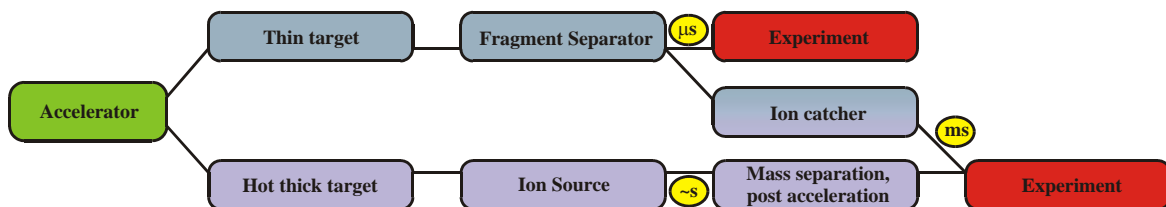


fig. 2-9 Schematic illustration of Ion catchers being a link between ISOL and in-flight technique. The main objective herein is to provide low energy, high quality exotic beams, chemistry independent and in a time of a few ms.

Such an approach is proposed as part of many next generation facilities like for the low energy branch of the SUPER-FRS at GSI [CDR01] in Germany, the Rare Isotope Accelerator (RIA) project in the USA [RIA00] and for the Riken radioactive beam facility [RIK00] in Japan.

A degrader system as indicated in fig. 2-8 for these type of setups has been developed and tested in an experiment at the FRS as part of this work and is in detail described in chapter 3.2. Chapter 5 is devoted to the development and collaboration work for a full-scale gas cell test behind the FRS, the FRS-Ion-Catcher [FRS03].

2.3 Slowing down of heavy ions in matter

The understanding of the slowing down and stopping of ions in matter is of basic scientific interest and has many applications. Detectors e.g. ionization chambers are based on the knowledge of energy loss of the particles. The doping of semiconductors and hardening of metals as well as cancer therapy [KRA88] has benefited greatly from the understanding and predictability of the stopping process.

The theory of energy loss has been developed over decades as there are many phenomena that have to be included in a complete description. Thus the first part of this chapter is devoted to the description of the charge-state distribution (CSD) of the projectile as it travels through the target material. The next part will present the energy loss and the contributions to it for the different energy regimes and the range of the projectile until they are fully stopped. To stop relativistic projectiles in thin layers of matter it is very important to understand the longitudinal and angular straggling processes and properties.

2.3.1 Charge-state distributions

Ions traveling through matter can change their charge state. As we will see in chapter 2.3.1.3 it is essential to know the charge of the projectile precisely for energy loss calculations as this depends strongly on the charge of the projectile. In case the projectiles have a charge distribution one has to sum over the partial stopping powers of ions in each charge state. As the exact charge distribution is mostly unknown and hard to calculate most calculations use the concept of a mean charge or an effective charge. The mean charge is simply the weighted mean of the charge-state abundances. The effective charge is defined by Northcliffe [NOR60] as the charge to scale the proton stopping power to the stopping power for heavy ions.

$$q_{eff}^2 = \frac{dE/dx(hi)}{dE/dx(p)} \Big|_v$$

eq. 2-17

To describe the charge-state distribution the Bohr criterion is used which states, that ions are ionized only if the velocity of the projectile is higher than the orbital velocities of the removed electrons. This full ionization will happen for $v \geq v_0 Z_1$ where v_0 is the Bohr velocity of the K-shell electrons of Hydrogen. Due to empirical considerations one expects an exponential increase of the number of electrons with decreasing projectile velocity that leads to formulas of the form [NOR60]

$$\left(\frac{q_{eff}}{Z_1} \right)^2 = 1 - 2c_1 \exp\left(- \frac{c_2 v}{v_0 Z_1^{2/3}} \right).$$

eq. 2-18

The two factors c_1 and c_2 allow to adjust the effective charge. According to a formula by Pierce and Blann [PIB68] the mean charge can be calculated as

$$\bar{q} = Z_1 \cdot \left(1 - e^{-130 \frac{\beta}{Z_1^{2/3}}} \right),$$

eq. 2-19

with $\beta = v/c$ but the agreement with experimental data is not sufficient for the aim of this thesis.

Still these formulas describe quite well the velocity dependence of the stopping power [ZIE85], [HUB90]. The non-uniform change of the effective charge q_{eff} due to the shell structure of the projectile is only taken into account by $dE/dx(p)$ in equation eq. 2-17 but not for heavy ions. Predictions for unknown target and projectile combinations can be done by inter- or extrapolation of the available data. For a more precise treatment one has to know the charge-state distribution and to calculate the energy loss via the partial stopping powers.

A more realistic approach considering the basic physical processes is used by the GLOBAL code [SCH98] which was used in this work to compare to the measured charge-state distributions. In the following the underlying physical concepts are described. The modeling of charge-state distributions of ion beams passing through matter requires the knowledge of the basic interaction mechanisms, the processes of projectile ionization and excitation as well as electron capture. Also the lifetime of excited states has to be considered, especially for dense media where the high collision rates may lead to different charge-state distributions compared to low density materials, the so called Fermi density effect [FER40].

2.3.1.1 Ionization

Ionization is the process where a bound electron is emitted from an atom or ion into the continuum as a consequence of the energy transfer in a collision. Ionization cross sections are mostly calculated quantum mechanically in the **Plane Wave Born Approximation (PWBA)**. The assumption in PWBA is that the outgoing projectile wave is unaltered the same as the incoming wave.

The starting point of calculating inner shell ionization cross section thus is given by [ANM85]

$$\sigma_{1s} = \frac{8\pi\alpha_0^2 Z_1^2 \alpha^2}{\beta^2} \int_0^\infty d\varepsilon \int_{q_0}^\infty \frac{dq}{q^3} |F(q)|^2.$$

eq. 2-20

Z_1 is the atomic number of the projectile nucleus, $v = \beta c$ is the ion velocity, c the speed of light, α the fine structure constant, a_0 the classical Bohr radius, ε the kinetic energy of the ionized electron, $q_0 = \frac{(E_K + \varepsilon)}{v}$ the minimum momentum transfer to ionize an electron

in the K-shell, where E_K is the K-shell electron binding energy. The quantity $F(q)$ is an ionization form factor given by

$$|F(q)|^2 = \left\langle \varepsilon \left| e^{\frac{i\vec{q}\cdot\vec{r}}{\hbar}} \right| s \right\rangle.$$

eq. 2-21

One has to treat the single energy levels independently. Therefore, this form factor is the transition matrix element for the transition of the bound state $|s\rangle$ to the continuum state $\langle\varepsilon|$.

2.3.1.2 Electron capture

The two most important processes for electron capture are the radiative electron capture (REC) and the non-radiative electron capture (NRC). REC dominates at high-energy collisions of high Z projectiles with low Z targets and the electron capture is followed by a γ emission. Essentially, this is the inverse of the photo electric effect.

An estimate of REC cross sections into the projectile K-shell can be obtained using the non-relativistic dipole approximation and multiplying the result with the number Z_2 of quasi free electrons in the target [STO30].

$$\sigma_{K-REC} = Z_2 \cdot 9165 \text{barn} \cdot \left(\frac{\kappa^3}{1 + \kappa^2} \right)^2 \cdot \frac{e^{-4\kappa \cdot \arctan\left(\frac{1}{\kappa}\right)}}{1 - e^{-2\pi\kappa}}$$

eq. 2-22

In this estimate

$$\kappa = \frac{1}{\sqrt{\eta}} \quad \text{with} \quad \eta = \frac{E_{kin}}{E_K}$$

eq. 2-23

is the adiabaticity parameter. E_{kin} is the kinetic energy of a target electron in the rest frame of the projectile ion and E_K is the K-shell binding energy.

At high energies the results of this dipole approximation start to deviate and can be better approximated with the Sauter formula [BET77], which is derived within a relativistic first order treatment in αZ_I [ICH94], where α is the fine structure constant.

With increasing nuclear charge of the target materials the importance of non-radiative capture increases. In the NRC process the electron is transferred radiation less from a bound state in the target atom to a bound state in the projectile ion or continuum state in three body collisions. To match energy and momentum this process thus needs a third particle involved, namely the target nucleus.

The cross sections for NRC can be estimated by using the eikonal approach [EIM95]. In the case of the 1s-state an analytic integration gives the non-relativistic cross section scaling dependence

$$\sigma_{NRC} \sim \frac{Z_1^5 Z_2^5}{E_{kin}^5}.$$

eq. 2-24

In the relativistic regime the energy dependence asymptotically approaches a $1/E_{kin}$ dependence.

Comparing the two cross sections in fig. 2-10 for REC and NRC it can be seen that NRC dominates for high Z_2 targets whereas REC dominates for low Z_2 .

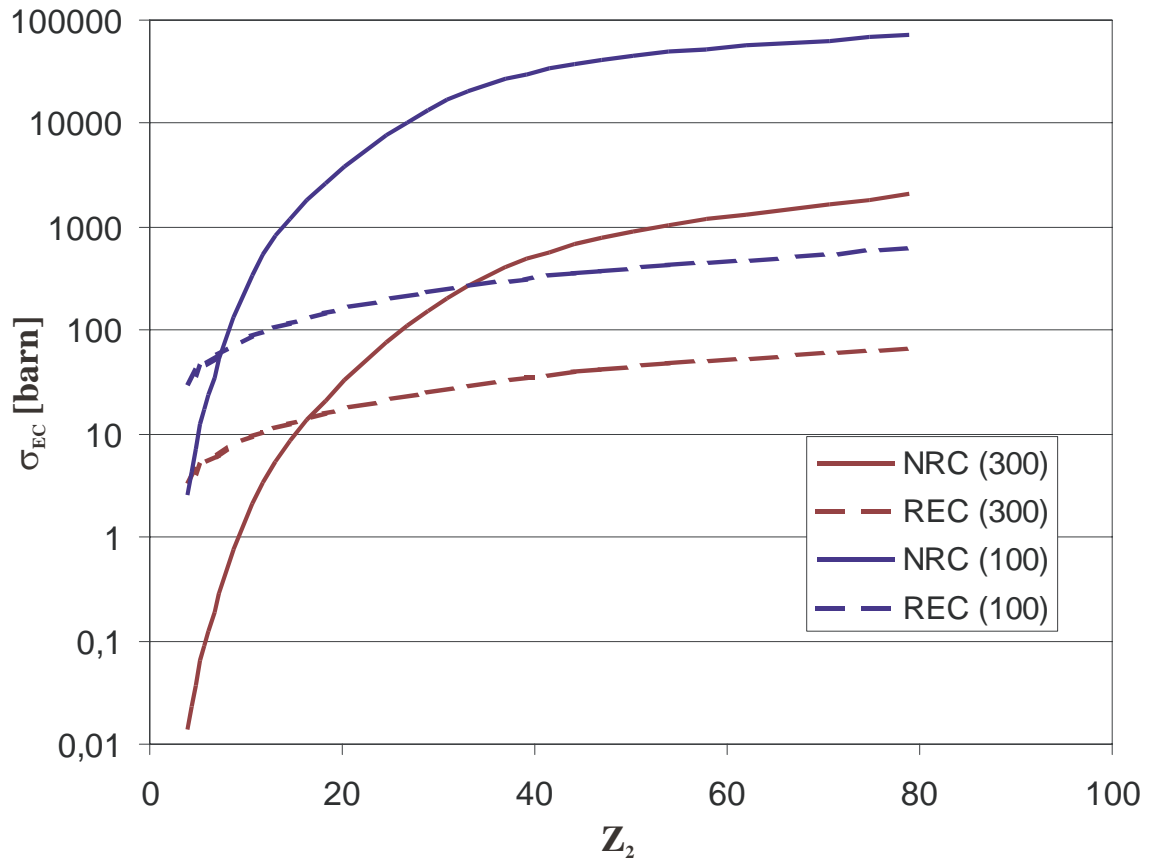


fig. 2-10 NRC and REC cross sections for the K-shell electrons of Ni ions with an incident energy of 300 and 100 MeV/u versus Z_2 .

2.3.1.3 The computer code GLOBAL

The computer code GLOBAL [SCH98] calculates charge-state distributions taking into account up to 28 charge states. It uses the Runge-Kutta method to solve the rate equation

$$\frac{dY_n(x)}{dx} = \sum_{n' \neq n} \sigma(n', n) Y_{n'}(x) - \sigma_{tot}(n) Y_n(x)$$

eq. 2-25

where Y is the number of ions in state n , x the penetration depth ($atoms/cm^2$), $\sigma(n', n)$ the cross section in cm^2 for a transition from projectile state n to state n' and

$$\sigma_{tot}(n) = \sum_{n' \neq n} \sigma(n, n')$$

eq. 2-26

is the total charge-changing cross-section for an ion with initially n attached electrons.

2.3.2 Energy loss

2.3.2.1 Basic quantities

In this chapter the mean energy loss ($\langle \Delta E \rangle$) per target thickness Δx will be treated. The specific energy loss or the so-called stopping power which essentially is a force is defined by:

$$\frac{dE}{dx} = \lim_{\Delta x \rightarrow 0} \frac{\langle \Delta E \rangle}{\Delta x}.$$

eq. 2-27

As the energy is lost this value is negative.

For high velocities ($\sim 1 \text{ MeV}/u$ and above) the energy loss of the charged projectile is mainly caused by inelastic collisions with the target electrons the so-called electronic stopping. The mechanism for energy loss is ionization and excitation of the target electrons.

For lower velocities

$$v < Z_P^{\frac{2}{3}} v_0, \text{ with } v_0 = \frac{e^2}{\hbar}$$

eq. 2-28

where Z_I is the charge of the projectile and v_0 is the Bohr velocity, elastic collisions with the target atoms start to play a role as seen in fig. 2-11, the so-called nuclear stopping.

The third process, namely the elastic collision with the target electrons is negligible due to the much higher mass of the nucleus compared to the electrons. In fig. 2-11 the elastic and inelastic specific energy loss of Nickel ions in a copper target is shown versus the energy of the projectile. One can clearly see the dominance of the electronic energy loss for energies larger than $1 \text{ MeV}/u$.

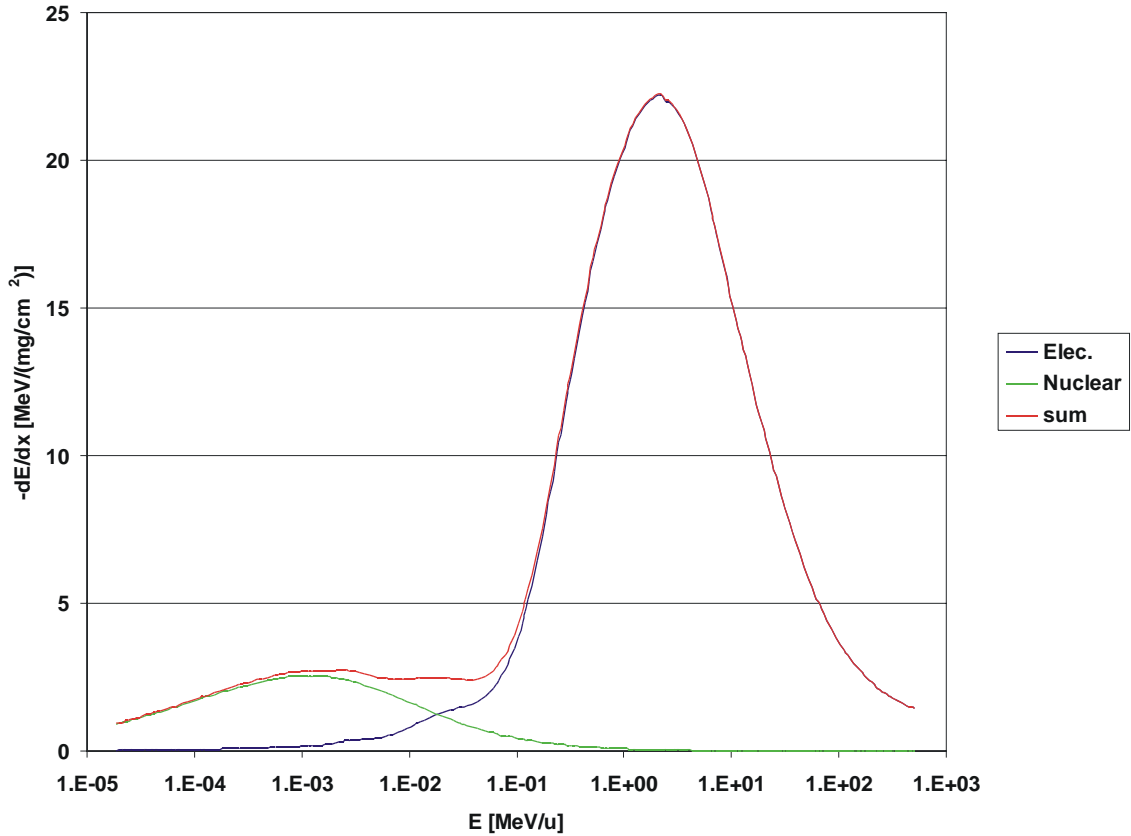


fig. 2-11 The contributions of nuclear and electronic stopping of ^{58}Ni ions in Copper depending on the energy of the projectile. The red curve shows the sum of the two contributions. For ^{58}Ni the Bohr criterion is $Z_1^{2/3} v_0 \approx 0.23 \frac{\text{MeV}}{u}$. This calculation was done using SRIM [ZIE85].

The total energy loss is the sum of the two contributions:

$$\frac{dE}{dx} = \left(\frac{dE}{dx} \right)_{nu} + \left(\frac{dE}{dx} \right)_{el}$$

eq. 2-29

The stopping process itself is a statistical process of many collisions and the interaction of the projectile with the target atoms depends on the energy regime. Since the energy transfer in a single collision is very small they can be treated as a quasi-continuous slowing down namely the continuous slowing down approximation (CSDA). The thickness d to reduce the initial energy E_{in} to E_{out} is then given by

$$d = \int_{E_{out}}^{E_{in}} \frac{1}{\frac{dE}{dx}(E)} dE .$$

eq. 2-30

The energy loss (ΔE) is therefore given by

$$\Delta E = E_{in} - E_{out} .$$

eq. 2-31

The energy-loss straggling is described by the standard deviation of σ_E with

$$\sigma_E^2 = \left\langle (E - \langle \Delta E \rangle)^2 \right\rangle.$$

eq. 2-32

In order to stop the beam the most important quantity is the range of the projectiles. Using eq. 2-30 the range can be calculated as the thickness to reduce E_{out} to zero

$$r(E_i) = \int_0^{E_i} \frac{1}{\frac{dE}{dx}(E)} dE.$$

eq. 2-33

As the influence of angular straggling for relativistic heavy ions along the projectiles trajectory is small the integral of the range is almost identical to the projected range. The longitudinal distribution the range straggling σ_R can be calculated approximately by using the differential energy straggling $\frac{d\sigma_E^2}{dx}$ and the stopping power $\frac{dE}{dx}$ as

$$\sigma_R^2 = \int_{E_m}^0 \frac{d\sigma_E^2/dx}{\left(\frac{dE}{dx}\right)^3} dE.$$

eq. 2-34

2.3.2.2 Classical calculation

The theory developed by Bohr [BOH13][BOH15] starts by viewing each collision independently from the others and the total energy loss as a statistical process. The target material is made up initially by a random assembly of independent classical electrons bound harmonically to the nuclei.

The stopping media contains N interaction centers distributed evenly over a volume unit. A monoenergetic ensemble of projectiles undergoes a mean energy loss $\langle \Delta E \rangle$ in the target with the thickness Δx :

$$\langle \Delta E \rangle = N\Delta x \int T d\sigma$$

eq. 2-35

Herein $N\Delta x$ is small enough to guarantee the condition of uncorrelated single collisions and T is the energy transfer in a single collision and $d\sigma$ is the cross section for the collision to occur. With the Coulomb potential as interaction potential the mean energy loss becomes

$$\langle \Delta E \rangle = 2\pi N\Delta x \cdot \frac{q_1^2 q_2^2}{m_2 v^2} \cdot \int_{T_{\min}}^{T_{\max}} \frac{dT}{T},$$

eq. 2-36

where q_1 and q_2 are the charge of the projectile and the target respectively, and M_T is the mass of the target material. The upper integration interval T_{max} is the maximum energy transfer in a single collision.

$$T_{max} = \frac{2m_1^2 m_2}{(m_1 + m_2)^2} v_1^2$$

eq. 2-37

The integration interval T_{min} cannot be zero to avoid the integral from diverging. Bohr [BOH13][BOH15] described the electron binding classically as oscillating dipoles and calculated the energy transfer separately for close and distant collisions. In the close collisions with large energy transfers the binding energy of the electrons is not taken into account. In the distant collisions the electromagnetic excitation of the dipole and the associated energy loss is calculated. The border between the two regions is chosen such, that it is much larger than the mean atomic radius yet it is small enough so the revolution frequency of the electrons is still much smaller than the time for the collision to avoid the collision becoming adiabatic [BOH48].

Taking the excitation in this way into account the integral converges for the distant collisions and it leads to the Bohr formula for the mean energy loss

$$\left(\frac{dE}{dx} \right)_{Bohr} = \frac{4\pi Z_1^2 e^4}{m_e v_1^2} N \ln \left(\frac{1.123 v_1^3 m_e}{Z_1 e^2 \bar{\omega}} \right).$$

eq. 2-38

It is assumed here that the projectile has the charge $Z_1 e$ with e being the electron charge and m_e the electron mass. Z_2 is the proton number of the target and N the number of collision centers (essentially the number of electrons) given by $N = N_a Z_2$ with N_a being the atomic density. The projectile has the velocity v_P and $\bar{\omega}$ is the mean oscillator frequency of the electrons.

A more modern approach, the so called binary stopping theory [SIG02], uses a starting point very similar to that of Bohr, but incorporates a lot of new features. Like the Bohr model it allows for static projectile screening and intrinsic motion of target electrons by adding correction terms but it does not need the formal distinction between close and distant collisions. It is an exact theory without using the dipole approximation and automatically includes the correct Z_1 dependence.

The central feature of the binary theory is to replace the harmonic binding by a potential including screening. The energy transfer thus is calculated in a binary collision using a Yukawa potential,

$$V(r) = -\frac{Z_1 e^2}{r} e^{-\frac{r}{a_{ad}}}, \quad a_{ad} = \frac{v_1}{\omega}$$

eq. 2-39

with ω being the resonance frequency of a harmonically bound electron and r the distance. This approach reproduces the predictions of the Bohr theory for a point charge in the limit of large impact parameters. The actual calculation is done by numerically evaluating classical scattering integrals for the potential in eq. 2-39 for all impact parameters.

Based on this theory the computer code PASS [SIG02] was developed to calculate the stopping number L as a function of the Bohr variable $\xi = mv^3 / Z_1 e^2 \omega$ where $\omega = I / \hbar$. I is the ionization potential of the target material listed in [ICR94].

2.3.2.3 Quantum mechanical treatment

In general the electronic stopping is very well described by the following expression:

$$\left(\frac{dE}{dx} \right)_{el} = 4\pi N \frac{Z_1^2 e^4}{m_e c^2 \beta^2} Z_2 L,$$

eq. 2-40

in which N is the density of the target atoms, m_e the electron mass, e the electron charge and βc is the velocity of the projectile. For velocities $v \gg Z_p v_0$ perturbation theory like the 1st Born approximation can be used. In the relativistic description by Bethe [BET32] the stopping number L is given by:

$$L_B = \ln \left(\frac{2m_e c^2 \beta^2}{I(1 - \beta^2)} \right) - \beta^2,$$

eq. 2-41

where I is again the mean ionization potential. Again the collisions are, like in the classical treatment by Bohr, subdivided in close collisions (free e^-) and distant ones (harmonic oscillator).

To this basic ansatz further correction terms are added which are briefly described in the following paragraphs.

The Bloch and Mott correction

The Bloch correction was derived by Bloch [BLO33] in an investigation of the similarities and differences between classical and quantum-mechanical range-energy calculations. He introduced a correction term to account for the difference to the exact treatment of low energy collisions. By this one obtains a smooth transition to the Bohr formula [SIG98].

The Mott correction describes the influence of the magnetic interaction in relativistic heavy ion collisions where the perturbation theory fails. Using higher order calculations as described in [AHL78] one obtained another correction term for L .

The treatment in the LS-theory [LIN96] is an exact calculation and incorporates these two corrections. The LS-theory at the low energy limit is exactly the Bloch correction. And by using the exact solutions to the Dirac equation, the LS-correction automatically incorporates Mott scattering and is relativistically correct. Still the Bethe theory is used for collisions with low energy transfer but the exact solution for close collisions with quasi-free electrons. The formalism in the LS-theory calculates the phase shifts in scattering of partial waves and directly calculates the difference to the Bethe result.

$$\Delta L_{LS} = L - L_{Bethe}$$

eq. 2-42

The shell correction

Bethes' result for the logarithmic factor in the stopping power eq. 2-40 needs the assumption that the excitation and ionization process is independently possible for all oscillator strengths. This assumption is introduced by the mean ionization potential I . For energy transfer reactions in the order of the binding and excitation energy this assumption is not valid and I ceases to be a constant. For this reason one introduces additive correction terms to the stopping power

$$\Delta L_{Shell} = -\frac{C}{Z_2},$$

eq. 2-43

with Z_2 as the charge of the target. C is a velocity dependent parameter summed over all shell correction parameters for each shell (K, L, M) of the form

$$C(v) = C_K(v) + C_L(v) + C_M(v) + \dots$$

eq. 2-44

and goes to zero for high velocities. As with reduced energy less and less electrons contribute to the stopping process the shell correction reduces the stopping power. Values for the shell correction parameter C are tabled in [BAB64] and [ICR94].

The density effect

In the description of the energy loss it was assumed so far that only one target atom interacts with the projectile at a time. Yet this is of course a simplification not true especially for dense media and for collisions with large impact parameters where there can be many atoms situated in between the projectile and the interacting target atom. Therefore, the density effect is a screening effect occurring at distant collisions for relativistic velocities due to the dielectric polarization of the target atoms. Qualitatively the density effect can be derived from classical electrodynamics as it may be found in classical electrodynamics textbooks like [JAC75]. Theoretically it was first investigated by Fermi in 1940 [FER40]. Its magnitude has been calculated by Fermi and extended by Sternheimer and Peiels [STE71]. For high velocities the density effect correction has the form

$$-\frac{\delta}{2} = -\ln(\beta\gamma) + \ln \frac{I}{\hbar\omega_p} + \frac{1}{2},$$

eq. 2-45

where ω_p is the plasma frequency of the medium. The density effect therefore reduces the relativistic rise in eq. 2-40 from $\sim \ln \gamma^2$ to $\sim \ln \gamma$ and substitutes the plasma frequency in the correction term for the mean ionization potential. At lower energies the density effect becomes more complicated, but one can obtain a parametric fit to the full density effect as developed by [STE71]. A more recent tabulation of the parameters can be found in [STE84].

The Barkas effect

The last contribution to the corrections in the stopping power calculations is the Barkas effect discovered by Smith et al. [SMI53] in the investigation of π^+ and π^- ranges. This effect arises due to the polarization of the target electron gas by the projectile. It is strongest at projectile energies near the electron velocity i.e. 25 keV for protons. As negative projectiles suffer less collision this effect lowers the stopping power of negative projectiles.

It was concluded by Jackson and McCarthy [JAC72] that the target polarization effects for low-energy distant collisions would produce a multiplicative correction to the energy loss, that is

$$\frac{dE}{dx} \rightarrow \frac{dE_{Barkas}}{dx} = \frac{dE}{dx} \left(1 + \frac{Z_1}{\sqrt{Z_2}} F(V) \right).$$

eq. 2-46

The variable V is a reduced momentum defined by

$$V = \frac{\beta \cdot \gamma}{\alpha \cdot \sqrt{Z_2}}.$$

eq. 2-47

The function F(V) is a ratio of two integrals over a Thomas-Fermi model of the atom and can be found in [JAC72]. It was shown later by Lindhard [LIN72] that this function F(V) should be multiplied by 2 for close and distant collisions and a better agreement between theoretical results and experimental data.

Including all these corrections the stopping number L becomes

$$L = L_{Bethe} + L_{LS} + L_{shell} + L_{Barkas} - \frac{\delta}{2}$$

eq. 2-48

2.3.2.4 Energy loss at medium velocities

At relativistic energies the projectile charge is simply the charge of the nucleus. For velocities around $v \approx Z_p v_0$ bound electrons become important. The resulting mean charge as discussed in chapter 2.3.1 is determined by the equilibrium of ionization and electron capture (EC). Many codes use semi empiric formulas to approximate q_{eff} [ZIE85][BRA82]. Once the effective charge is known one can calculate the energy loss from the energy loss of the proton which is measured for a large energy range and for many different target materials with the so called scaling formula with the effective charge q_{eff} as defined in eq. 2-17 where the energy loss of the heavy ion

$$\frac{dE}{dx}(Z_1, v) = q_{eff}^2 \frac{dE}{dx}(Z_1 = 1, v)$$

eq. 2-49

scales with the energy loss of a proton times the squared effective charge. The hereby obtained specific energy loss is accurate in the order of 15% [ZIE85] [HUB80].

2.3.2.5 Energy loss at low velocities

For velocities lower than the Bohr criterion ($v < Z_1^{\frac{2}{3}} v_0$) thus for velocities below the Bragg peak the electronic energy loss is proportional to the projectile velocity. According to the theory by Lindhard and Scharff the electronic energy loss in this regime is given by [LIN68]:

$$\left(\frac{dE}{dx}\right)_{el} = 8\pi N e^2 a_0 Z_1^{\frac{1}{6}} \frac{Z_1 Z_2}{\left(Z_1^{\frac{2}{3}} + Z_2^{\frac{2}{3}}\right)^{\frac{3}{2}}} \frac{v}{v_0}.$$

eq. 2-50

As in this energy regime the projectile already carries many electrons one cannot treat it as a point like charge any more, even worse the electron clouds of the projectile ion and the target atom can overlap. For this reason one uses the Thomas-Fermi approximation and to include the influence of this overlap.

But of course in this velocity regime the contribution to the energy loss by elastic collisions of the projectile with the target nucleons is no longer negligible. Ziegler derived by using Hartree-Fock calculations that the nuclear energy loss depending on the kinetic energy E of the projectile is given by

$$\left(\frac{dE}{dx}\right)_{nu} = \frac{8.462 \cdot 10^{-15} Z_1 Z_2 A_1 s_n(\varepsilon)}{(A_1 + A_2)(Z_1^{0.23} + Z_2^{0.23})},$$

eq. 2-51

with the reduced energy

$$\varepsilon = \frac{32.53 A_2 E}{(A_1 + A_2) Z_1 Z_2 (Z_1^{0.23} + Z_2^{0.23})}$$

eq. 2-52

and the functional for the stopping power cross section

$$s_n(\varepsilon) = \frac{0.5 \cdot \ln(1 + 1.1383 \cdot \varepsilon)}{\varepsilon + 0.01321 \cdot \varepsilon^{0.21226} + 0.19594 \cdot \varepsilon^{0.5}} \quad \text{for } \varepsilon \leq 30$$

$$s_n(\varepsilon) = \frac{\ln \varepsilon}{2\varepsilon} \quad \text{for } \varepsilon \geq 30$$

eq. 2-53

2.3.2.6 The computer code ATIMA

ATIMA is a program developed at GSI which calculates various physical quantities characterizing the slowing-down of protons and heavy ions in matter for specific kinetic energies ranging from 1 *keV/u* to 500 *GeV/u* such as

- stopping power,
- energy loss,
- energy-loss straggling,
- angular straggling,
- range,
- range straggling,
- and beam parameters (magnetic rigidity, time-of-flight, velocity, etc.).

Above 30 *MeV/u* the stopping power is obtained from the theory by Lindhard and Sørensen (LS) including the following corrections: the shell corrections, a Barkas term and the Fermi-density effect. The projectiles are treated as point-like particles of a mean charge. Below 10 *MeV/u* a modified version of Ziegler's SRIM [ZIE85] is used. In the intermediate energy range a interpolation between the two is used. The LS theory differs substantially for ions with high *Z* from the Bethe formula it also considers the nuclear size effect for very relativistic ions. Energy-loss straggling comes also from the LS-theory above 30 *MeV/u*. Below 10 *MeV/u* the theory of Firsov [FIR57] and Hvelplund [HVE71] is used. The mean charge of the projectiles is calculated by the formula of Pierce and Blann eq. 2-19.

3 Experiment

The goal of this experiment was to measure the charge-state distribution, energy loss, and energy-loss straggling from 500 MeV/u down to energies of 40 MeV/u . For the measurement six different target materials, Be, C, Al, Cu, Ag and Au, with different thickness each corresponding to roughly 10%, 20% and 30% energy loss were used. The energies of the primary beam delivered from the heavy ion synchrotron SIS18 was 500, 300, 100, and 50 MeV/u for the ^{136}Xe beam and 300, 100, 70, and 50 MeV/u for the ^{58}Ni beam.

3.1 Slowing down experiment with ^{58}Ni and ^{136}Xe ions

The Fragment Separator FRS as an energy-loss spectrometer is an ideal tool to measure charge state distributions, energy loss and energy-loss straggling. The following chapters will describe the method used for this experiment and the ion optical mode used for these measurements as well as the detectors and targets. The basics about the in-flight technique, fragment separators especially the FRS and the $B\rho - \Delta E - B\rho$ separation method were already described in chapter 2.2.2.

3.1.1 Ion-optical mode

For the slowing down experiments the FRS was used in its standard achromatic mode [GEI92] as shown in fig. 3-1. As only primary beam was used there was no production target at TA, but a stripper to get fully stripped incident ions.

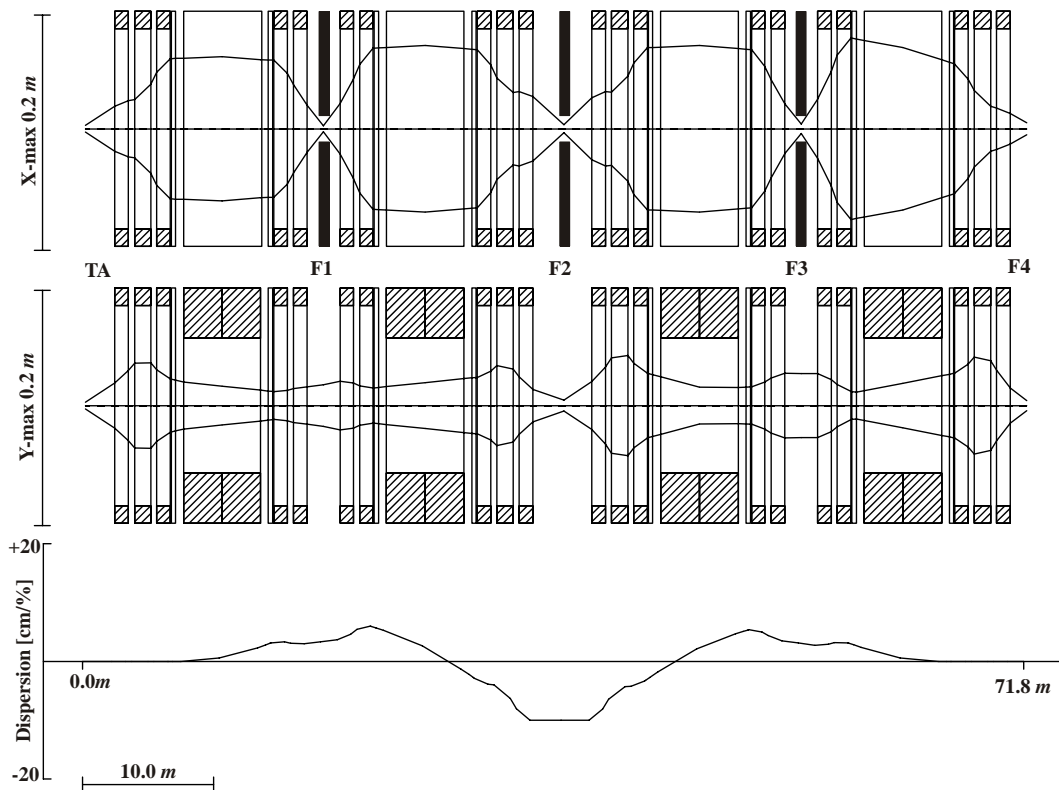


fig. 3-1 The FRS in achromatic standard ion-optical mode. The upper two plots show the beam envelope in x- and y-plane for an incident phase space of $\varepsilon = 20 \pi \text{ mm} \cdot \text{mrad}$. The lower plot shows the dispersion curve for this standard achromatic mode.

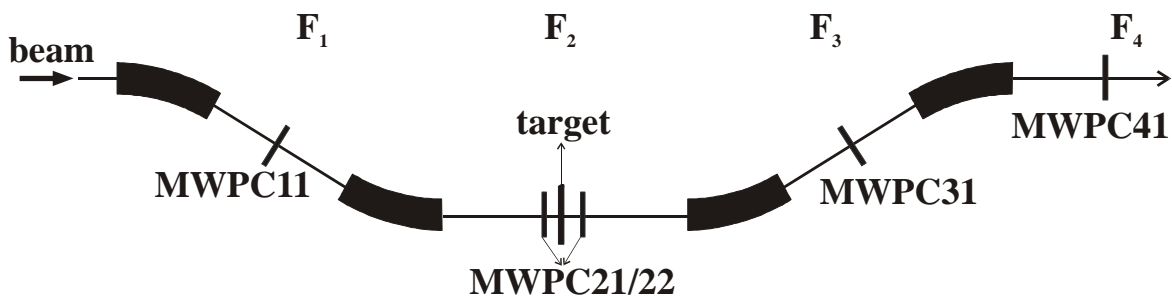


fig. 3-2 Positions of the Multi wire proportional chambers (MWPC) for the charge-state and energy-loss measurements. For the charge-state distribution measurements MWPC31 was used. The energy loss for the materials placed at F2 was determined at F3 and F4 using MWPC31 and MWPC41 respectively.

The different targets were placed at the second focus F2 behind a collimator as shown in fig. 3-1. The positions of the Multi Wire Proportional Chambers (MWPC) described in chapter 3.1.2.2 to measure the charge-state distributions and energy loss data are shown in fig. 3-2. The charge state distribution measurements were done using the MWPC31 at the third focus F3. The energy loss measurements were done at F3 and F4 by also using these MWPCs. All energy straggling data were taken with the MWPC41 in an optics mode with a focal length of only 590 mm behind the last quadrupole to avoid the additional contribution to the peak width from angular scattering in the exit window. The overview of the detector setup behind the last Multi wire as it was used for all range focusing experiments is shown in fig. 3-3.

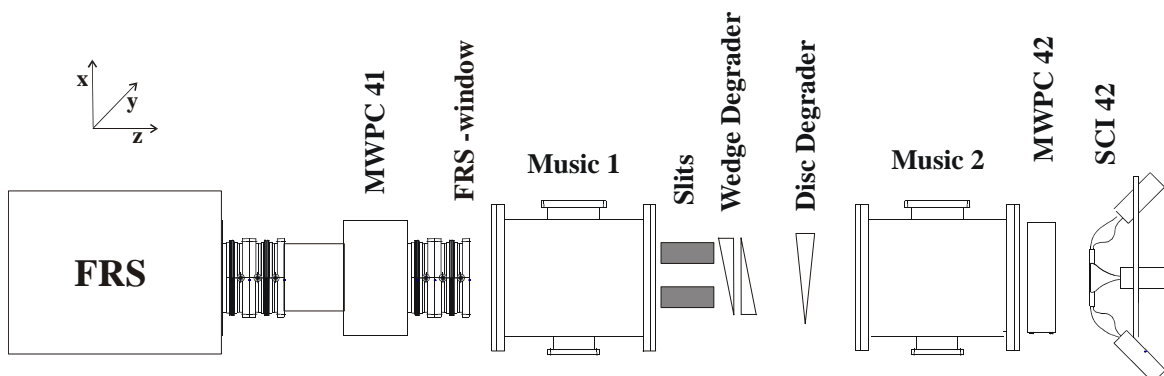


fig. 3-3 Detector setup at the end of the FRS. The detectors mounted are MUSICs, MWPCs and scintillators. For the slowing down experiments the beam focus was on the MW41 just 590 mm behind the last quadrupole. For the range focusing experiment the focus was on the disc degrader mounted between the two MUSICs.

3.1.2 Detectors

Three types of detectors are in standard use for experiments at the FRS. These are the Multi Wire Proportional Chamber (MWPC) mounted on mechanical feed through to move them in and out of the beam at each focal plane of the FRS, the scintillators for Time Of Flight (TOF) measurements and Multi Sampling Ionization Chambers (MUSIC). They are commonly used to identify the projectiles by their energy loss.

3.1.2.1 Multi sampling ionization chamber MUSIC

The **M**ultiple **S**ampling **I**onization **C**hamber (MUSIC) [PFÜ94] is an ionization chamber filled with P10 gas (90% Ar, 10% CH₄) at about room temperature and normal pressure. The entrance and exit windows are made from 25 μm Kapton (C₂₂-H₁₀-O₅-N₂)_n with a density of 1.4 g/cm² coated with 40 $\mu\text{g}/\text{cm}^2$ Al. The diameter of the windows is 450 mm. Depending on the high voltage applied the drift velocities of the electrons reach about 5 cm/ μs .

When an ionizing particle penetrates through the gas, a cloud of electrons and ions is generated and by means of an applied electric field the charged particles drift towards the cathode (positive ions) and to the six-fold segmented anode (electrons). Using charge-sensitive preamplifiers, the charge of the electrons arriving at each anode is converted into a voltage which is proportional to the number of electrons. Since this number is roughly proportional to the square of the charge of the penetrating particle, the output voltage of the preamplifier is a measure for the atomic number of this particle. The preamplifier output signal is further increased and shaped by a main amplifier and digitized by an ADC and further on handled by the data-acquisition system. From the six available anodes only the signals of the middle four anodes are used. The first and the last anode serve for homogeneity of the electric field and are only connected to the high voltage.

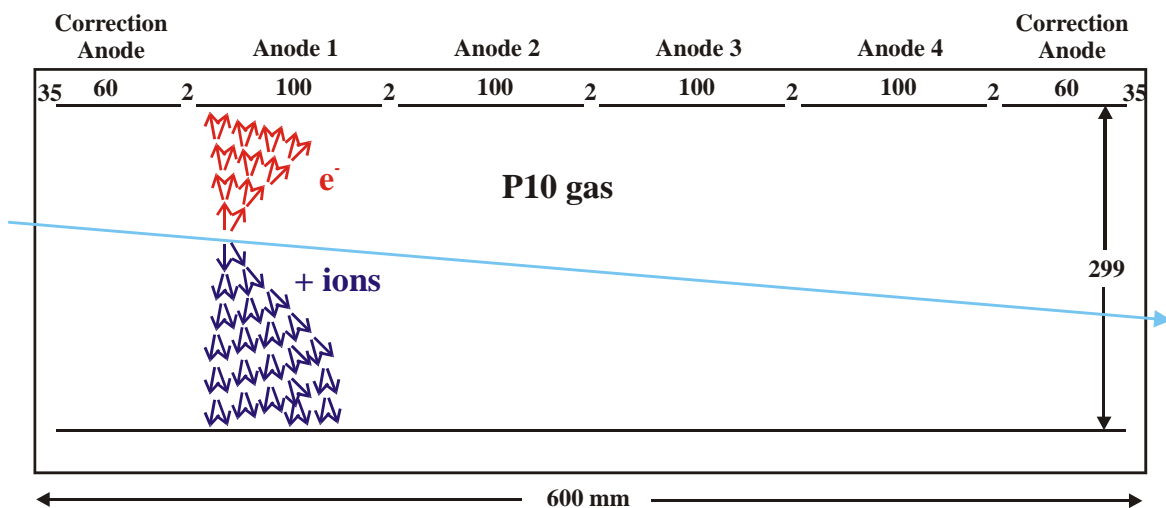


fig. 3-4 Scheme of the multiple sampling ionization chamber (MUSIC). All measures are in mm.

Using an additional, fast detector as a start trigger for a TAC or a TDC, the drift time of the electron cloud provides information on the x -position of the passing particle. The stop signal for the TAC or for the TDC can be derived from the output of the preamplifiers, shaped accordingly with a timing-filter amplifier.

3.1.2.2 Multi wire proportional chambers

The multi wire proportional chambers MWPCs [STE91] are well suited for a wide range of ions to measure their positions. At the FRS about 10 of this type of detectors are routinely used for beam tracking.

A schematic layout of a MWPC is shown in fig. 3-5. The plane labeled A is the anode plane, consisting of 20 μm gold-plated tungsten wires with a distance of 2 mm. The cathode X- and Y-plane are made of 50 μm gold-plated tungsten wires with a distance of 1 mm. The wire direction of the two cathodes X and Y are orthogonal to each other while the

anode wires are diagonal in a 45° angle. The spacing between the cathodes and the anode is 5 mm respectively. A pre-gap can be used to increase the amplification for low charged ions, but was not used in the present experiment.

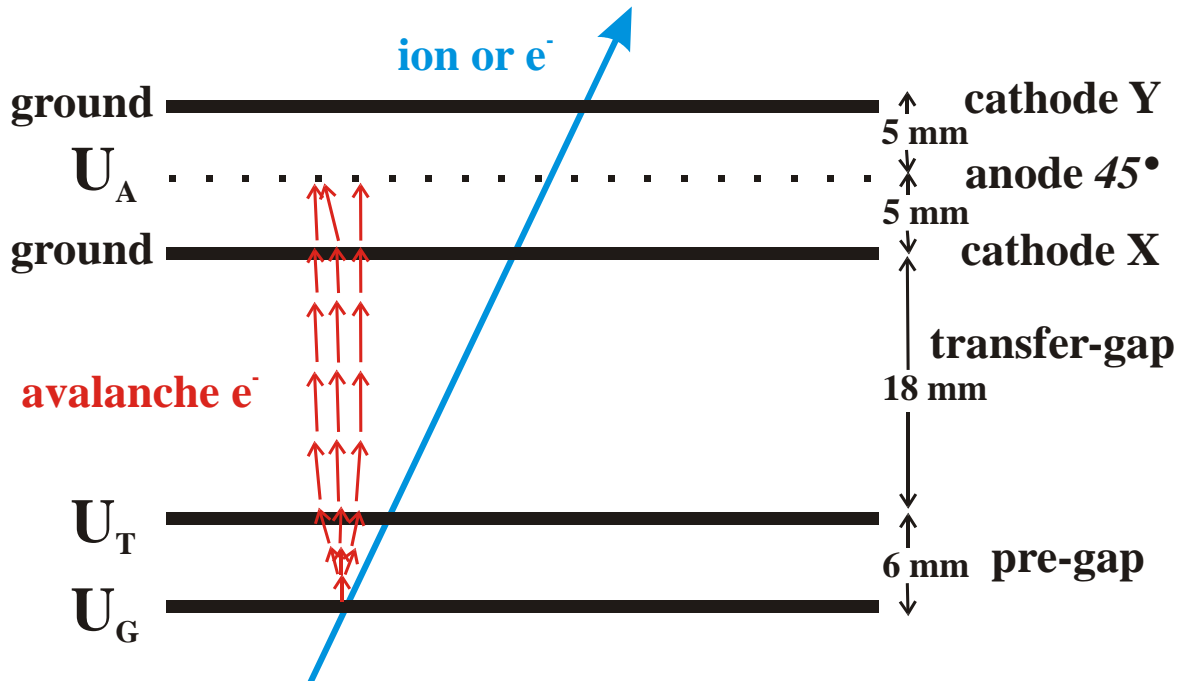


fig. 3-5 Schematic layout of a the multi wire proportional chamber [STE91].

The two read out cathodes X and Y are on ground potential. This type of MWPC with a two-stage gas amplification exhibit a much better time-resolution than an ordinary MWPC ($\sim 10\text{ ns FWHM}$). The gas used is a mixture of 86% Argon and 14% CO_2 with some admixture of alcohol. The windows are made from Ti with a thickness of $2 \cdot 100\ \mu\text{m} = 2 \cdot 45\ \text{mg}/\text{cm}^2$. The detectors cover an area of $200 \cdot 200\ \text{mm}$ with a position resolution of about $0.5\ \text{mm}$.

An ionizing particle hitting the active area of the chamber produces primary electrons in the chamber gas. In the so called pre-amplification gap or simply pre-gap they are multiplied due to the high electric field gradient. The gain here is of the order of 100. The electrons then are following the low electric field gradient through the transfer gap to the first cathode plane with an transfer efficiency of about 15% . Finally the avalanche reaches the anode plane and there a second gas amplification by about a factor 10^3 takes place. Due to the long drift path the electron cloud broadens by transverse diffusion and typically 2 adjacent anode wires carry the signal.

The readout is done with the so called delay-line technique. Each wire of the X and Y plane is connected to a $4\ \text{ns}$ delay line. The signal propagates through the left and the right side of the delay line and thus their time difference is a measure for the position while the sum of them is a constant. This fact is used for background suppression.

3.1.3 Targets

The targets used for the slowing down experiments were mounted on three different ladders at the second focal plane (F2) of the FRS shown in fig. 3-6.

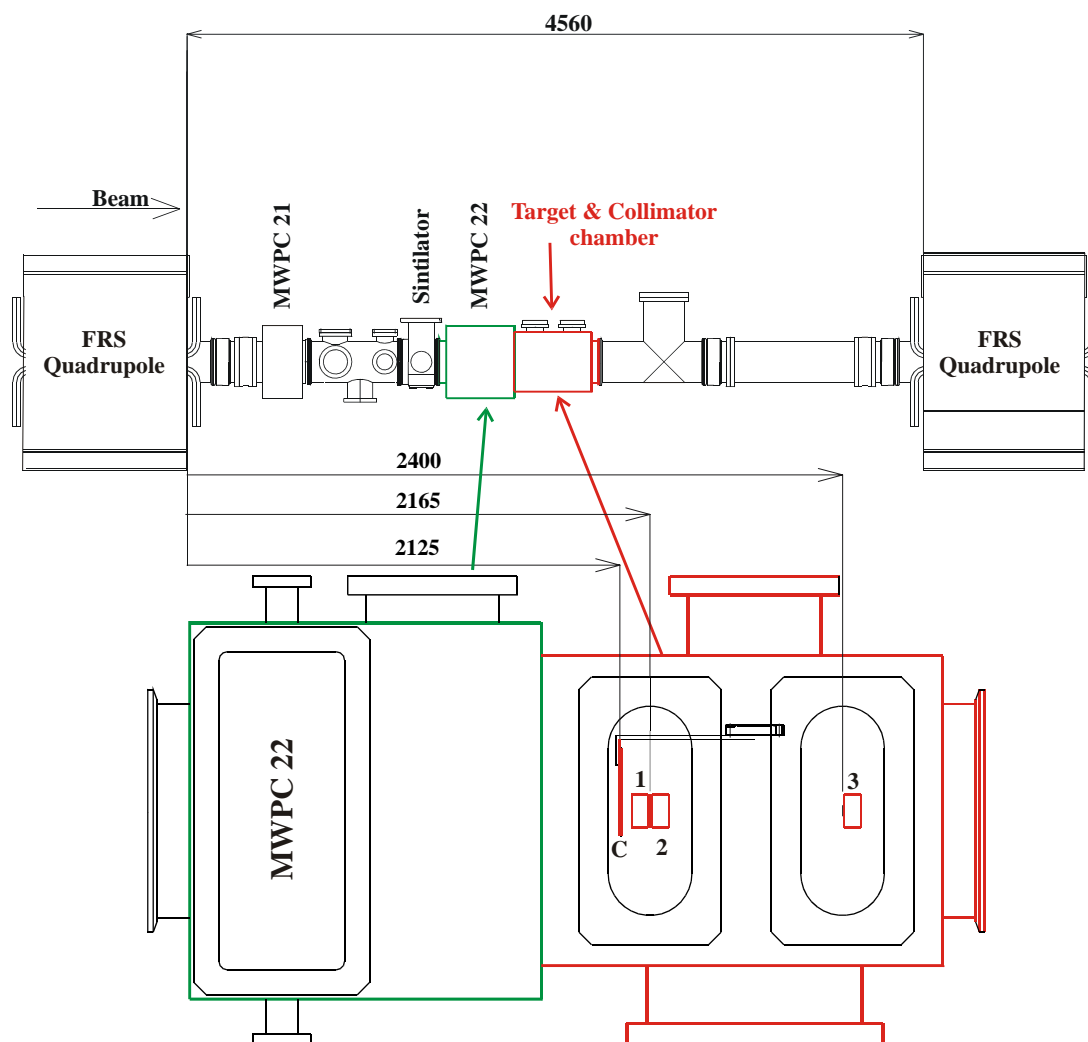


fig. 3-6 Side view of the second focal area of the FRS (top) and a zoomed in top view of the target chamber at the bottom. The collimator C was placed at the focus, 2125 mm after the quadrupole. The distance between ladder 1 and 2 was 4 mm while the target ladder 3 was 275 mm away from the collimator and thus from the focal plane. Just before the targets and collimator chamber a MWPC for beam monitoring could be inserted.

A summary of all targets mounted is given in the Appendix A. Ladder 1 and 2 were only 4 mm apart and were used also to stack targets for more possibilities in thickness variation. Ladder three only contained very thin Gold foils and all Silver targets. Due to its distance of about 25 cm to the other ladders it was not feasible to stack those targets because of the angular straggling in the first. Each ladder had 21 available positions and could be moved out of the beam completely. Ladder 1 and 3 also had an empty slot to measure the possible influence of the target ladder on the beam quality.

The thickness of the targets was measured in the target lab at GSI and two complementary methods were used. The thickness was directly measured using a kind of caliper in 2 mm steps in x - and y -direction on the surface. The mean of those measurements is one value used for the actual target thickness. The other method is to obtain the surface area via the diameter of the target. This is measured in 8 times 45° steps. Together with the weight and the known density of the target one can calculate the areal weight. The errors of the thickness and diameter values are the standard deviations and for the weight the maximum error of the used scale in this range was used.

3.1.4 Data analysis

This chapter describes the methods of the measurements and how the data were analyzed. For each measurement method there is one complete example described. The overall results on the slowing down experiments are then summarized and discussed in chapter 4.1 and a complete list of all results are shown in tables in the appendix B.

3.1.4.1 Charge-state distribution

The charge state distributions were measured by counting the ions in each peak belonging to one charge state at the third focus F3. In those cases where the charge-state distribution was too broad to fit at once into the acceptance of the FRS the spectra were taken in several magnetic settings and normalized to an abundant peak common to the two histograms. All targets were thick enough to guarantee equilibrium conditions. In fig. 3-7 an example of a ^{58}Ni at $50\text{ MeV}/u$ beam impinging on a $41\text{ mg}/\text{cm}^2$ Cu target is shown. For this measurement it was necessary to rescale the FRS two times, thus taking three snapshots, in order to get the full distribution.

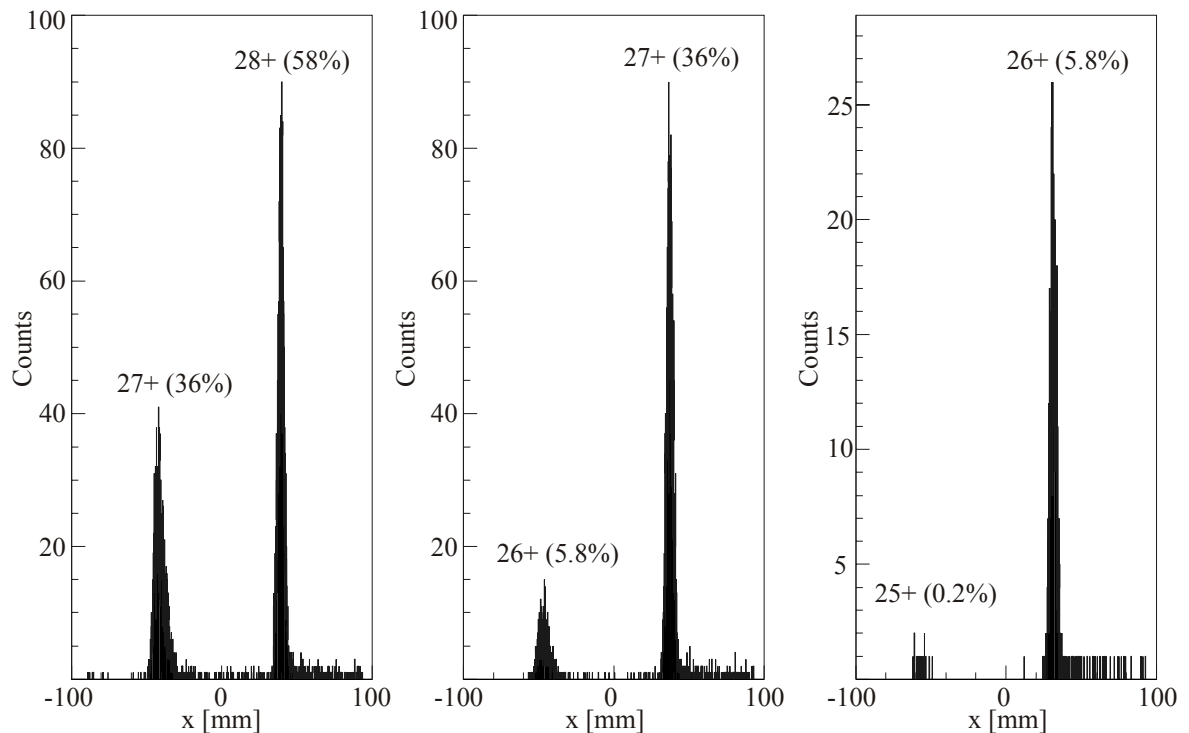


fig. 3-7 Charge state distribution at F3 for Ni at $50\text{ MeV}/u$ beam on a $41\text{ mg}/\text{cm}^2$ Cu target. As the charge-state distribution is too wide to fit at once into the acceptance window of the FRS three $B\rho$ -settings were taken. The percentage given for each peak is already the fraction normalized to the total intensity.

From these measurements one obtains the charge-state distribution for each target combination. In fig. 3-8 the measurement of ^{58}Ni at $50\text{ MeV}/u$ on all three Cu targets is summarized and compared to the predictions of the computer code Global.

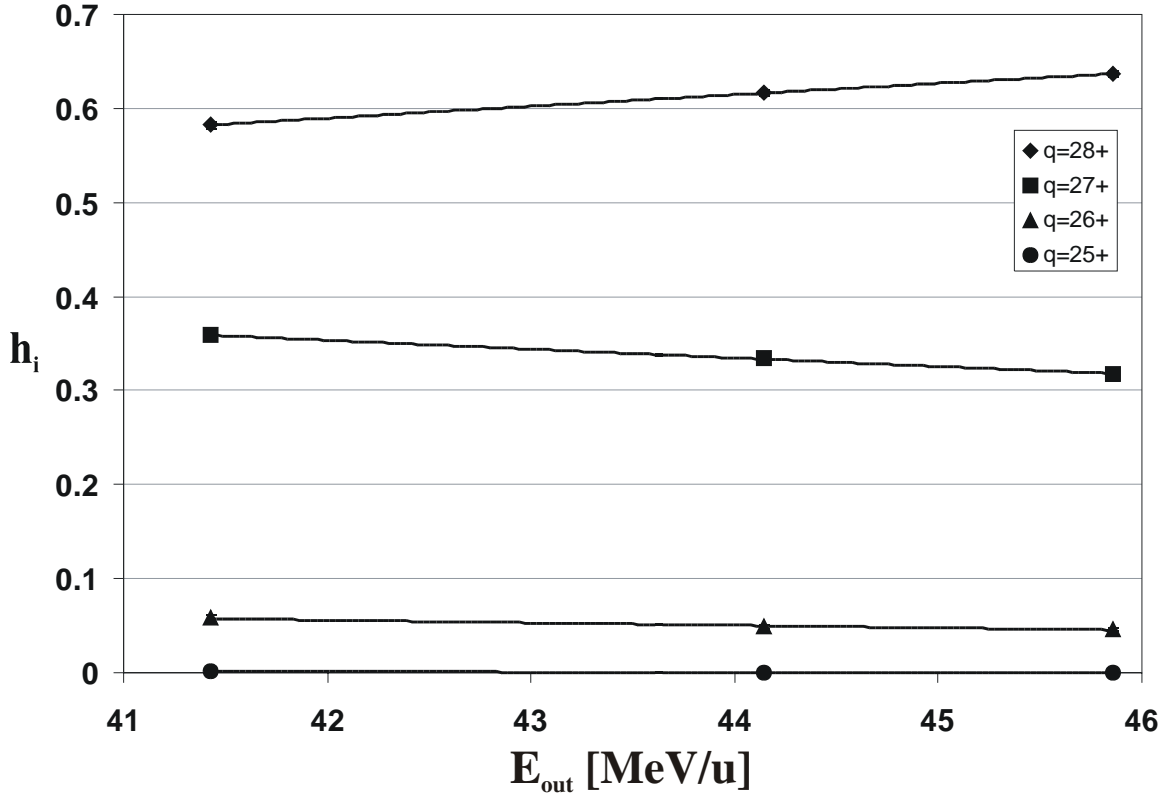


fig. 3-8 This plot shows the charge-state distribution of a 50 MeV/u Ni beam behind Cu targets of different thickness. The measured charge-state ratios are plotted versus the beam energy behind the targets. The lines are to guide the eye.

The abundance of each charge state was determined by

$$h_i = \frac{N_i}{N} \text{ with } N = \sum_j N_j$$

eq. 3-1

where h_i is the relative abundance of each charge state, N_i is the number of counts in one specific charge state and N is the sum of all counts in all charge-state peaks. From this the error was calculated as

$$\Delta h_i = \Delta N_i \frac{\partial h_i}{\partial N_i} = \left(\frac{1}{N} - \frac{N_i}{(N)^2} \right) \cdot \sqrt{N_i}$$

eq. 3-2

From these measured charge-state distributions the mean charge \bar{q} is calculated which is a common quantity used to predict energy losses. The mean charge is the normalized sum of the weighted abundances of each charge state q_i .

$$\bar{q} = \frac{\sum_i q_i N_i}{N}$$

eq. 3-3

The error of the mean charge state was calculated as

$$\Delta\bar{q} = \sum_i |q_i - \bar{q}| \cdot \frac{\sqrt{N_i}}{N}$$

eq. 3-4

where \bar{q} is the mean charge, q_i is the charge state corresponding to peak i , N_i are the counts in peak i and N is the sum of counts in all peaks. The mean charge for Ni on Cu is plotted in fig. 3-9 versus the exit energy for all energies measured and compared to the predictions of the computer code GLOBAL [SCH98].

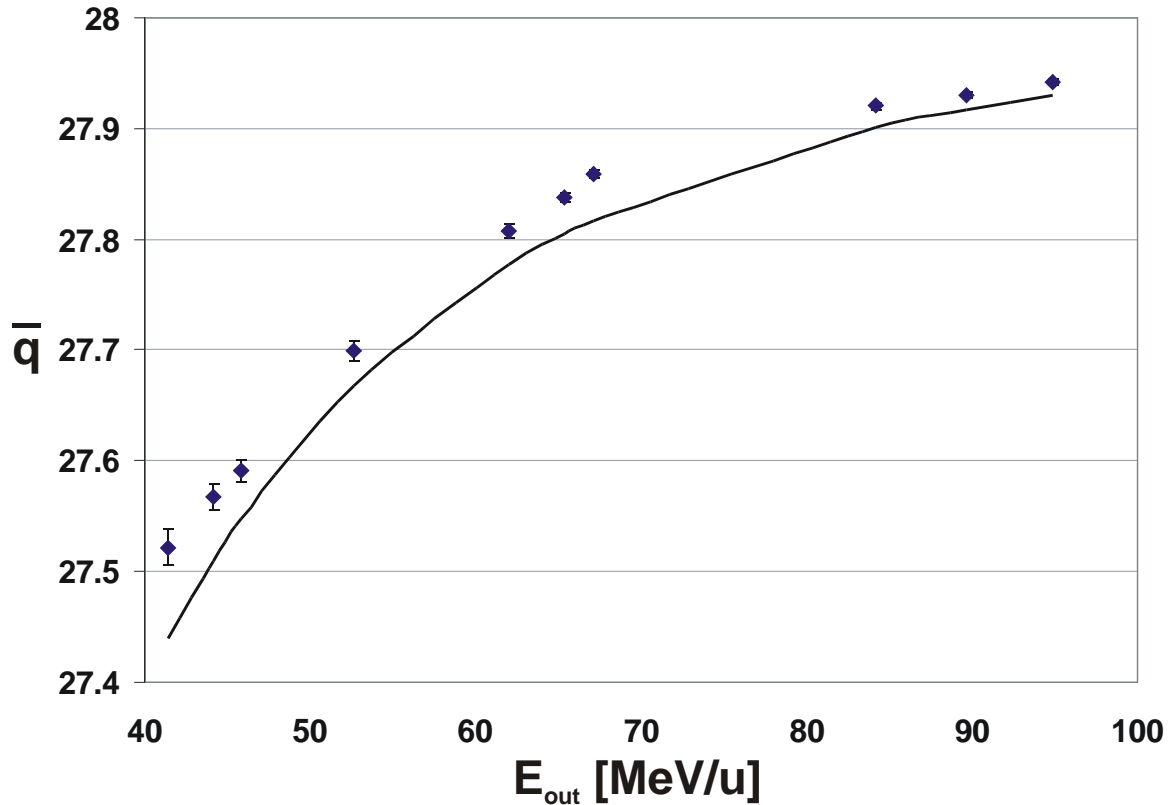


fig. 3-9 Mean charge of Ni projectiles as a function of energy behind all measured Cu targets. The solid line represents the prediction by the computer code GLOBAL [SCH98].

3.1.4.2 Energy loss

The energy loss was determined via the magnetic rigidity. This is calculated from the magnetic fields, from the beam position and from the measured dispersion. For each beam energy the primary beam was centered first at F3 without a target at F2 having a magnetic rigidity ($B\rho_0$). After that a target was placed at the second focal plane F2, the magnets were scaled to a new magnetic rigidity such that the beam was again centered on the detector except for a little displacement. This principle is illustrated in fig. 3-10. The scaling procedure relies on changing the magnetic rigidity ($B\rho$) while keeping the deflection angle (ϕ) constant. The deflection angle is proportional to the integrated magnetic flux density along the ion optical axis.

$$\phi = \frac{\int B(l)dl}{B\rho}$$

eq. 3-5

It is common to replace the geometrical length of the magnet (L) in the integral in eq. 3-5 by an effective length L_{eff} such that with the magnetic field B measured in the middle of the magnet

$$B\rho = BL_{eff} = \int B(l)dl.$$

eq. 3-6

L_{eff} is in the range where the experiment was carried out practically a constant. Therefore the change in the magnetic rigidity by introducing a target at F2 can be deduced from the scaling factor taking into the account additional corrections for a possible displacement (Δx).

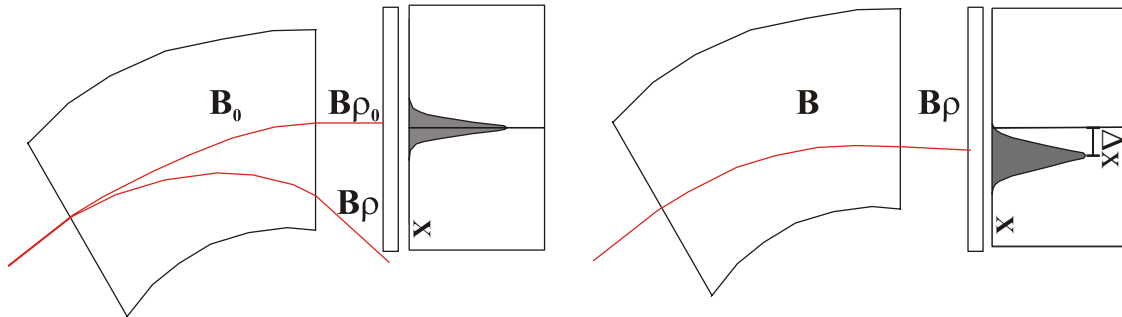


fig. 3-10 Schematic illustration of the energy loss measurement method. Without target (left) the primary beam with a magnetic rigidity $B\rho_0$ is centered in x direction on the MWPC while a beam component with the rigidity $B\rho$ would be out of the acceptance. With a target and after scaling the magnets (right) the beam with the magnetic rigidity $B\rho$ is centered except for a little displacement Δx .

This measurement was done for each beam, target, and energy combination at the third focus F3 and at the final focus F4. So each energy loss measurement consists of two independent measurements one from F2 to F3 and another one from F3 to F4. This does not only increase the accuracy of the measurements but also is very helpful when analyzing the data, as mistakes show up directly in large deviations between the two independent measurements.

The change in magnetic rigidity is thus mainly determined by the scaling factors of the dipole and can be measured in three different ways. First by a Hall probes' voltage, the set values for the currents to the magnets and finally the measured currents. The change in magnetic rigidity is then obtained by applying a 2nd order calibration curve as shown in fig. 3-11.

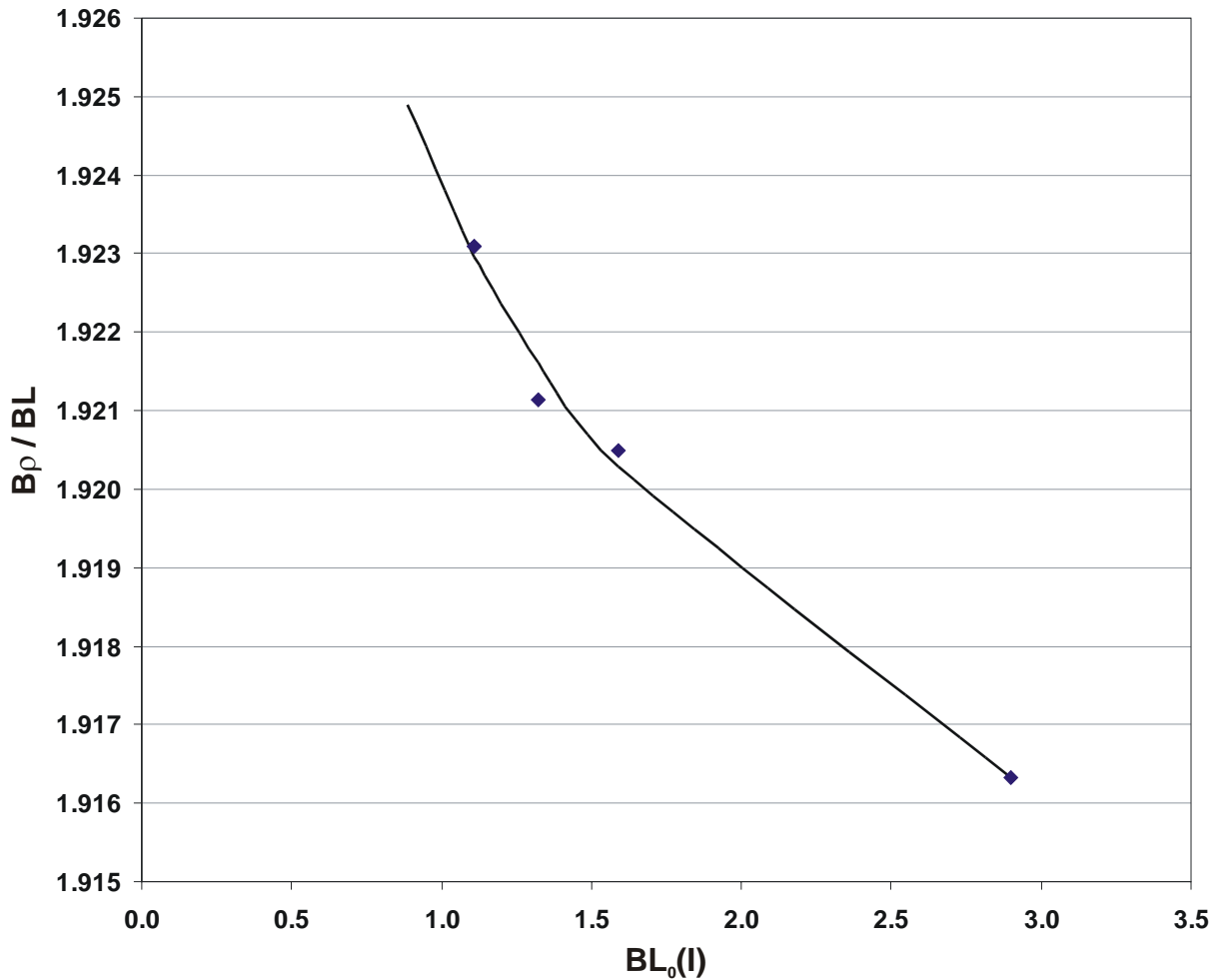


fig. 3-11 Calibration points for $B\rho$ determined via the measured currents versus BL_0 and a 2nd order polynomial fit function.

From the function for the two measured currents

$$B\rho = c_0 + c_1 BL + c_2 (BL)^2,$$

eq. 3-7

and the corresponding function for the Hall probes

$$B\rho = c_0 + c_1 B + c_2 B^2,$$

eq. 3-8

one obtains three sets of parameters c_0 , c_1 and c_2 for the measurements without targets. These are then used to normalize the three different measurement methods. The fit itself is a “chi-square” fit. A comparison of the measured energy loss (ΔE) obtained via the three methods is shown in fig. 3-12 for the case of ^{58}Ni with 50 MeV/u incident energy.

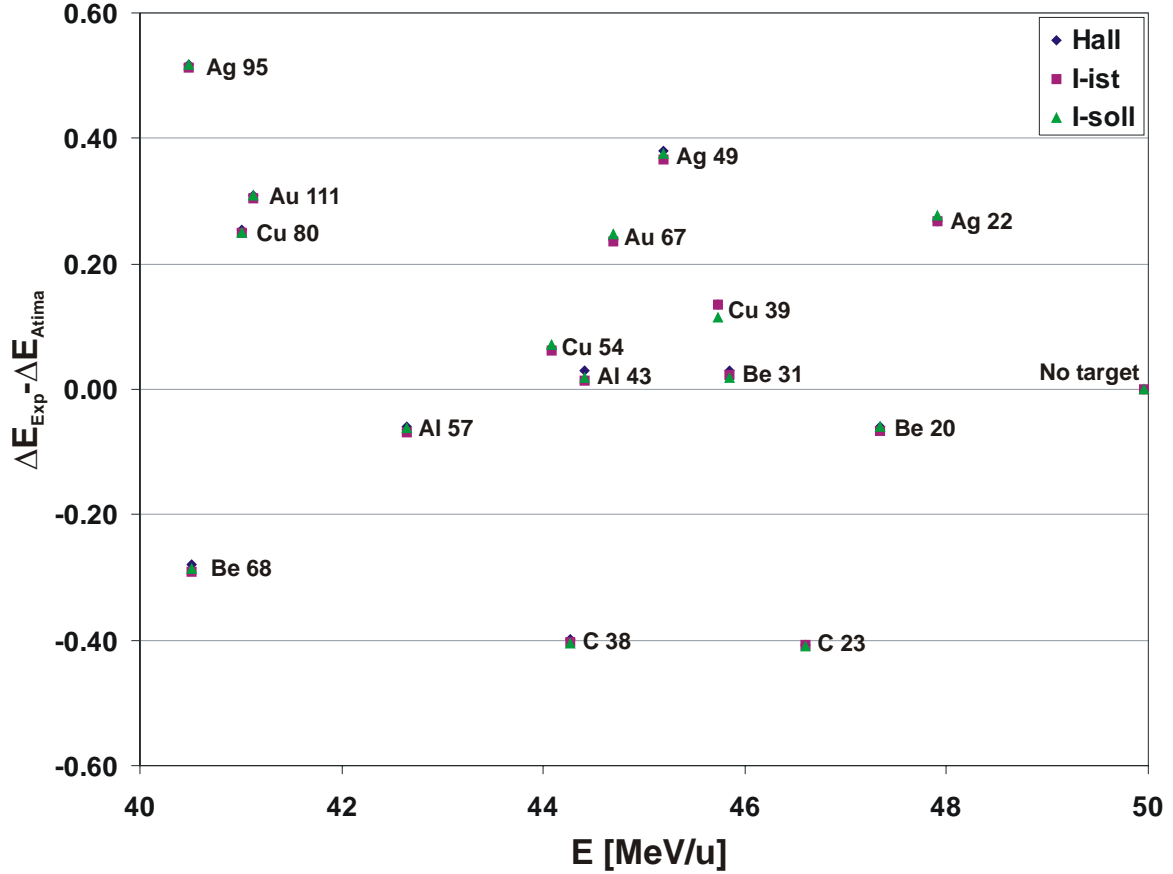


fig. 3-12 The difference between the measured energy loss ΔE_{exp} and the predicted energy loss by the computer code ATIMA ΔE_{ATIMA} as a function of the energy after the targets for the three different methods to determine $B\rho$.

As only the difference between the measurement with and without target enters the calculation an absolute calibration is not needed.

After scaling the magnets the deviation of the beam position is governed by the linear dispersion and can be calculated by

$$\frac{(B\rho) - (B\rho)_0}{(B\rho)_0} = \frac{\Delta x}{(x, \delta)}$$

eq. 3-9

where Δx is the displacement and (x, δ) the linear dispersion coefficient.

The dispersion was measured from the distance of two peaks with neighboring charge states and by shifting one charge state by scaling the magnetic fields by 0.5%, 1% and 1.5 % in positive and negative direction. The values obtained for the dispersions at the optical axis from focal plane F2 to F4 and in between are

$$\begin{aligned} (x, \delta)_{F2-F4} &= 6391 \text{ mm}, \\ (x, \delta)_{F2-F3} &= 2204 \text{ mm}, \\ (x, \delta)_{F3-F4} &= 2850 \text{ mm}. \end{aligned}$$

The momentum of a projectile after passing the target is given by

$$p_i = p_0 \frac{(BL_{eff})_i q_i}{(BL_{eff})_0 q_0} \left(1 + \frac{\Delta x}{(x, \delta)} \right).$$

eq. 3-10

From these measurements the energy loss is calculated by the relativistic energy-momentum relation

$$p_0 = \frac{1}{c} \sqrt{E_0^2 + 2E_0 m_0 c^2}.$$

eq. 3-11

And therefore the energy loss for a target i is given by

$$\Delta E_i = \sqrt{(p_0 c)^2 + (m_0 c^2)^2} - \sqrt{(p_i c)^2 + (m_0 c^2)^2}$$

eq. 3-12

In fig. 3-13 an example is shown for the measured energy loss versus the target thickness. This is again for the case of a ^{58}Ni beam with 50 MeV/u incident energy impinging on Cu targets.

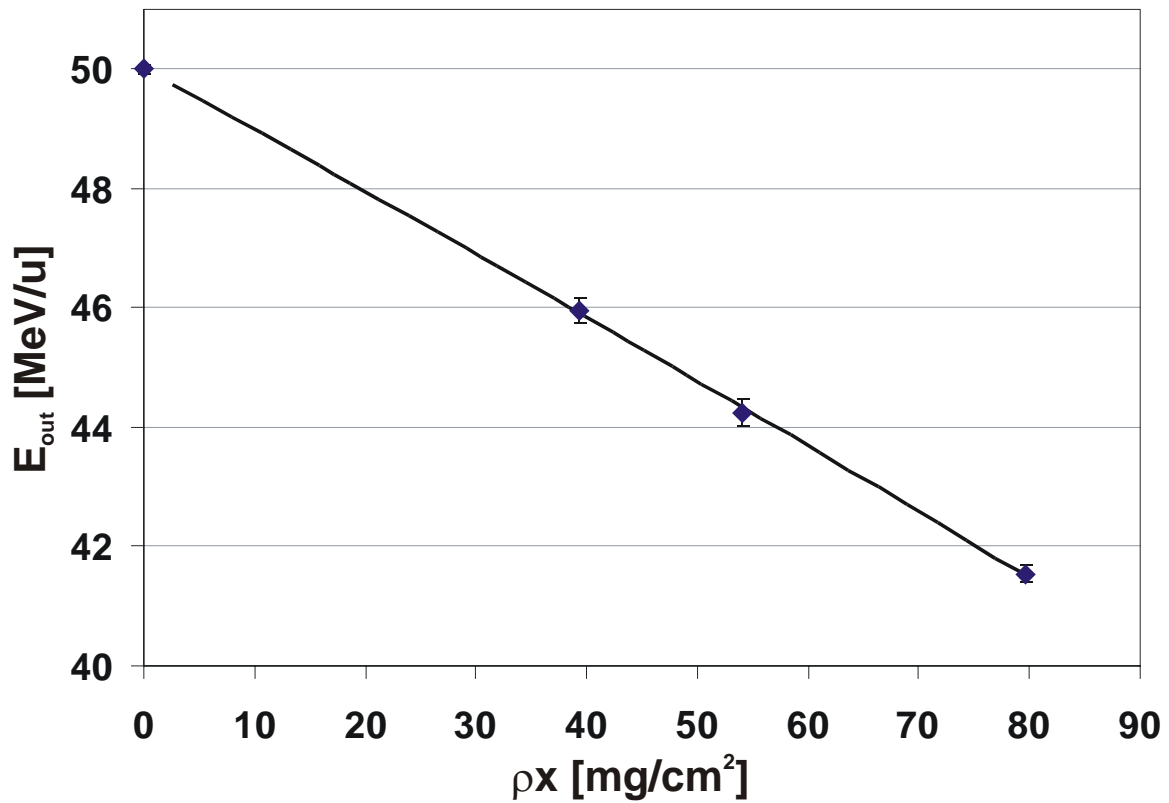


fig. 3-13 Emergent energy of ^{58}Ni ions with 50 MeV/u incident energy as a function of the Cu target thickness. The solid line shows a linear fit to the data points.

3.1.4.3 Stopping power

There are different ways to obtain the stopping power from the set of measured energy-loss data. For each target material the energy-loss was measured for three different thicknesses plus the measurement without target. One way would be to fit a polynomial to the

measured data as the stopping power is energy dependent and thus must contain non-linear terms. This was done for example in [SCH03]. The way chosen here has also been used for analyzing stopping-power measurements at the FRS [WEI00]. The energy dependence of the stopping power is already to a large extent described by theory and can be used as a constant contribution in a fitting function. In this way it is not needed to introduce many free parameters.

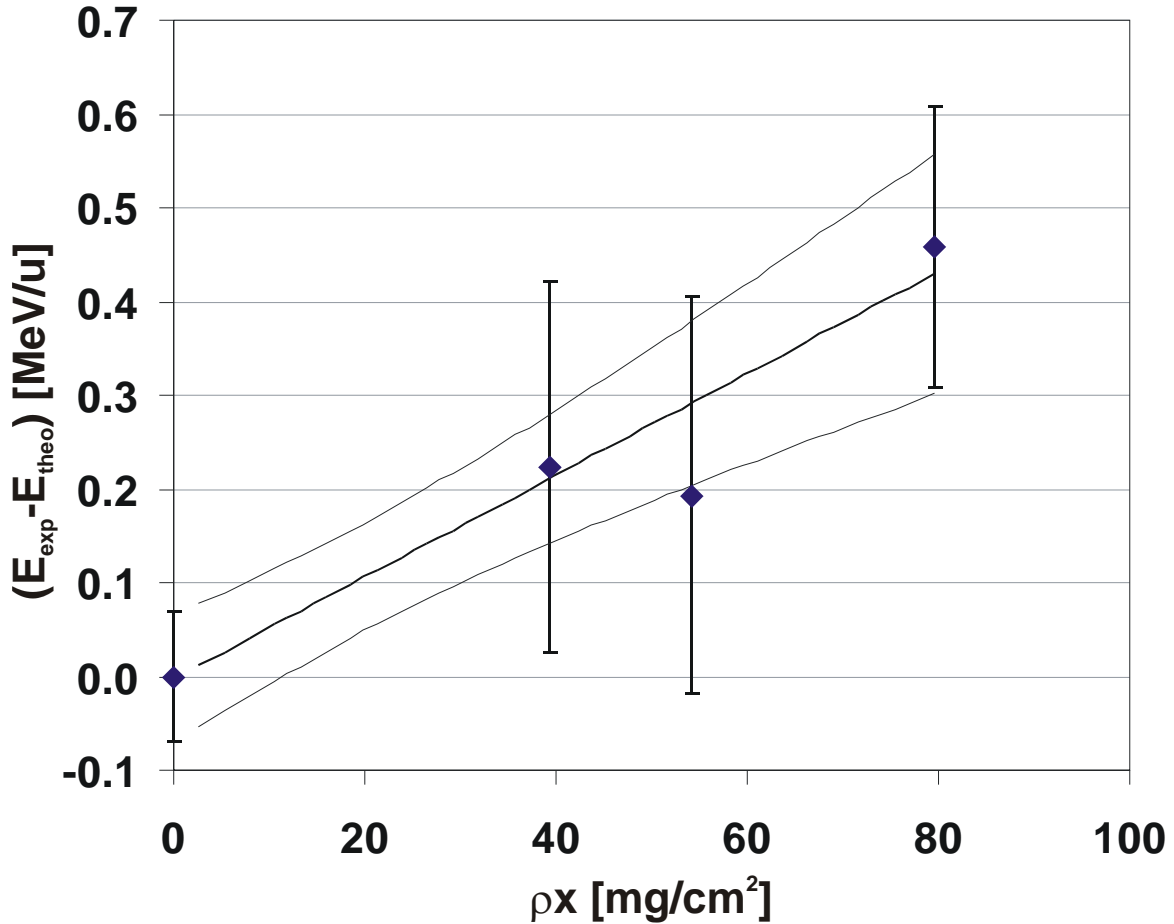


fig. 3-14 The same values for the energy of ^{58}Ni with 50 MeV/u incident energy versus the Cu target thickness as in fig. 3-13. But this time after subtraction of the theoretical prediction by ATIMA. Also included a linear approximation function and the error of this linear approximation.

The measured energy E_{exp} after a target of thickness x can be written as the sum of the initial energy E_0 , the theoretical energy loss ΔE_{theo} and a polynomial $P(x)$ as

$$E_{exp}(x) = E_0 + \Delta E_{theo} + P(x)$$

eq. 3-13

where the theoretical energy loss is negative and given by the integral of the predicted stopping power over the target thickness

$$\Delta E_{theo} = \int_0^x \left(\frac{dE(x')}{dx'} \right)_{theo} dx'$$

eq. 3-14

By differentiating eq. 3-13 one obtains the difference in the stopping power

$$\left(\frac{dE(x)}{dx}\right)_{\text{exp}} = \left(\frac{dE(x)}{dx}\right)_{\text{theo}} + \frac{dP(x)}{dx}.$$

eq. 3-15

3.1.4.4 Energy-loss straggling

The energy-loss straggling was determined via the position distribution at the final focus F4 of the FRS. The ion optical setting was the same achromatic one as described in chapter 3.1.1. Thus the focus was directly on the MWPC41 shown in fig. 3-3. With this setting it is possible to directly obtain the influence of the target on the position distribution $\sigma_x^2(Target)$ on the MWPC from measurements with and without targets as

$$\sigma_{x(Target)}^2 = \sigma_{x,with}^2 - \sigma_{x,without}^2,$$

eq. 3-16

where $\sigma_{x,without}$ is the width of the distribution without target.

This method is shown in fig. 3-15 for the example case of a ^{58}Ni beam with 50 MeV/u on a 79.6 mg/cm² Cu target.

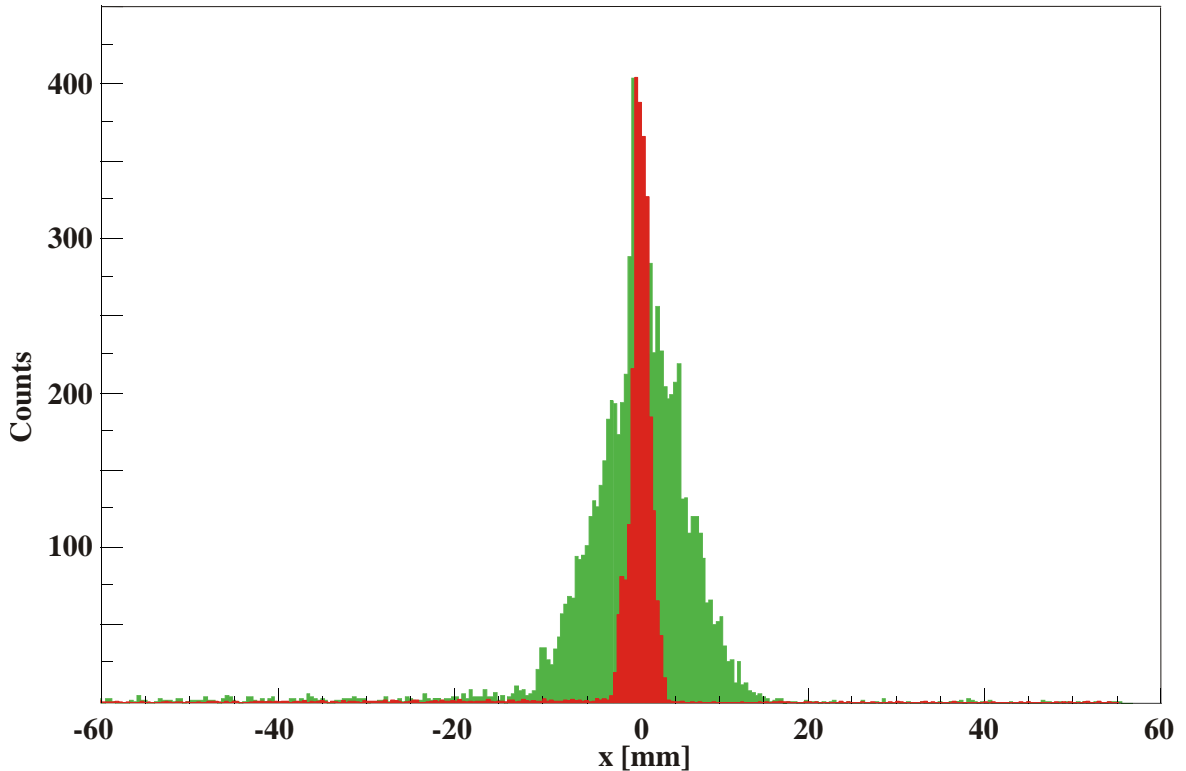


fig. 3-15 Measured width profile of the ^{58}Ni beam at F4 with an initial energy of 50 MeV/u with (green) and without (red) a 76 mg/cm² Cu target at F2.

Due to the collimator mounted before the targets there is a tail to the low energy side coming from projectiles striking the collimator. The background on the high energy side has the same origin but belongs to a different charge state. This background was subtracted as shown in fig. 3-16. To the left and right the background was assumed to be a linear contribution with values c_1 and c_2 at the peak rims. In between the following function $b(x)$

$$b(x) = \frac{(c_1 - c_2)}{1 + e^{\frac{1.81(x-x_0)}{\sigma_x}}} + c_2$$

eq. 3-17

was applied to interpolate.

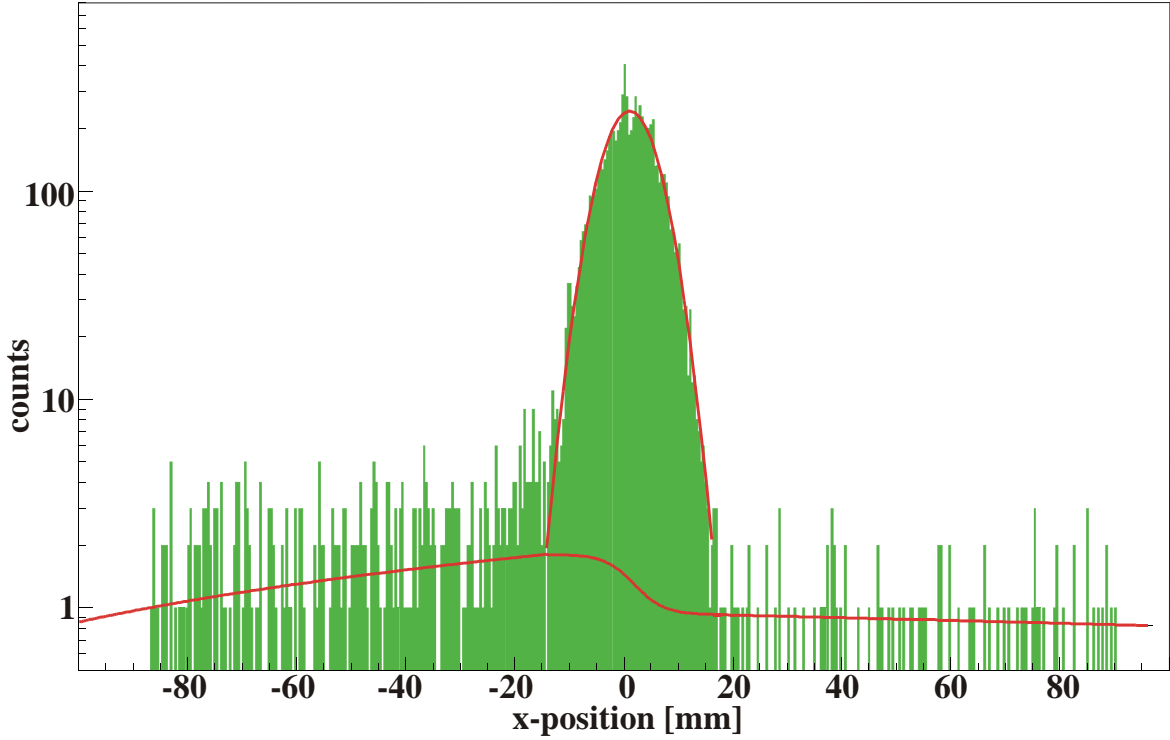


fig. 3-16 Gauss fit of the above case with the Cu target at F2. The background on the left (low energy side) is due to ions striking the collimator. The background to the right has the same origin yet belongs to the next charge state. Both contributions are interpolated due to eq. 3-17 and subtracted for the fit.

After subtracting the background two different methods were used to obtain a width for the peaks. One was to apply a gaussian fit as shown in fig. 3-16. The other method was to count the number of entries per bin in the peak and derive the standard deviation of the distribution around the mean value. The mean value of those two methods was used as the measured distribution. The difference in σ_x by using the two methods is sometimes as big as $\sim 5\%$ and enters as a systematic error in the calculation.

From the obtained position distribution, the measured dispersion and the known charge state it is possible to calculate the relative momentum spread $\Delta p/p$ using a first deconvolution in x-space

$$\frac{\Delta x}{(x/\delta)} = \frac{\Delta p}{p}$$

eq. 3-18

The measured dispersion from F2 to F4 was $(x, \delta) = 6.5 m$.

In principle it is necessary to calculate the momentum of each ion and then derive the resulting momentum spread. But as the variations around the mean value are small, one can treat the energy momentum dependence as linear. Thus one can easily convert the

relative momentum spread using a mean velocity and the corresponding Lorentz factor γ into a relative kinetic energy spread

$$\frac{\Delta E}{E} = \left(1 + \frac{1}{\gamma}\right) \frac{\Delta p}{p}.$$

eq. 3-19

The error introduced assuming this linear dependence is much smaller than the experimental errors and thus negligible.

The results of the energy-straggling measurements for a ^{58}Ni beam at four different initial energies in various target materials are shown in fig. 3-17 to fig. 3-22. The plots show the square of the measured energy straggling $(\sigma_E)^2$ versus the energy loss in the target. For comparison the plots also show the prediction for the energy straggling by the LS-theory implemented in ATIMA [ATIMA].

The contributions to the error bars are coming from the energy-loss measurements, the measured dispersion and from the standard deviation of the two different methods to determine the width of the distribution which is approximately 5%. The last contribution enters the calculation of the error twice as the peak width of the no-target measurement also has this contribution and is always subtracted.

The lighter the target the better is the prediction by the LS-theory in the low energy regime but the energy straggling is overestimated for the 300 *MeV/u* initial beam energy. As the target materials get heavier the predictions get better in the high energy regime but start to underestimate the energy straggling for the low beam energies.

One could start arguing that the charge-exchange straggling might rise the energy straggling especially for the heavy targets where more charge states appear (up to four charge states for Au targets). But the effects seen in the C, Ag and Au target measurements are by far too big to be explained with charge exchange straggling.

In the measurements with the carbon targets this effect is strongest. For the 300 *MeV/u* measurement the prediction and the measurement agree very well within the error bars, but for the lower energies the deviations to the theory are huge. One could firstly expect a surface effect but then the deviations should become smaller with increasing target thickness. Yet one can clearly see that the opposite is the case, the deviations are increasing with the target thickness. Thus this must be related to a granularity effect over the whole target volume.

To prove that this is the reason for the deviation one can check the density of each target as the weight, the area and the thickness were measured as described in chapter 3.1.3. The listed density of carbon ^{12}C is 2.26 *g/cm³* at 300 K [ECC95]. The table below shows the calculated densities for the carbon targets as they were used for the experiment.

tab. 3-1 Calculated density of the used carbon targets using the measured values for the thickness, area and weight by the target laboratory.

Thickness [mm]	Thickness [mg/cm ²]	Area [cm ²]	Weight [mg]	Density [g/cm ³]
0.085	14.7	5.83	89.77	1.81
0.134	23.0	5.50	126.5	1.71
0.42	77.9	5.35	417.1	1.86
0.8	150.7	3.14	473.4	1.88
2.54	472.6	3.13	1480.4	1.86
3.5	769.4	3.14	2416.8	2.20
4.24	925.3	3.13	2893.3	2.18

From this table one can see that the densities of all thin carbon foils are off by about 20% from the listed value. The two thick foils were stacked and are responsible for the data point at 300 *MeV/u* which is within the error bars right on the theory.

However, the deviations seen in the energy straggling are by far larger, up to a factor 10, than this. Yet one has to keep in mind that the deviation from the density does not say anything about the granularity itself, only that there is one. In principle in an extreme case it could be just one bubble inside the target lowering the density.

Unfortunately for the other target materials, especially the thin Au and Ag foils showing the same type of deviation, the weight was not determined by the target laboratory. For this reason it was not possible to check the density like for the carbon foils where it became clear that the reason for the deviation is simply the quality of the targets. Suspicion arises that this might as well be the reason for the large deviations measured in these cases.

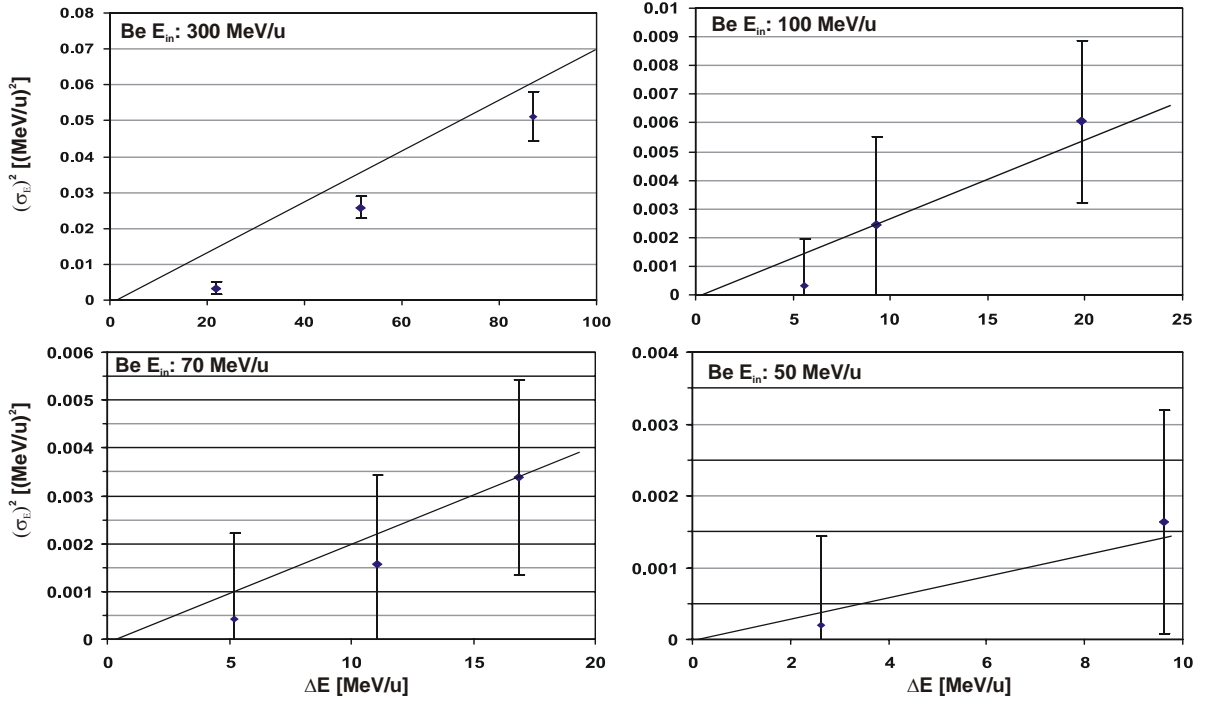


fig. 3-17 Variance of the energy straggling σ of Ni ions in various beryllium targets versus the energy loss in these targets for four different initial beam energies. The solid lines show the prediction by ATIMA.

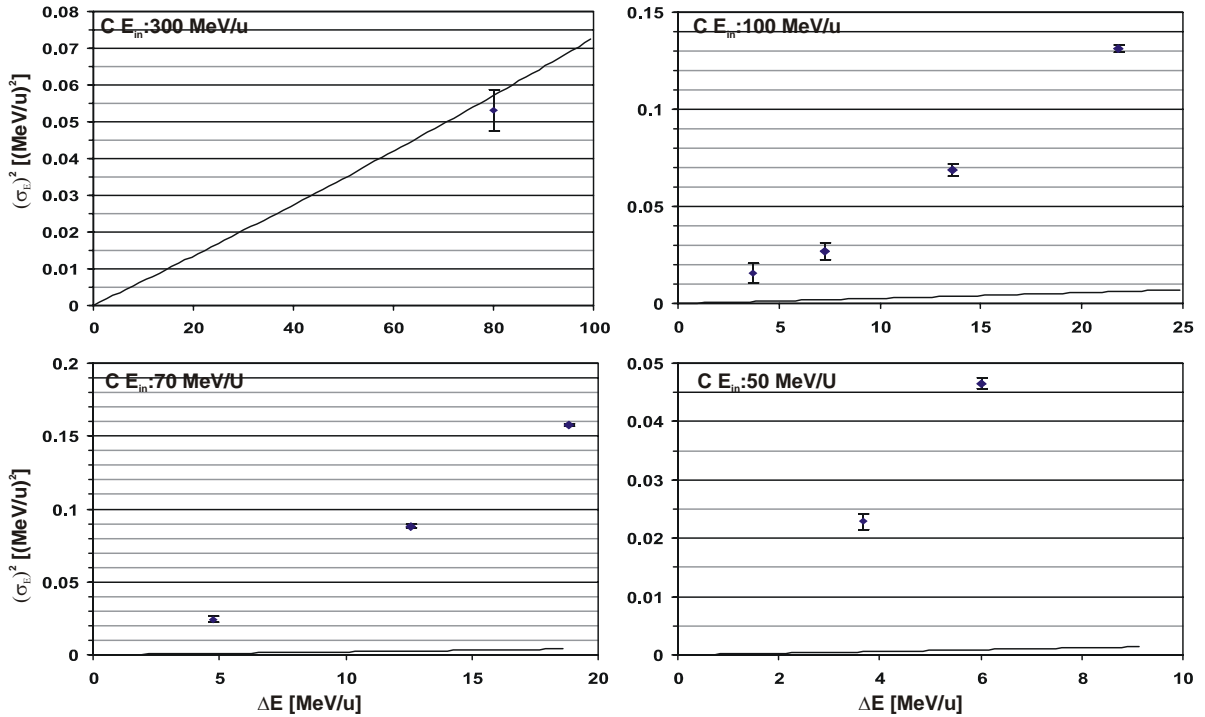


fig. 3-18 Variance of the energy straggling σ of Ni ions in various carbon targets versus the energy loss in these targets for four different initial beam energies. The solid lines show the prediction by ATIMA.

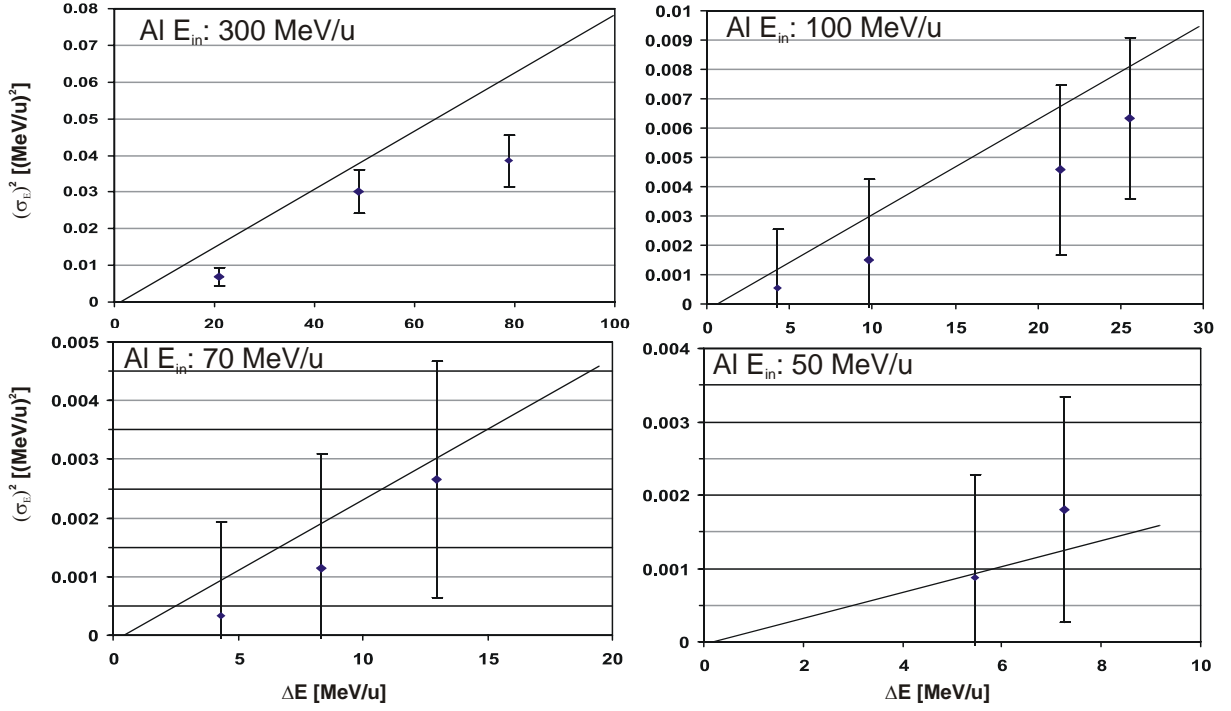


fig. 3-19 Variance of the energy straggling σ of Ni ions in various aluminum targets versus the energy loss in these targets for four different initial beam energies. The solid lines show the prediction by ATIMA.

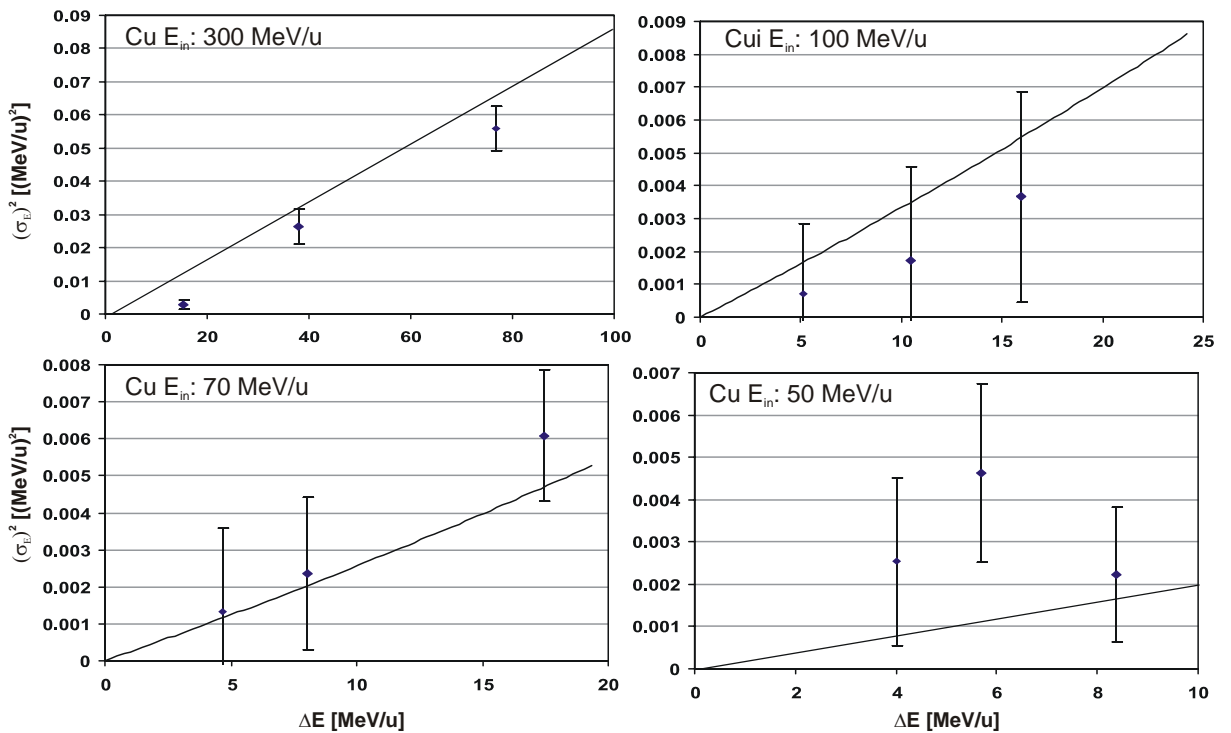


fig. 3-20 Variance of the energy straggling σ of Ni ions in various copper targets versus the energy loss in these targets for four different initial beam energies. The solid lines show the prediction by ATIMA.

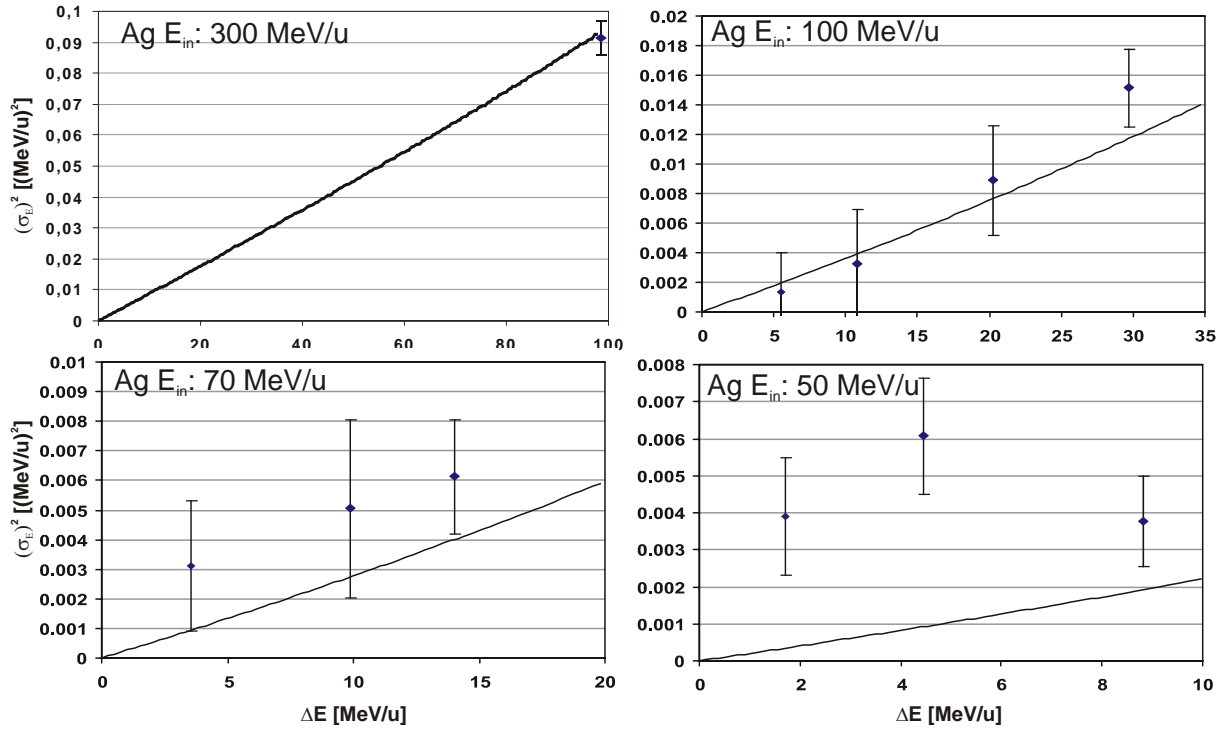


fig. 3-21 Variance of the energy straggling σ of Ni ions in various silver targets versus the energy loss in these targets for four different initial beam energies. The solid lines show the prediction by ATIMA.

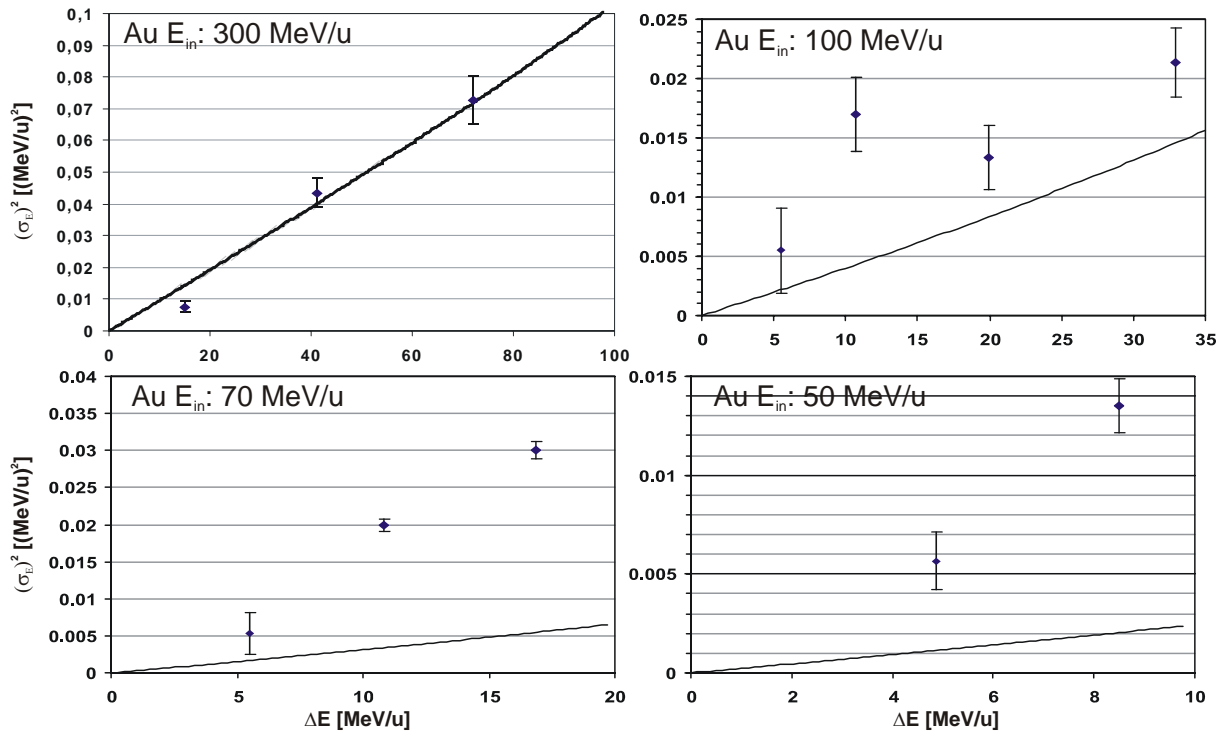


fig. 3-22 Variance of the energy straggling σ of Ni ions in various gold targets versus the energy loss in these targets for four different initial beam energies. The solid lines show the prediction by ATIMA.

These drastic deviations together with the fact that the measurement was done using only one detector and the problems with the targets does not allow to draw conclusions or judge the quality of a theory based on the obtained results.

For future energy straggling measurements one first of all really has to take care about the target materials. The thickness, the size and the weight have to be directly measured and each target should be labeled and retraceable to its manufacturer to avoid these confusions in the future.

In order to do a more precise measurement two detectors have to be used in order to be able to trace every particle to allow for determining the peak width at the waist of the beam and not only rely on ion-optical calculations that the focus in the used optical setting is on the detector, since the position of the beam waist changes with inserting different target materials and varying thicknesses.

3.2 Range focusing of relativistic ^{56}Ni and ^{54}Co ions

In-flight separation of projectile fragments is a fast ($< \mu\text{s}$), chemically independent and isotopic clean method of giving access to all nuclei up to uranium. The projectile fragments have a energy distribution caused by the kinematics of the nuclear reaction and the energy losses in the production target.

In order to do high precision experiments, such as laser spectroscopy, γ -spectroscopy and atom or ion trap experiments on the reaction products it is necessary to slow down or even stop them in thin layers of matter such as a gas cell [SAV03]. The resulting range straggling, σ_R , of ions stopped in matter is dominated by the incident momentum distribution σ_p of the projectiles. The upper limit of the momentum distribution is given by the acceptance of the spectrometer. For the FRS this limit is on the order of $\sigma_p/p=1\%$ [GEI92].

A new approach pioneered at the FRS has been developed. A specially shaped monoenergetic degrader [GEI89] at the final dispersive focal plane has been used to reduce the momentum spread effectively. This will increase the efficiency of capture by devices such as gas cells. The results of first experiments at the FRS with such a degrader system on relativistic ^{56}Ni and ^{54}Co fragments are presented in this work.

In order to obtain a narrow range distribution in thin layers of matter it is necessary to apply a significant reduction in momentum spread. This is demonstrated in fig. 3-23 for a ^{56}Ni fragment beam impinging into a gas cell filled with helium at a pressure of 1 atmosphere. The calculated range straggling of a ^{56}Ni beam is plotted versus the energy for two different initial momentum distributions and compared to the stopping volume of a gas cell developed at Argonne [SAV03].

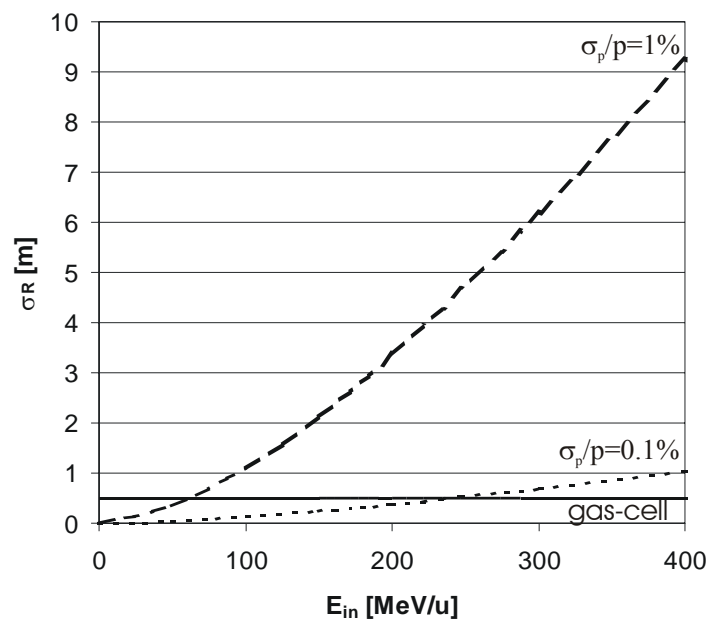


fig. 3-23 Calculated range straggling σ_R of ^{56}Ni ions in helium for 1% initial momentum spread (dashed line) and 0.1% initial momentum spread (dashed dotted line) versus the beam energy E_{in} using the computer code MOCADI [IWA97]. The straight solid line corresponds to a stopping volume of a 1.25 m long gas cell filled with helium at 400 mbar corresponding to 8.9 mg/cm^2 .

This cell as with an effective length of 1.25 m is projected to run at gas pressures of 400 mbar. For Helium this corresponds to 8.9 mg/cm^2 of stopping thickness. For the GSI FRS ion catcher the cell will be extended to 1.4 m corresponding to 10 mg/cm^2 . Besides the dependence on energy the range straggling of a stopped beam is clearly dominated by the initial momentum distribution of the projectiles.

The optimum operation domain for the FRS is clearly above 100 MeV/u for ions heavier than Argon as seen in fig. 3-24 where the yield of bare ions which undergo no nuclear losses is plotted versus the energy of the projectiles. For higher energies thicker production targets can be used and the fragments are more forward focused. Therefore the yield increases with energy. Yet at higher energies the thicker target as well as the thicker degrader lead to increased absorption by nuclear losses and increased energy straggling from the material. All effects together yield in a optimum energy for the production and stopping of each nuclei. At these high energies fig. 3-23 signifies clearly that in order to minimize the range straggling the initial momentum spread has to be reduced.

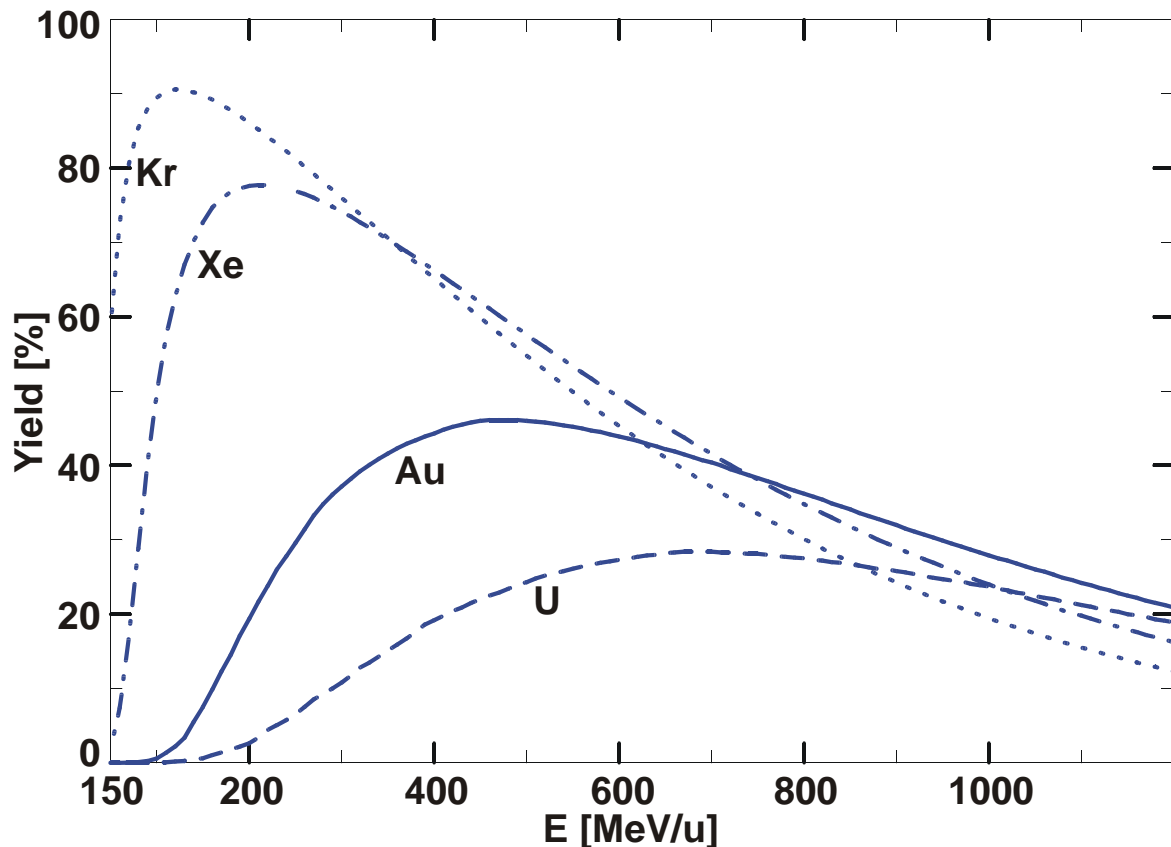


fig. 3-24 Calculated yield of bare ions after the intermediate aluminium degrader which undergo no nuclear reactions during the stopping process up to the final focus as a function of their exit energy. Transmission through the second stage of the FRS is not included in the calculation.

To reduce the momentum spread one can use the fact that a magnetic dipole stage spatially separates the projectiles according to their momentum. Placing a monoenergetic degrader at the dispersive focal plane [GEI89] after the magnetic dipole as shown in fig. 3-25 can reduce the momentum spread. By adjusting the degrader angle α according to the dispersion such that the difference in energy loss compensates for the different momentum it is possible to compensate energy straggling effects from in front of this magnetic dipole.

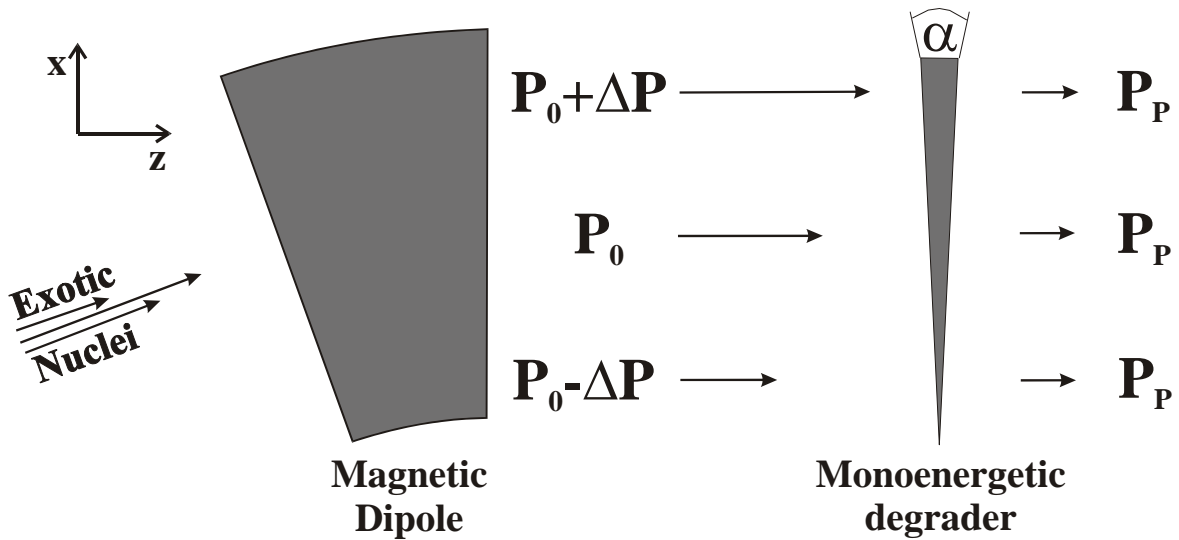


fig. 3-25 Illustration of the range focusing principle. The projectiles dispersed in momentum enter a magnetic dipole stage which spatially separates the projectiles in x-direction according to their momentum difference δp . The monoenergetic degrader [GEI89] compensates the momentum distribution by adjusting the thickness via the degrader angle α and therefore the energy loss according to the dispersion of the magnetic dipole.

Energy straggling occurring after the magnetic dipole can not be bunched. These unavoidable contributions are the energy loss straggling in material after the dispersive stage. These are the degrader system itself, vacuum windows and the detectors. Thus it is necessary to use materials and mechanical alignments with a very high precision in thickness uniformity.

3.2.1 The degrader system

The prototype degrader system developed and used for range focusing consists of a degrader to adjust the total energy loss by variation of the total thickness d and a degrader to vary the angle α as shown in fig. 3-27.

The overall homogeneous, high-precision degrader consists of two wedge shaped parts made of a special glass material, Suprasil 2 (SiO_2). The wedges are driven by a stepper motor drive which allows for a quasi continuous thickness variation d in z-direction by equal and opposite displacement of the two wedges along the y-axis. The thickness in y and x-direction is uniform. The minimum thickness is $d_{min} = 259.72 \text{ mg/cm}^2$ and the maximum thickness is $d_{max} = 3191.45 \text{ mg/cm}^2$. The minimum thickness variation possible is given by $\Delta d_{min} = 1 \text{ step} = 0.076196 \text{ mg/cm}^2$. This degrader is from here forth called the homogenous degrader.

The monoenergetic degrader is made from aluminum. It consist of two widdershins rotatable discs with a maximum slope of $\alpha = 18.43 \text{ mrad}$ while the center thickness stays constant at 837 mg/cm^2 . The thickness of the discs varies linearly along the x-axis as a function of the disc rotation angle β being always equal and opposite for each disc. Along the y-axis the thickness stays uniform. The discs are mounted on an arm to move them in and out of the beam. The disc angle as a function of rotation angle β is given by

$$\alpha = 18.4 \text{ mrad} \cdot \cos\left(\frac{\pi}{2} - \beta + 15^\circ\right),$$

eq. 3-20

where α is the degrader angle in mrad, 18.4 mrad is the maximum slope of the two discs and β is the rotation angle. Due to a misalignment by the manufacturer of the discs a correction had to be applied afterwards to get the actual disc angle. Each disc had been misaligned by $\beta=15^\circ$ during assembling. To avoid any sideways movement and tilting the two discs are mounted between four wheels each to hold them in position as shown in fig. 3-26.

The optimum angle for energy focusing can be calculated for a very thin degrader approximation according to

$$\tan \alpha = \frac{\gamma m v^2}{D \cdot \frac{dE}{dx}},$$

eq. 3-21

where γ is the Lorenz factor, m and v are the mass and velocity of the projectile respectively, D is the dispersion coefficient and dE/dx is the stopping power in the degrader material. Yet this formula is only used for an estimation. To get a more reliable result for the optimum degrader angle one can use MOCADI and calculate the range straggling for different angles to find the minimum as it was done for this experiment.

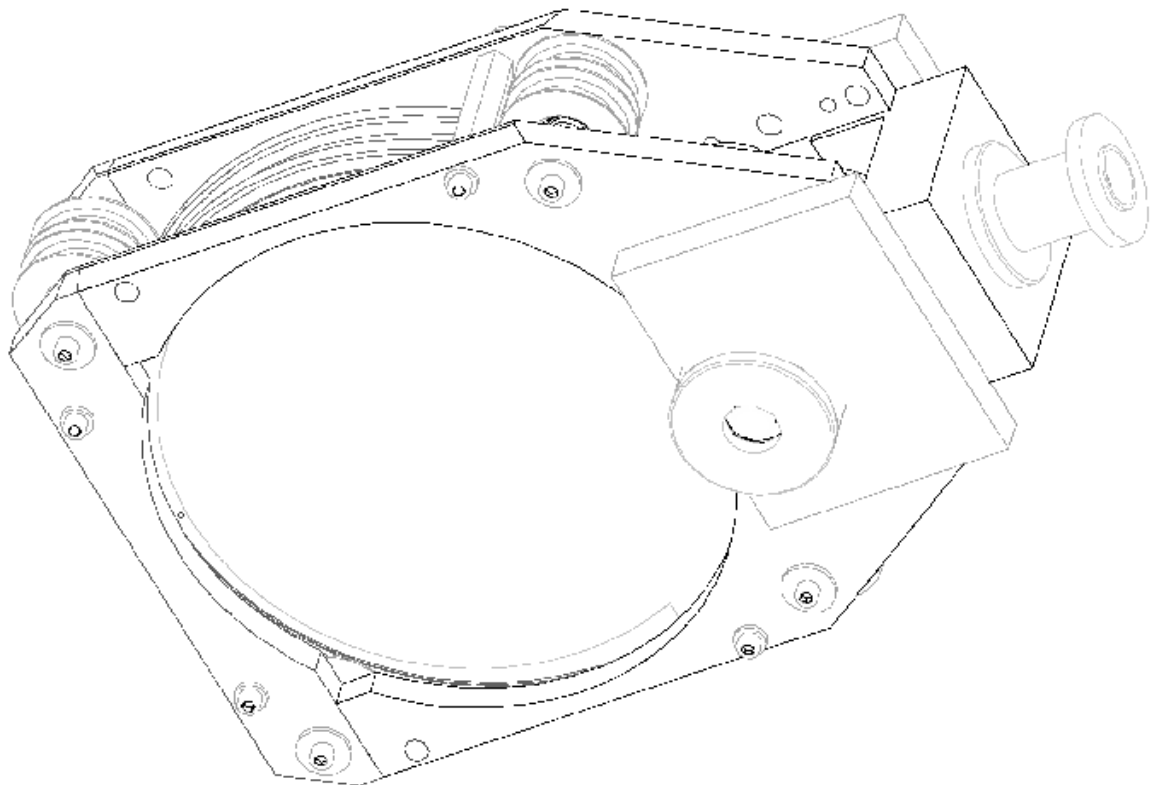


fig. 3-26 Three dimensional technical drawing of the monoenergetic degrader. The two widdershins rotatable discs are held in place by four wheels each to avoid tilting of the discs. Around the discs there are teeth in order to drive them with cock wheels via a stepper motor drive.

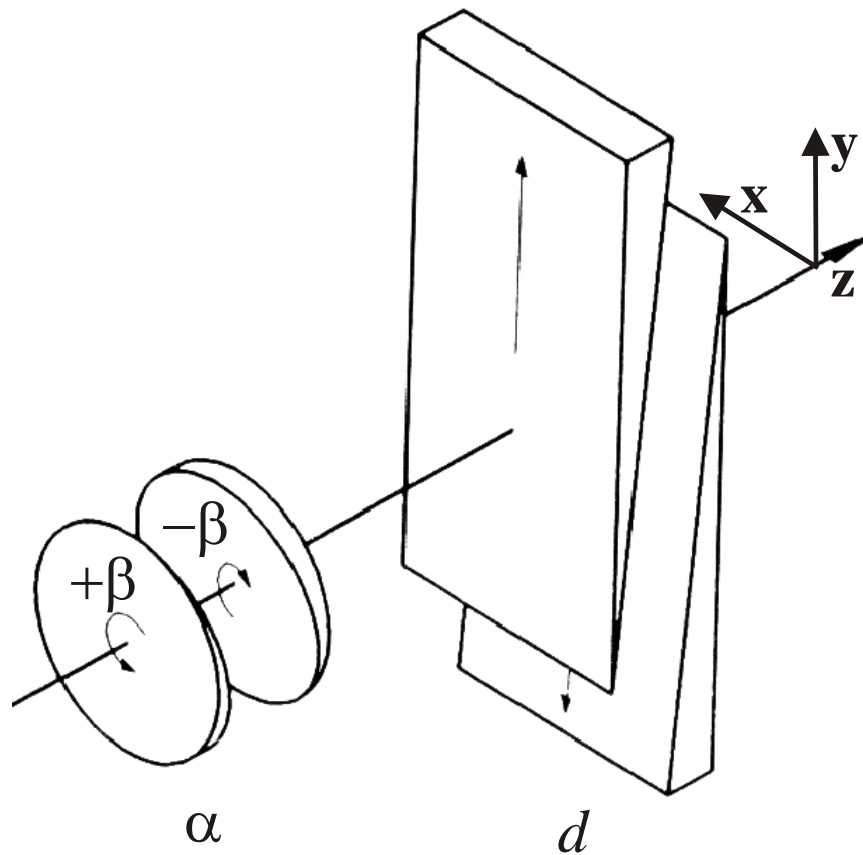


fig. 3-27 The prototype degrader system as used for the experiment (top) and schematically (bottom). This two stage degrader system consists of a degrader to vary the angle α by rotating two wedge shaped discs by the angle β , and a degrader to adjust the total thickness d .

3.2.2 The magnetic spectrometer FRS

Since the FRS in the standard optical mode is an achromatic ion optical device [GEI92] and at present there is no space for a separate energy buncher stage, hence different ion optical schemes had to be developed and tested. There are different ways to operate the FRS in a dispersive focusing mode as pointed out in the PhD thesis by Vladimir Chichkine [CHI03].

For the range focusing experiment fig. 3-28 the first half of the FRS from TA to the second focus S2 was operated in a low dispersion beam transport mode centering 461.45 MeV/u $^{58}\text{Ni}^{28+}$ on the 2.935 g/cm^2 aluminum production target after a collimator at S2. The second half of the FRS was operated in dispersive mode with a momentum dispersion of 6.84 cm/\% , centering $^{56}\text{Ni}^{28+}$ fragments with 360 MeV/u at S4. This optics setting does not lead to a isotopically clean beam but to a so called ‘cocktail’ beam, selecting $A/Z=2$ fragments to reach F4 as shown in fig. 3-29. The final focal plane for ^{56}Ni in this optics setting is on the monoenergetic degrader as shown in fig. 3-3.

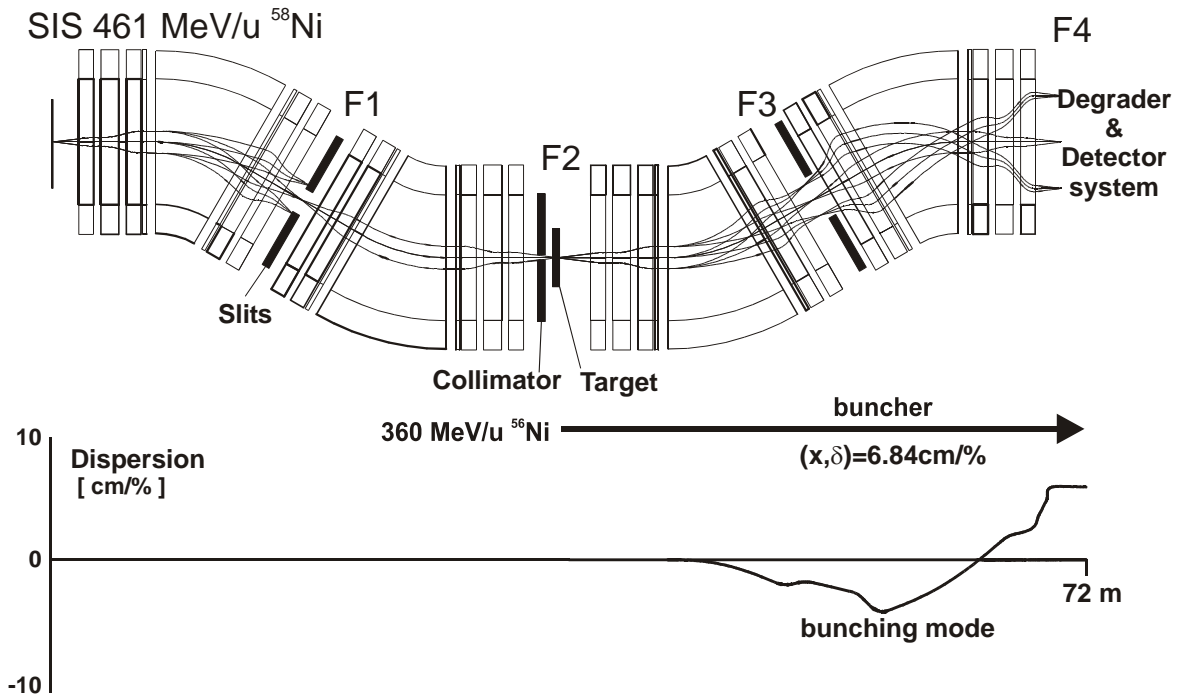


fig. 3-28 Ion optical setting (upper) and dispersion plot (lower) used for the range focusing experiment on ^{54}Co and ^{56}Ni . The dispersion function shows the mode of the FRS and reached a value of 6.84 cm/\% from F2 to F4.

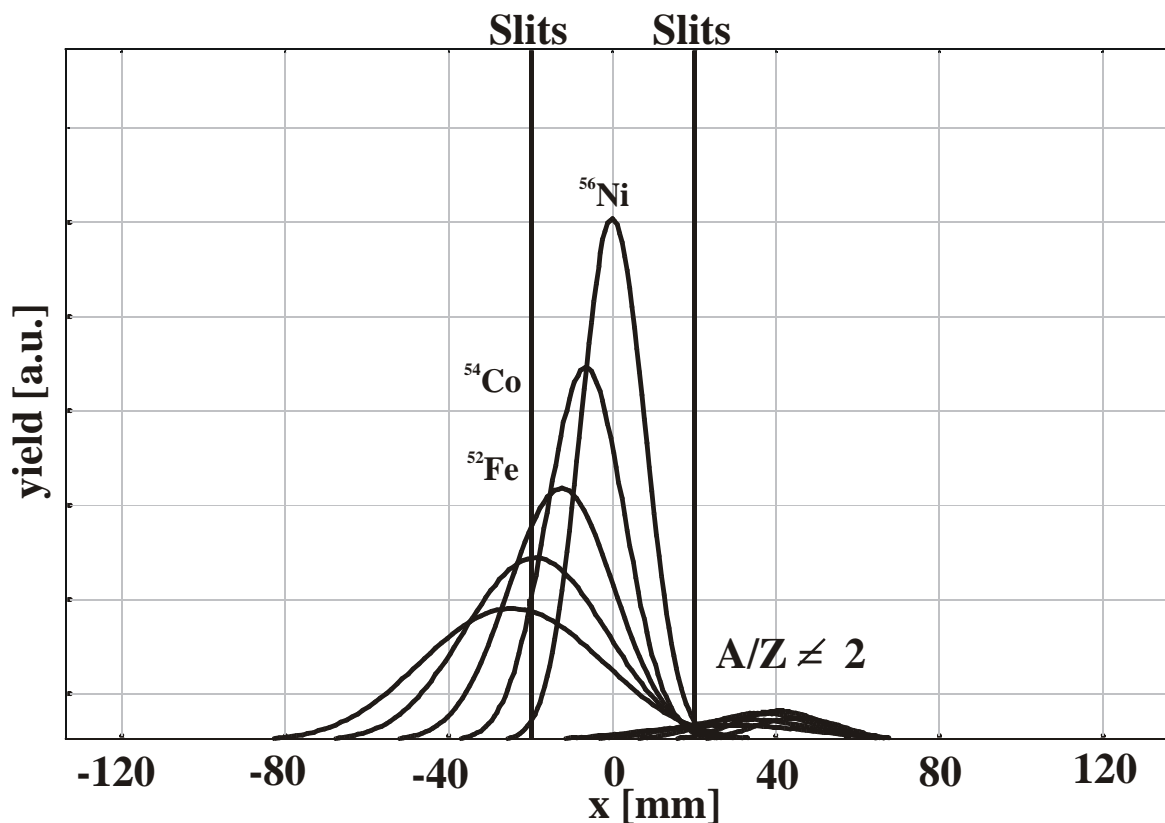


fig. 3-29 Fragments yield at F3 versus the x-position with ^{56}Ni centered according to LISE [LIS03] simulation. The vertical lines indicate the slit position to cut off none $A/Z=2$ fragments. The reason for the lighter $A/Z=2$ fragments not being centered is due to the different energy loss in the target.

3.2.3 Measurement

A schematic view of the experimental setup for the range focusing of ^{56}Ni and ^{54}Co is shown in fig. 3-30, a more precise picture of the detector setup fig. 3-3 was already shown.

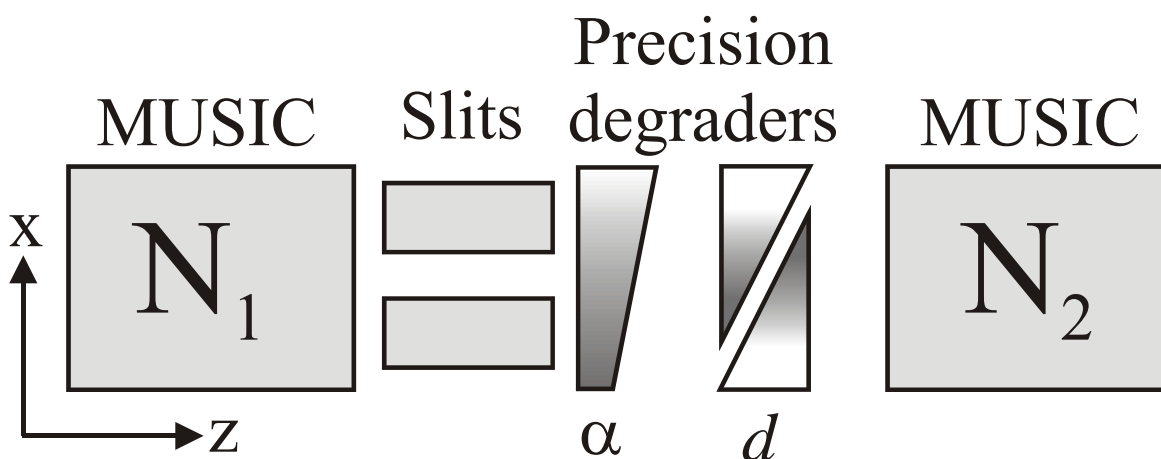


fig. 3-30 Schematic view of the experimental setup for the range focusing measurements. Two Multi Sampling Ionization Chambers (MUSIC) were used for particle identification and counting their number N_1 and N_2 respectively. In between the MUSIC detectors the two stage degrader system to vary the angle α and the total thickness d is located as well as the slits to select the $A/Z=2$ fragments

As ^{56}Ni was centered and focused on the monoenergetic degrader for this experiment. The lighter $A/Z=2$ fragments are off center and therefore arrive with decreased yields as shown in fig. 3-31. All other fragments are cut off by the slits just in between the two detectors.

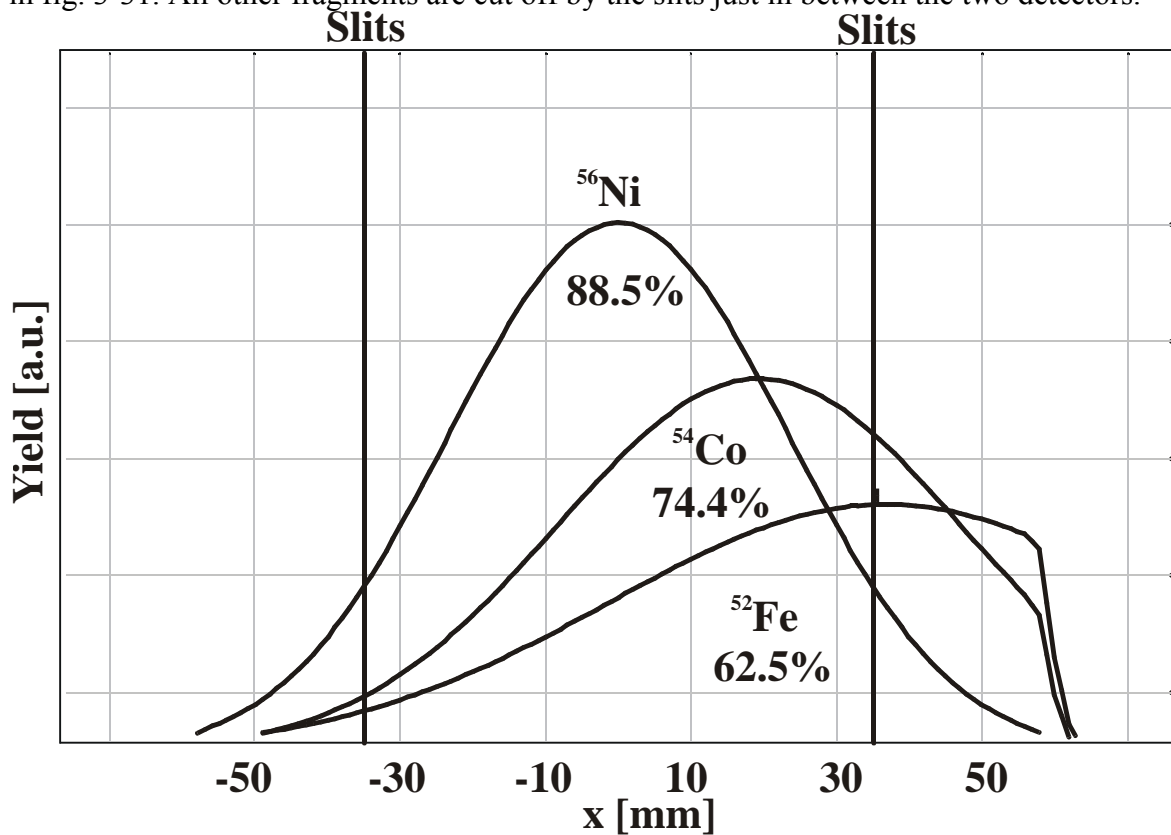


fig. 3-31 Yield of $A/Z=2$ fragments at F4 versus the x-position. 88.5% of ^{56}Ni are passing the slits, while for the not centered ones the losses are larger.

The detectors used for identification and counting of the particles are MUSICS [PFÜ94]. Ionisation chambers of 0.6 m length filled with P10 (90% Ar, 10% Methane) gas at 1 bar with four separate anodes to detect the particle tracks. Since the number of generated electrons is roughly proportional to the square of the charge of the penetrating particle, the output voltage of the preamplifier is a measure for the atomic number of this particle. A more detailed description of the MUSIC detector was given in chapter 3.1.2.

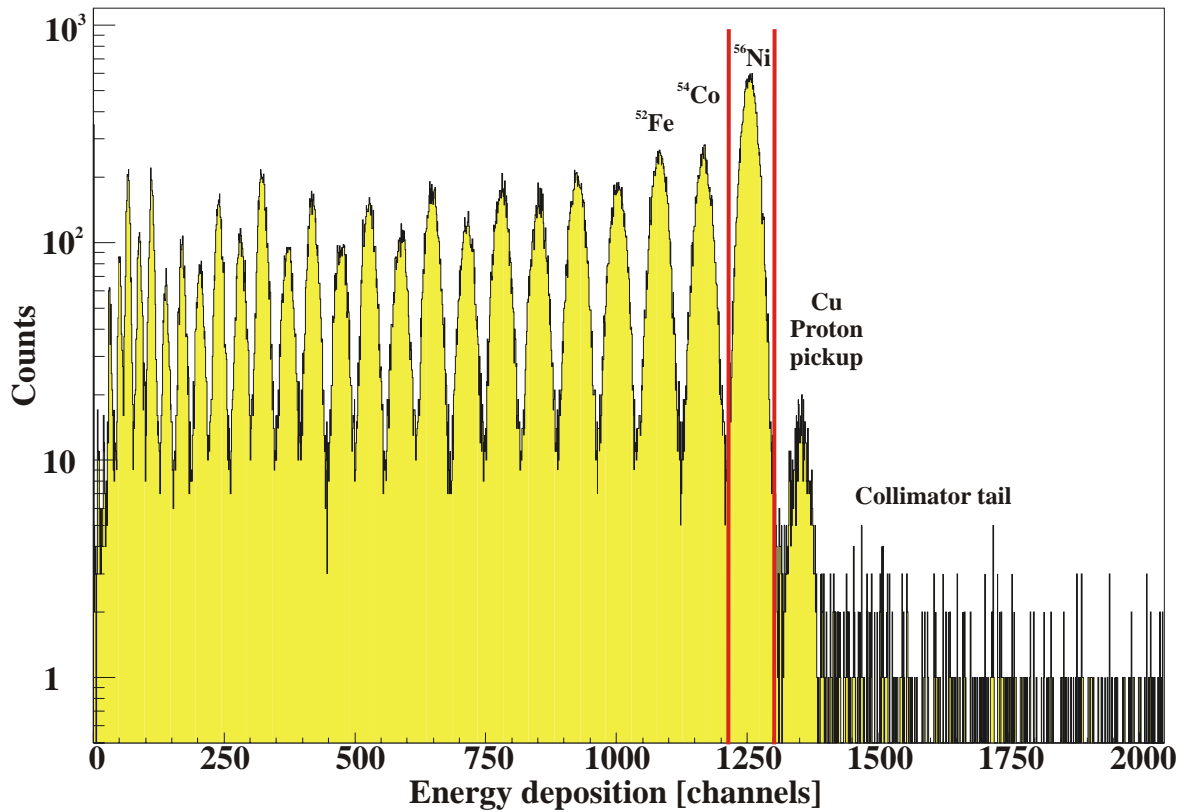


fig. 3-32 Counts in the 1st music detector as a function of energy deposition. A gate is set to select a certain species. In this case ^{56}Ni was selected.

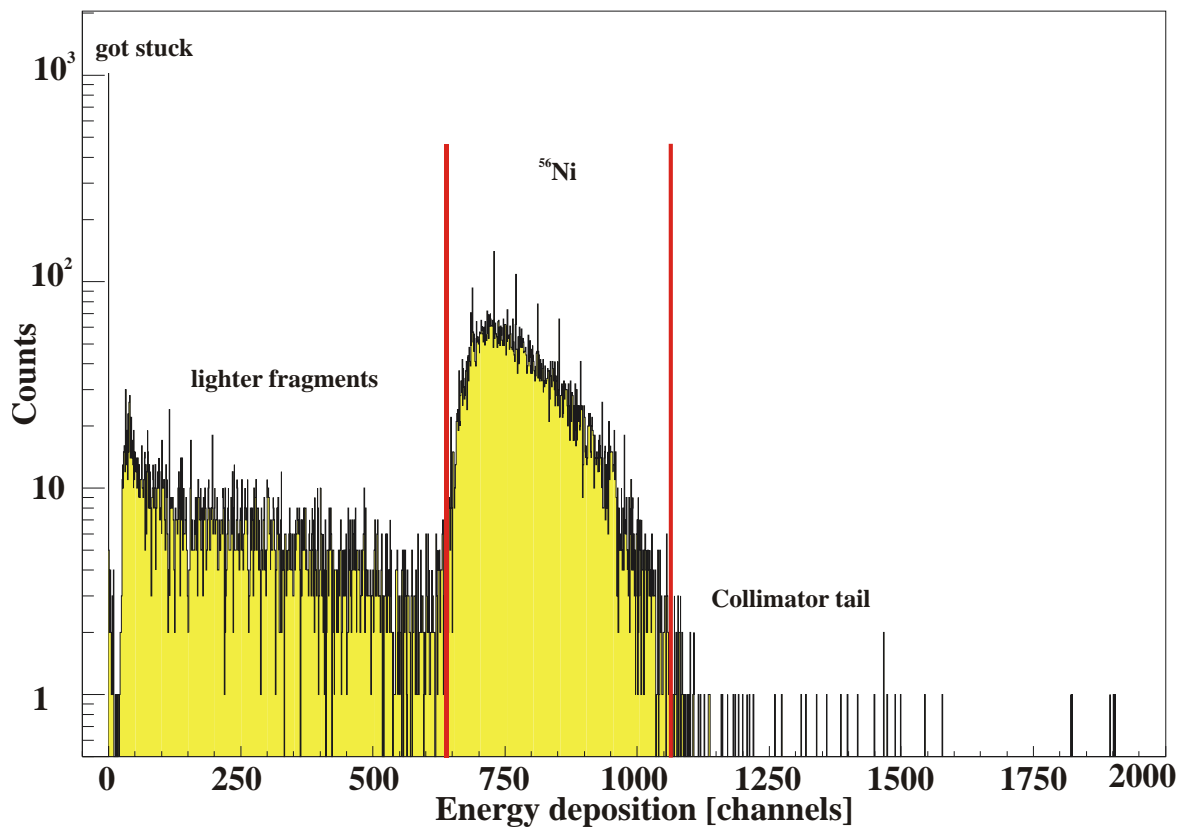


fig. 3-33 Counts in the 2nd music detector as a function of energy deposition only counting those ions which were previously identified and gated in the 1st music.

In the first MUSIC the fragments are identified as shown in the upper plot of fig. 3-32. A gate is set to only count those fragments in the second MUSIC which were of the selected

species identified in the first. Fragments which are lost in between the two MUSICS contribute as a zero count in the second. The large background in the second MUSIC is due to the nuclear reactions. A quite large fraction of the fragments undergo nuclear reactions in the degrader material and other layers of matter like the detectors and windows. For the ^{56}Ni fragments these losses are on the order of 30% according to calculations using the Kox formula [KOX87].

All matter together except for the homogeneous degrader had a thickness of 1144 mg/cm^2 . The other contribution to the background was coming from projectiles striking the collimator and the slits. At the slits about 12% of the fragments are cut off which is the reason for the large contribution to the peak at zero in the second MUSIC. Due to the calculations the losses before the second MUSIC add up to about 42% of the fragments identified in the first MUSIC.

Plotting the ratio of ^{56}Ni fragments identified in the first MUSIC, N_1 , divided by the fragments reaching the second MUSIC, N_2 , versus the degrader thickness Δx one obtains a number distance curve NDC for each of the read out anodes as shown in fig. 3-34. The losses due to nuclear reactions and cut off are approximately 45% and thus agree very well with the estimates.

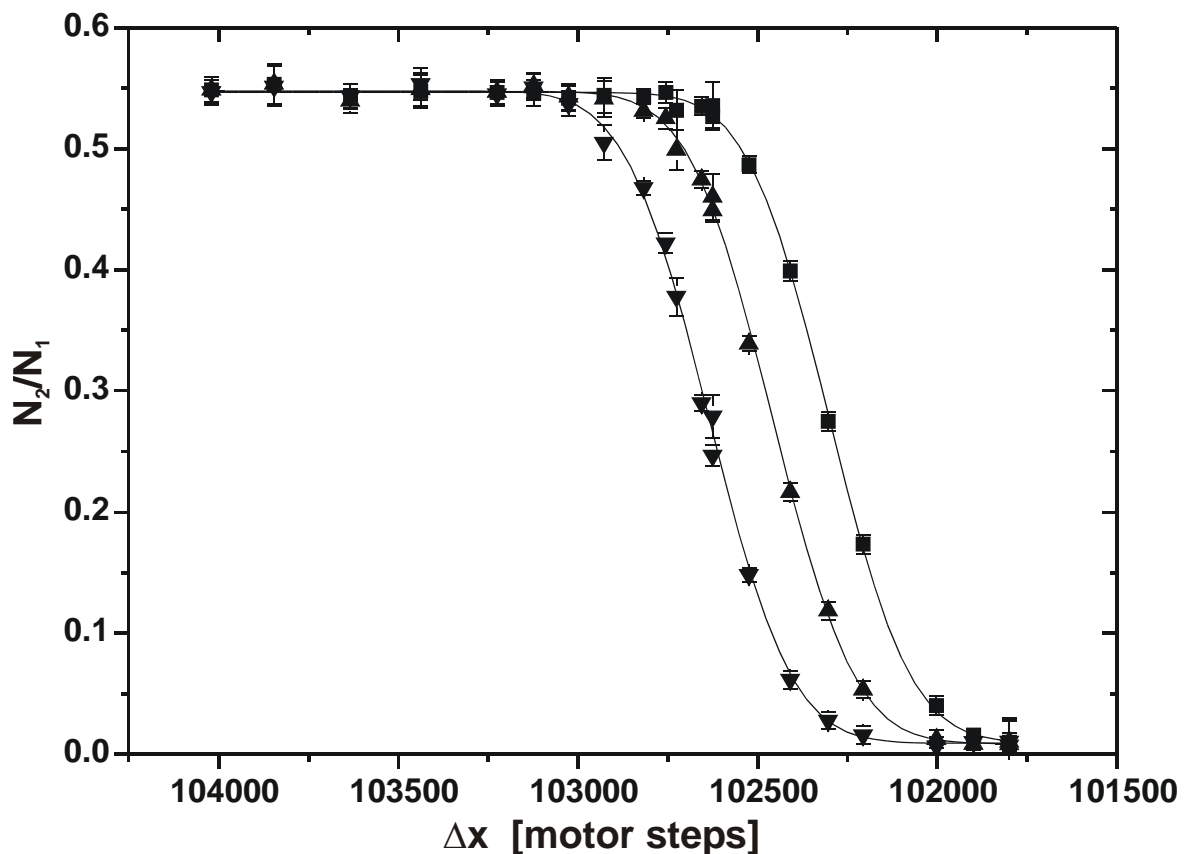


fig. 3-34 NDC obtained using three Anodes of the 2nd music varying the degrader thickness Δx for one fixed degrader angle α . The drawn lines are fits with the error function to the data points.

These NDCs are fitted using an approximated expression for the error function.

$$\text{erf}(x) = \frac{2}{\sqrt{\pi}} \int_0^x e^{-u^2} du$$

eq. 3-22

A Taylor expansion of eq. 3-22 leads to an expression of the form

$$\begin{aligned} \operatorname{erf}(x) &= \frac{2}{\sqrt{\pi}} \left(x - \frac{x^3}{3 \cdot 1!} + \frac{x^5}{5 \cdot 2!} - \frac{x^7}{7 \cdot 3!} + \dots \right) \\ &= \frac{2}{\sqrt{\pi}} \sum_{n=0}^{\infty} \frac{(-1)^n \cdot x^{2n+1}}{(2n+1) \cdot n!} . \end{aligned}$$

eq. 3-23

This is a good model for describing gaussian range distributions of the stopped fragments and was used up to 40th order for fitting the NDCs. In fig. 3-35 the derivatives of the fitted error functions are plotted.

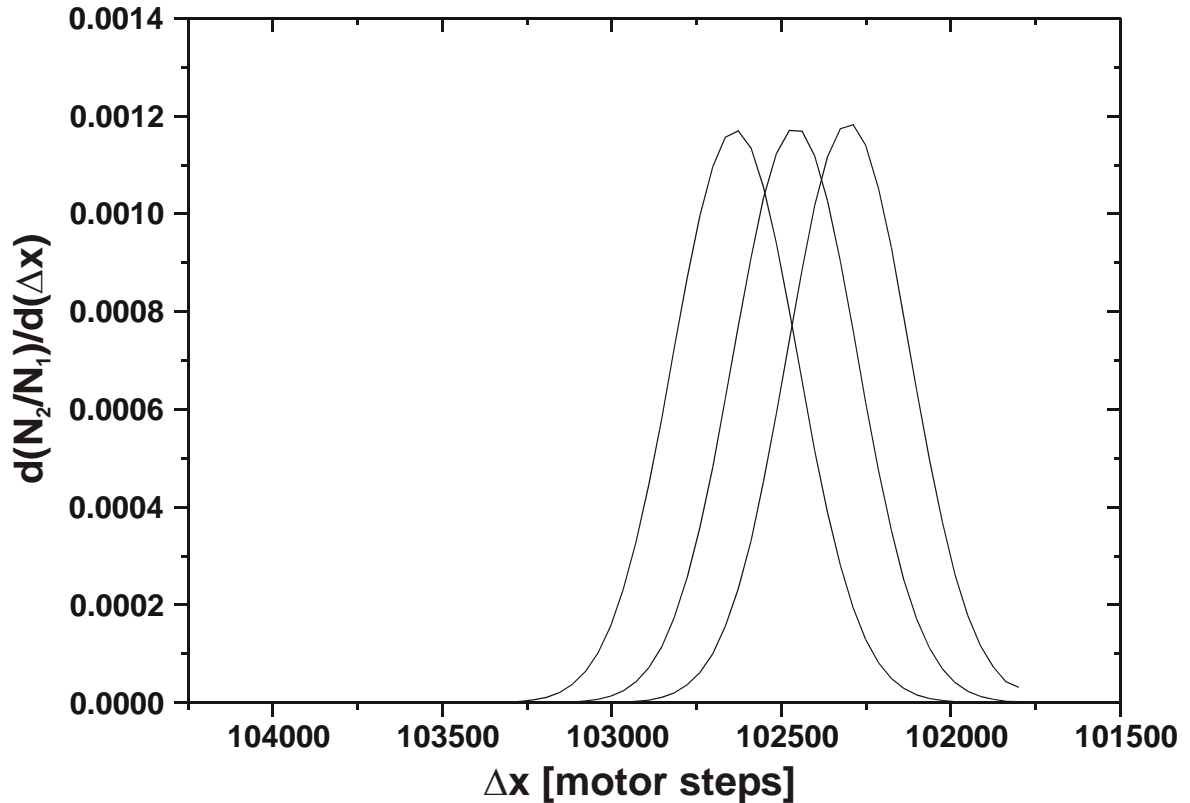


fig. 3-35 The derivatives of the NDC's shown in fig. 3-34 as a measure for the Gaussian range distribution of the stopped fragments.

The data from the fourth anode had to be neglected as the preamplifier for this channel did not work properly.

The measurement was repeated for various degrader angles and the result is shown in fig. 3-36 for the two cases of ⁵⁶Ni fragments with no focusing and for the case of focusing. As described before it was necessary to correct for the misalignment of the discs. The actual angles after correction using eq. 3-20 were as follows:

1. No focusing $\alpha = -4.80 \text{ mrad}$
2. focusing $\alpha = 6.24 \text{ mrad}$,
3. over focusing $\alpha = 17.74 \text{ mrad}$.

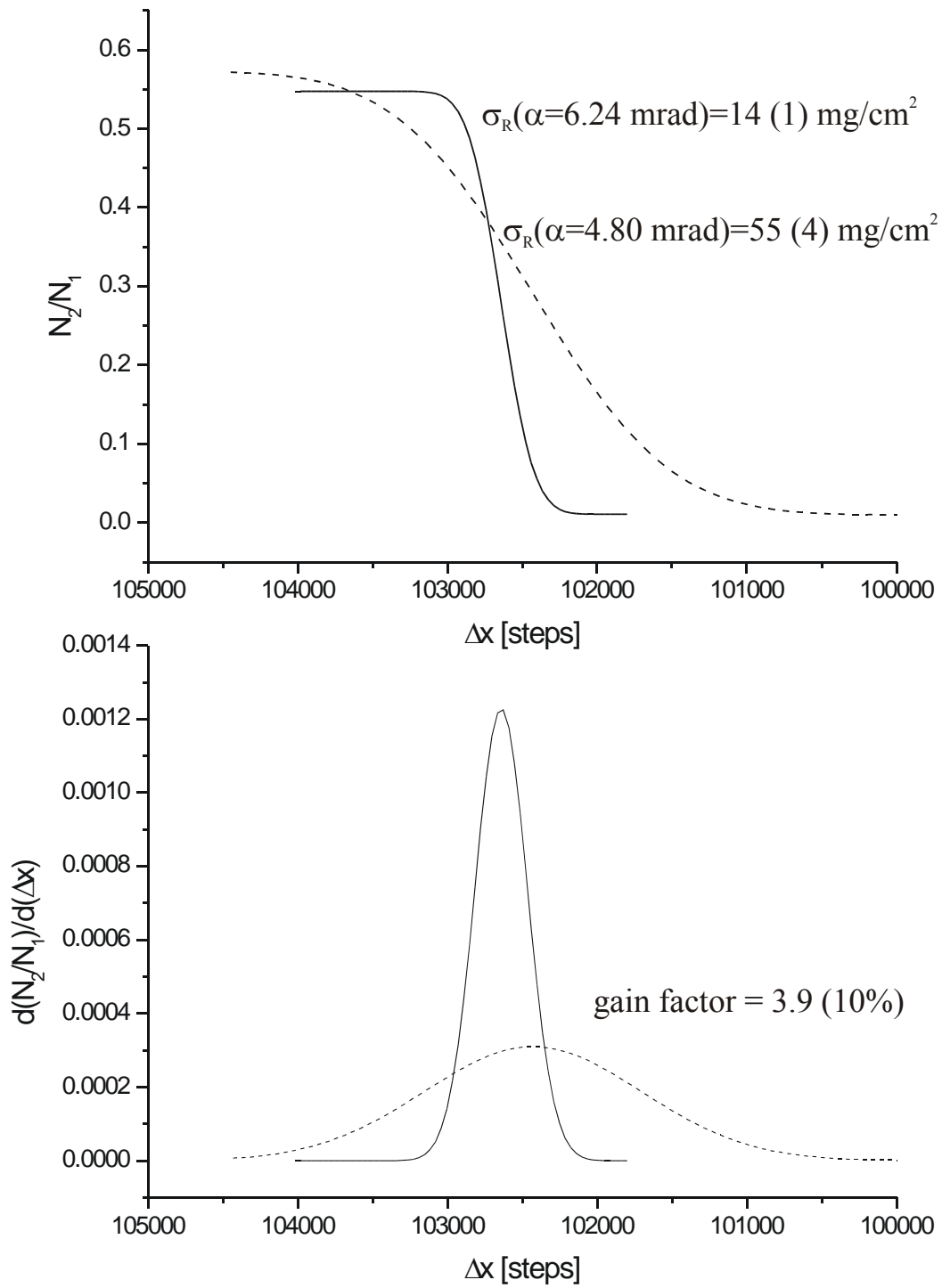


fig. 3-36 Range focusing of ^{56}Ni fragments. The upper graph shows the error-function fit to the number distance curves measured for a focusing angle of $\alpha=6.24 \text{ mrad}$ (solid line) and with $\alpha=4.8 \text{ mrad}$ (dashed line). The lower graph shows the corresponding range distributions. The gain in range straggling in the case of ^{56}Ni is almost a factor of four.

4 Results and discussion

4.1 Charge-state distributions

From the abundances of each charge state the mean charge state was determined according to eq. 3-3 and is plotted versus the energy after the target, E , for ^{58}Ni and ^{136}Xe projectiles in fig. 4-1.

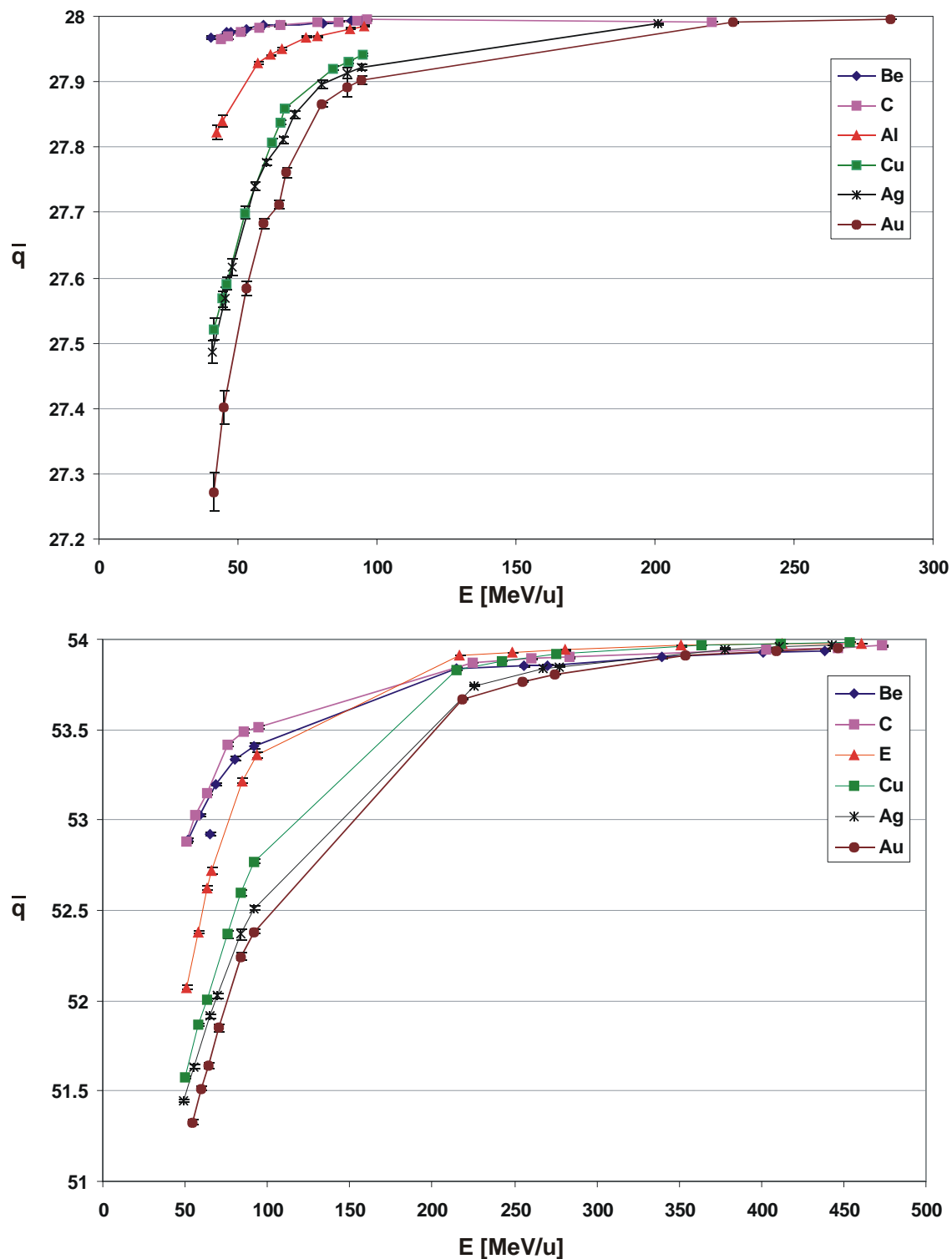


fig. 4-1 Measured mean charge of ^{58}Ni versus the Energy E after the targets (top) and measured mean charge of ^{136}Xe versus the Energy E after the targets. The lines are drawn to guide the eye only.

The mean charge decreases for lower energies and in the case of Ni projectiles the beryllium targets are the best strippers followed by carbon. For Xe in the low energy regime between 50 and 100 MeV/u , the carbon targets are the slightly better stripping material.

Comparing these results to the predictions of the simple Pierce and Blann formula (eq. 2-19) without Z_2 -dependence shows deviations from the measured values, especially in the low energy regime. For Nickel the prediction of this simple model is quite good, especially for the copper and the silver targets. For the lighter targets the P&B formula underestimates the mean charge by up to 1.5%, yet for the gold targets it overestimates the mean charge up to 1%.

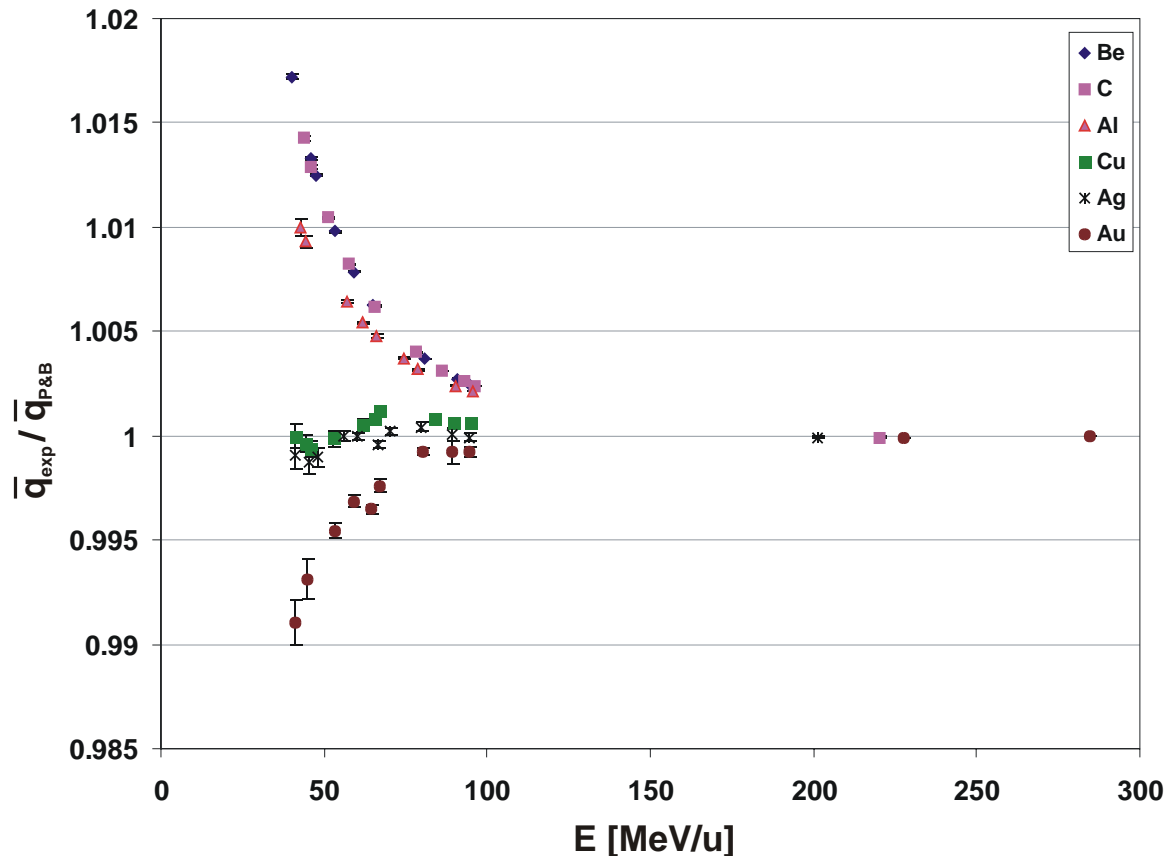


fig. 4-2 Measured mean charge of ^{58}Ni divided by the prediction of the Pierce and Blann formula versus the Energy E_{out} after the target.

For xenon projectiles the situation is somewhat different. The overall agreement with the measured mean charge is worse than for nickel and deviations in the low energy regime up to almost 4% for the light target materials occur. For the heavy targets, silver and gold, there seems to be a tendency to overestimate the mean charge for energies between 200 and 60 MeV/u and to underestimate for lower energies. Unfortunately there is a large gap in the data taken so it is not possible to confirm this trend for the lighter target materials.

The main result here is that for energies above 200 MeV/u the simple approach of the P&B formula is good enough to predict the mean charge state with an accuracy of about 0.1 % for nickel and better than 0.5 % for xenon projectiles.

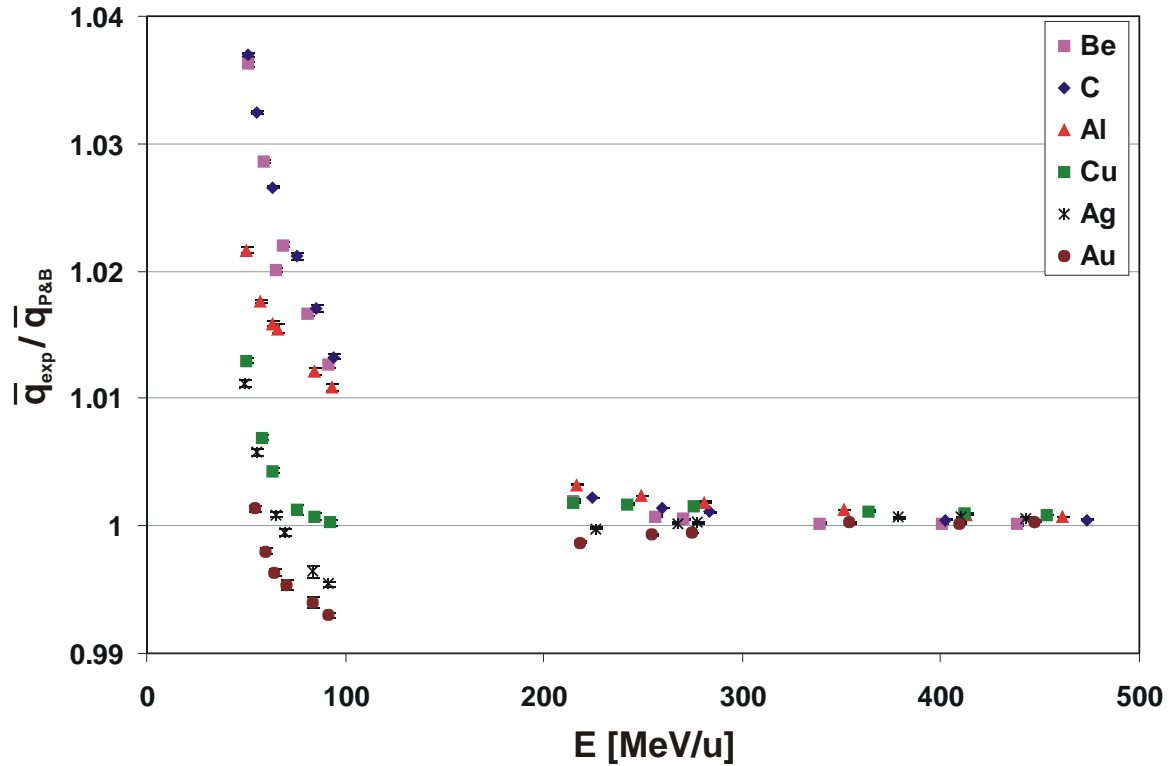


fig. 4-3 Measured mean charge of ^{136}Xe divided by the prediction of the Pierce and Blann formula versus the Energy E .

The better approach to predict the mean-charge state for both cases is the code GLOBAL [SCH98] as shown in fig. 4-4 and fig. 4-5.

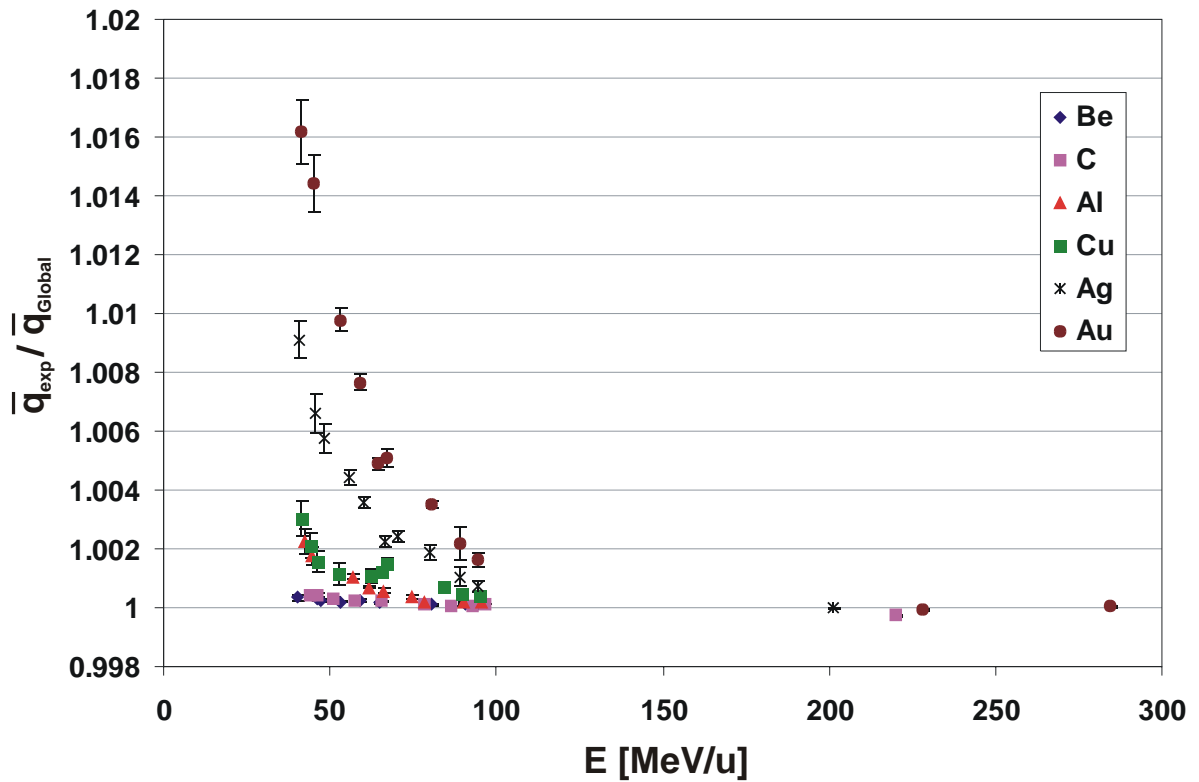


fig. 4-4 Measured mean charge of ^{58}Ni divided by the prediction of the computer code Global versus the energy E .

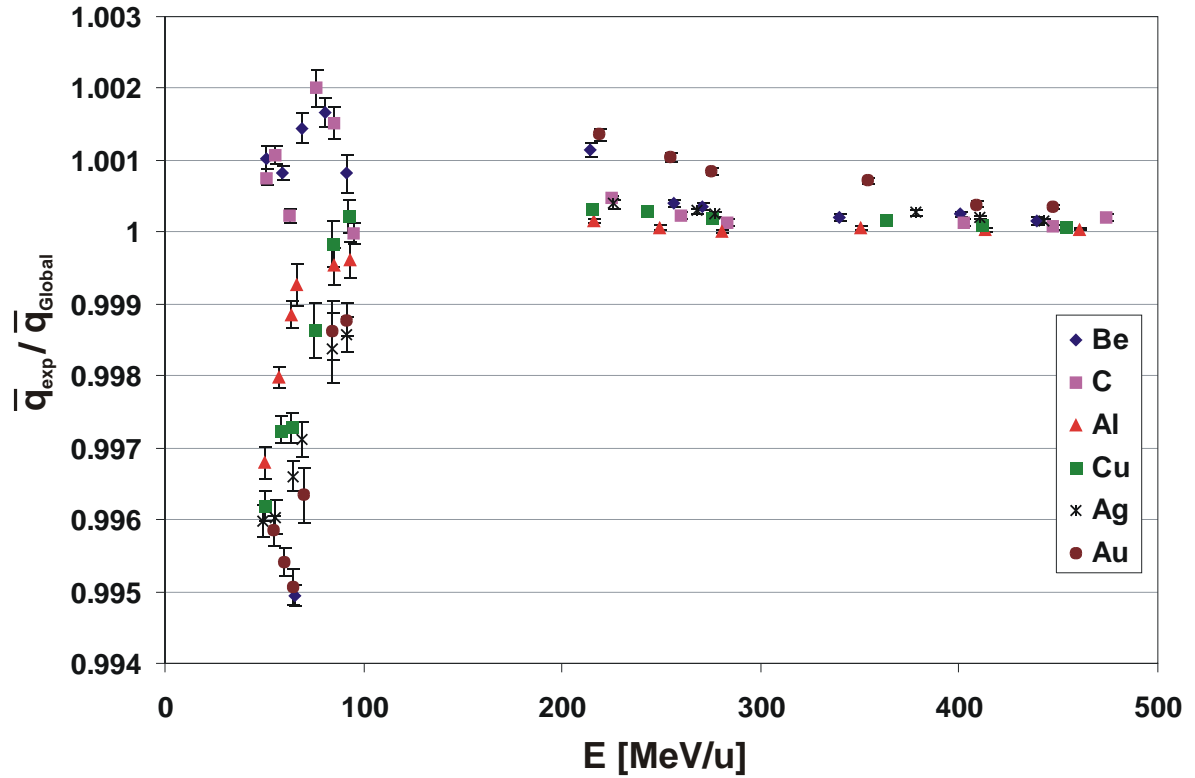


fig. 4-5 Measured mean charge of ^{136}Xe divided by the prediction of the computer code Global versus the energy E .

Especially for the light targets, Be and C, the agreement with the data is very good. Even for the heaviest target, Au, the deviations are only 1.6% for the low energy nickel beam and only 0.5% for xenon projectiles. A complete list of charge-state measurements for all beam target combinations is tabulated in Appendix B, as are the measured abundances of each charge state.

4.2 Stopping powers

The intent of this work was to fill the gap of available stopping-power data above 30 MeV/u . A summary of the data obtained is shown for Ni projectiles in fig. 4-6 and for Xe projectiles in fig. 4-7. The graphs show the results of this experiment in addition to all the available data for this beam and target combinations and energy regime available in the collection by Helmut Paul [PAU03]. The data is also compared to two simulations: SRIM 2003 for the whole energy range, and ATIMA above 30 MeV/u (ATIMA uses an older version of SRIM for values below 30 MeV/u). The prediction by the code PASS is not included in these plots as the difference between the different codes on this absolute scale can not be seen.

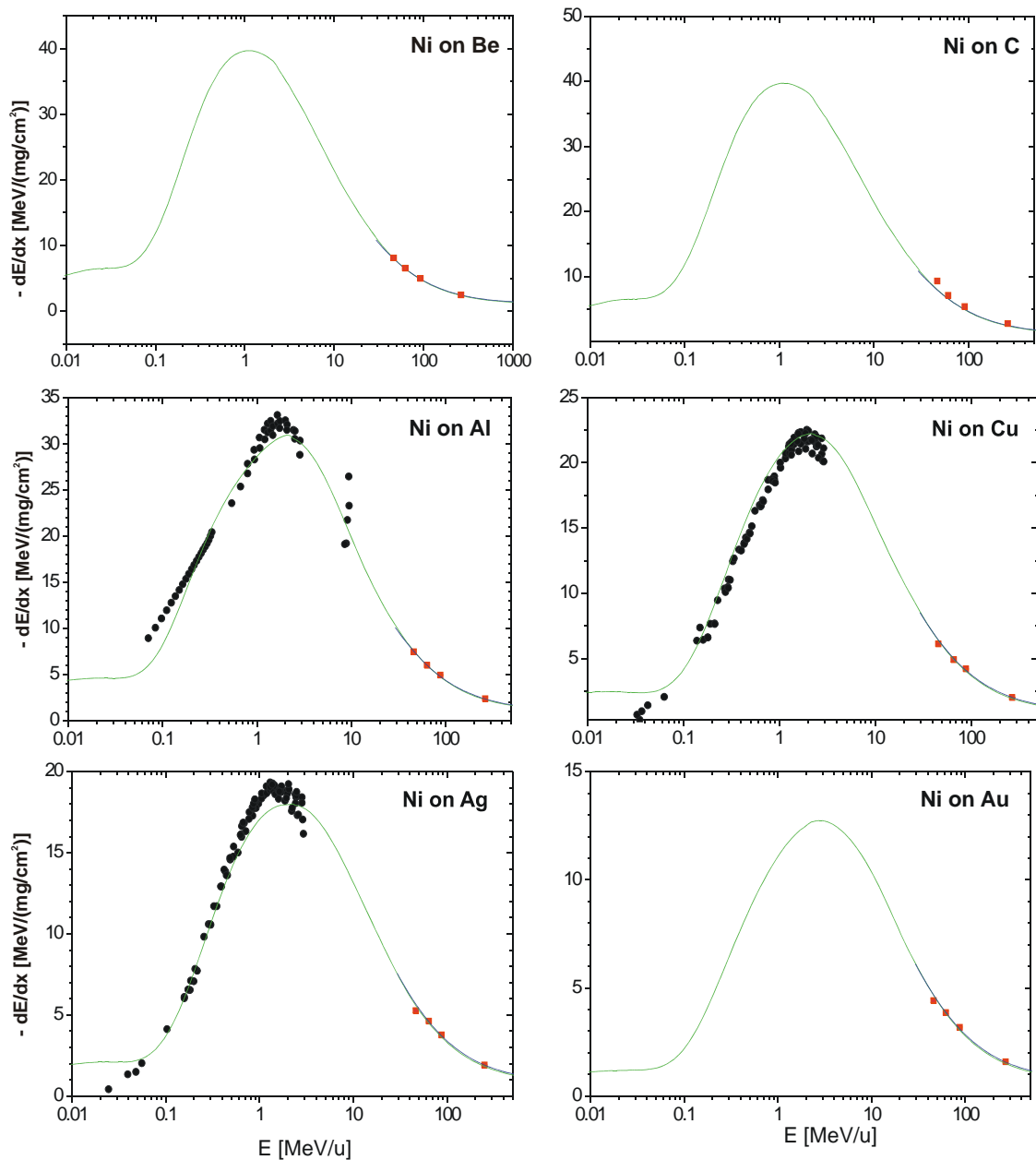


fig. 4-6 The measured stopping power of ^{58}Ni projectiles versus the energy. The green line is the prediction by SRIM 2003 and the blue line the prediction by ATIMA down to 30 MeV/u . The black data points are taken from the collection of stopping-power measurements by Helmut Paul [PAU03]. The red data points are the ones taken from this work.

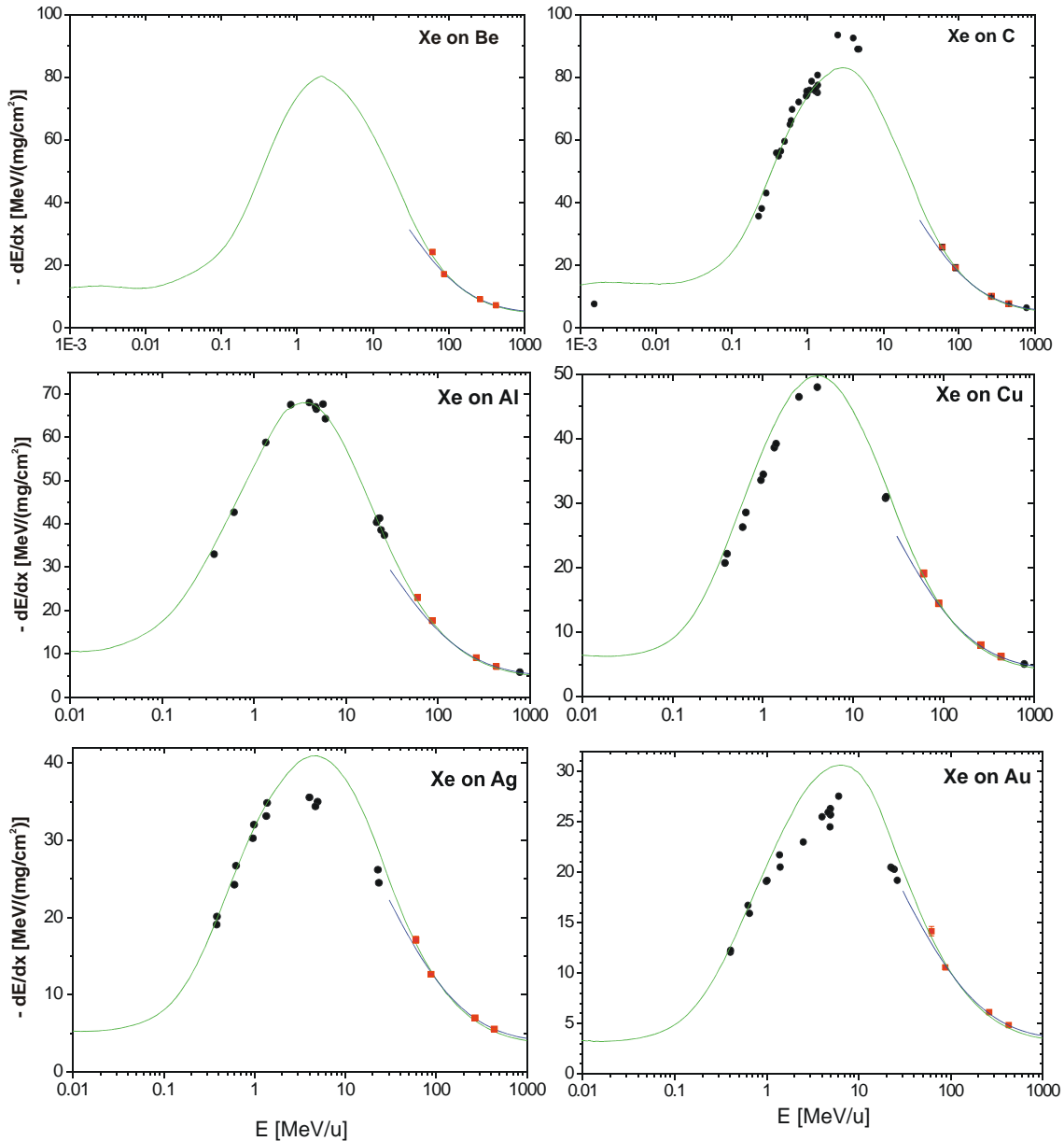


fig. 4-7 The measured stopping power of ^{132}Xe projectiles versus the energy. The green line is the prediction by SRIM 2003 and the blue line the prediction by ATIMA down to $30 \text{ MeV}/u$. The black data points are taken from the collection of stopping-power measurements by Helmut Paul [PAU03]. The red data points are the ones taken from this work.

To compare the measured stopping powers to different theoretical approaches, the data is normalized to the prediction of ATIMA and plotted together with the predictions of SRIM2003 and PASS in fig. 4-8 for Ni and fig. 4-9 for Xe projectiles.

In the high energy regime the predictive power of ATIMA is very good and the deviations are on the order of one percent. For the lightest target, Be, the deviations do not change drastically for the lower energies, but the error bars get bigger. Yet as the targets get heavier there is a clear trend that ATIMA starts to over predict the stopping power. The one measurement for the carbon target with 7% deviation looks very strange and does not fit into this picture. Yet this carbon foil was a stacked foil on two different target ladders and in chapter 4.3 which discusses energy straggling, it becomes clear that these thin carbon targets are not suited for high precision experiments.

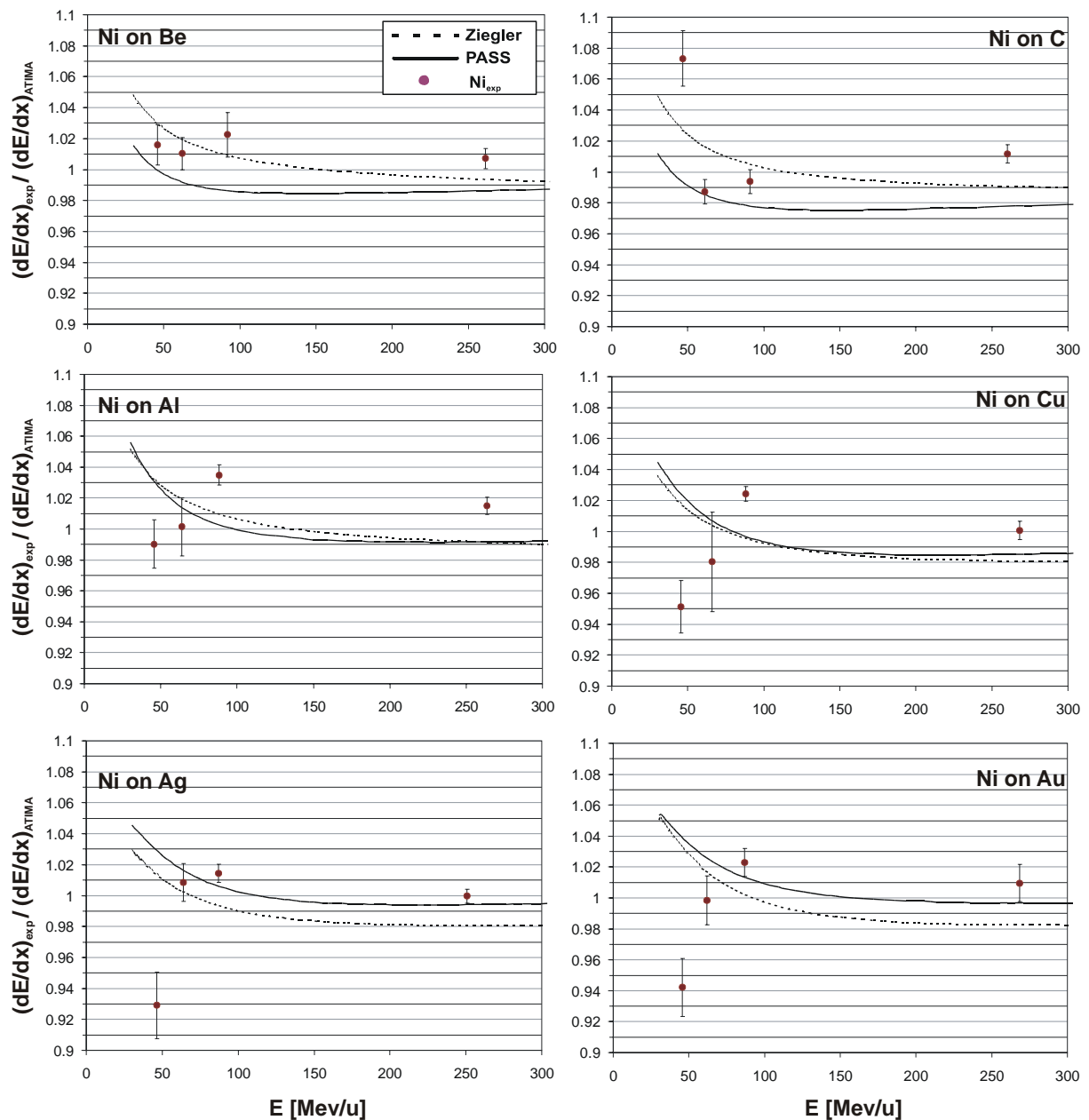


fig. 4-8 Measured stopping power of ^{58}Ni normalized to the prediction of ATIMA plotted versus the energy. For comparison, also shown are the predictions of Ziegler and PASS.

In the high energy regime the agreement of the ATIMA predictions with the data is also true for the xenon projectiles. However, in the low energy regime ATIMA under predicts the stopping power up to 10%. Here, unlike the nickel case, the code PASS seems to do better and even SRIM is closer to the data. Yet, looking at the Cu, Ag and Au targets, there seems to be an indication of a ditch in the stopping power prediction which is unfortunately hard to confirm with the huge gap of more than 150 MeV/u without data points.

Looking at the plot for the charge state distributions of Xe in fig. 4-5 compared to the formula by P&B there seems to be the same trend visible.

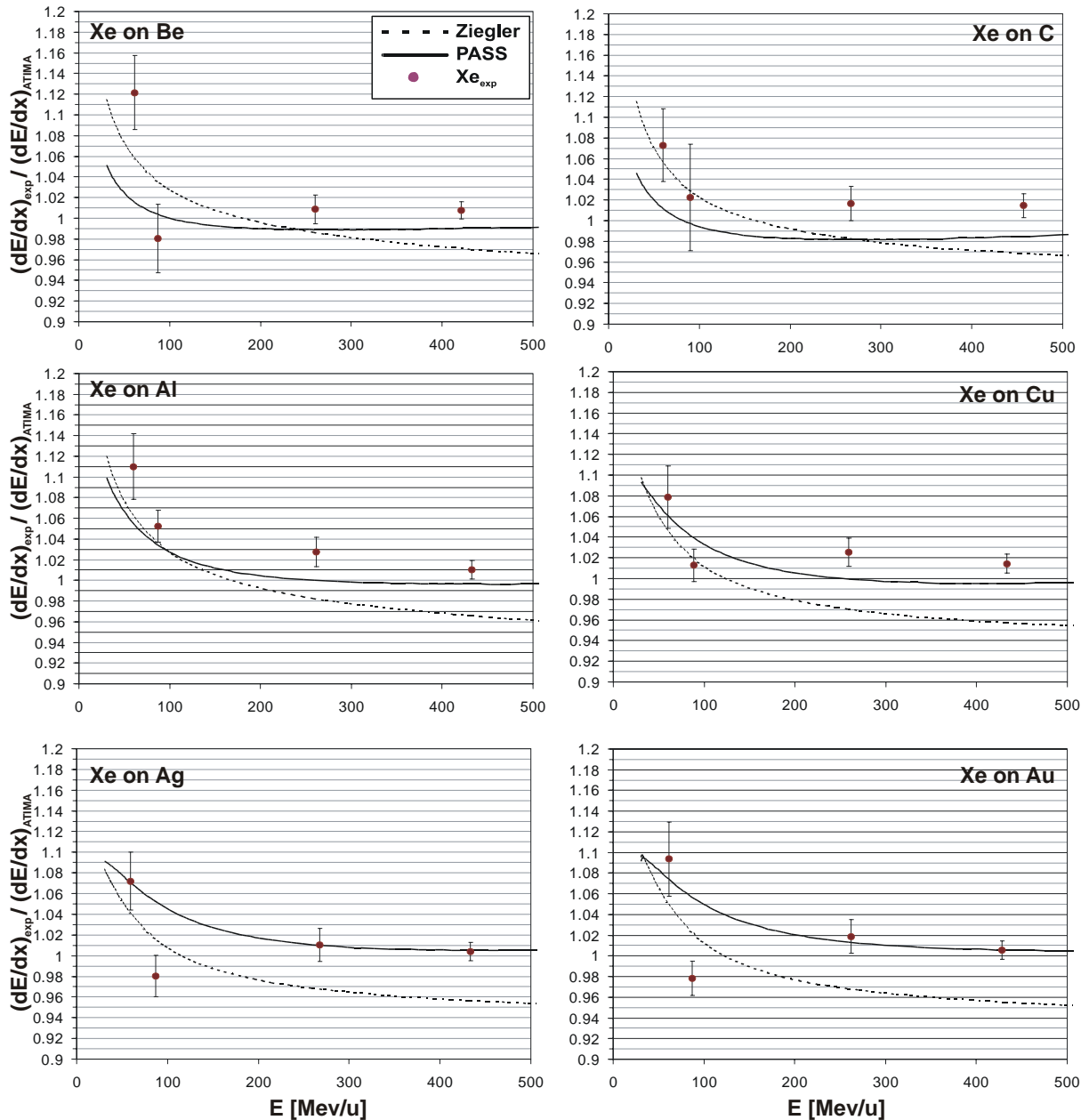


fig. 4-9 Measured stopping power of ^{136}Xe normalized to the prediction of ATIMA versus the energy. For comparison also shown the predictions of Ziegler and PASS.

Following this idea one could instead of using a mean charge calculate the partial stopping $\frac{dE}{dx}(q_i)$ power of each single charge state q_i and sum up these partial stopping powers weighted by their abundance h_i over all charges according to the formula

$$\frac{dE}{dx} = \sum_i h_i(q_i) \cdot \frac{dE}{dx}(q_i).$$

eq. 4-1

To do this ATIMA was used to calculate the stopping power for each single charge state for the averaged energy from the stopping power fit. The charge state distribution for this energy was obtained by graphical interpolation of the charge state distribution curves as shown in fig. 3-8. The resulting stopping powers again normalized to the prediction by ATIMA are shown for Xe in fig. 4-10. As for nickel even at the lowest energies there were

only 4 charge states the changes are below 1% and too small to be significant within the error bars. Yet for xenon one can clearly see an improvement of the prediction with ATIMA. For the light targets Be, C and Al at 50 MeV/u initial beam energy the improvement is of the order of 5%. Going to higher energies and heavier Target materials this trend is still visible, yet within the error bars not significant any more.

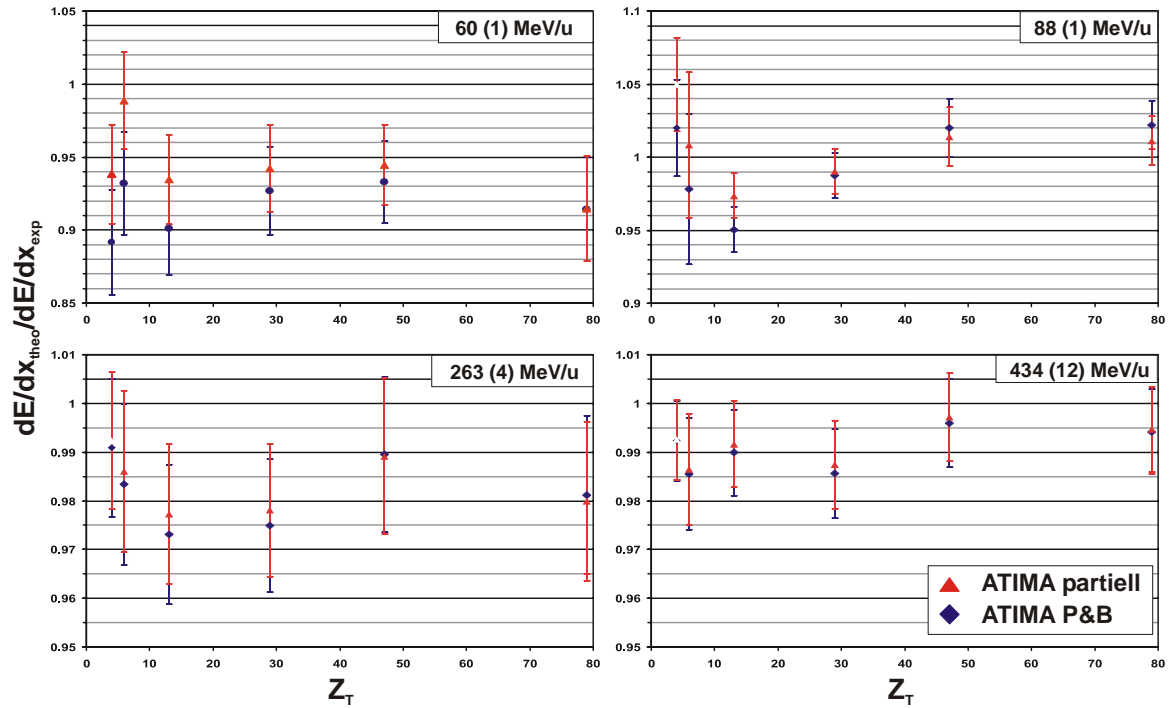


fig. 4-10 Stopping power of ^{136}Xe calculated with ATIMA with partial stopping powers (red) and using the Pierce and Blann formula (blue) for the mean charge versus Z_2 of the target normalized to the experimental values. There is a plot for each initial beam energy.

Thus it is clear that there is still other effects which are not taken into account properly for calculating the stopping power in the low energy and high Z_2 regime.

4.3 Energy and range focusing

With the technique described in chapter 3.2 we have measured the range distribution of ^{56}Ni for three different angles. For ^{54}Co we measured two cases and the range distribution of the ^{58}Ni primary beam was also investigated for comparison. The results are summarized and compared to the predictions by MOCADI [MOCADI], fig. 4-11. MOCADI is a Monte Carlo simulation program to calculate the transport of primary beams and nuclear fragments through ion optical systems described by third order transfer matrices and through layers of matter using the codes GICO [GICO] for the ion optics, EPAX [SÜM00] for the nuclear fragmentation cross sections, GLOBAL [SCH98] for charge state distributions and ATIMA [IWA97] to calculate the energy losses. Within the error bars the measured range straggling for ^{56}Ni and ^{54}Co agrees very well with the predictions by MOCADI. The gain in reducing the range straggling for ^{56}Ni at the corrected angles is almost a factor of four. The large error bar in the ^{54}Co case for -4.8 *mrad* results from a not completely measured number distance curve. This then leads to a high uncertainty in the fitting. But also for Cobalt the agreement is well enough to assume a high predictive power of MOCADI for future experiments. Using the proper angles, meaning 0 *mrad* for no focusing and 8.5 *mrad*, for the focusing measurement would in accordance with MOCADI calculations lead to a reduction of range straggling by a factor of about 4.4. The comparison with the measured range straggling of the primary beam shows that it is in principle possible to have a similar range straggling of fragment beams as with primary beams. This is a very promising result in the prospect of future devices such as gas cells as it will increase their stopping efficiency drastically.

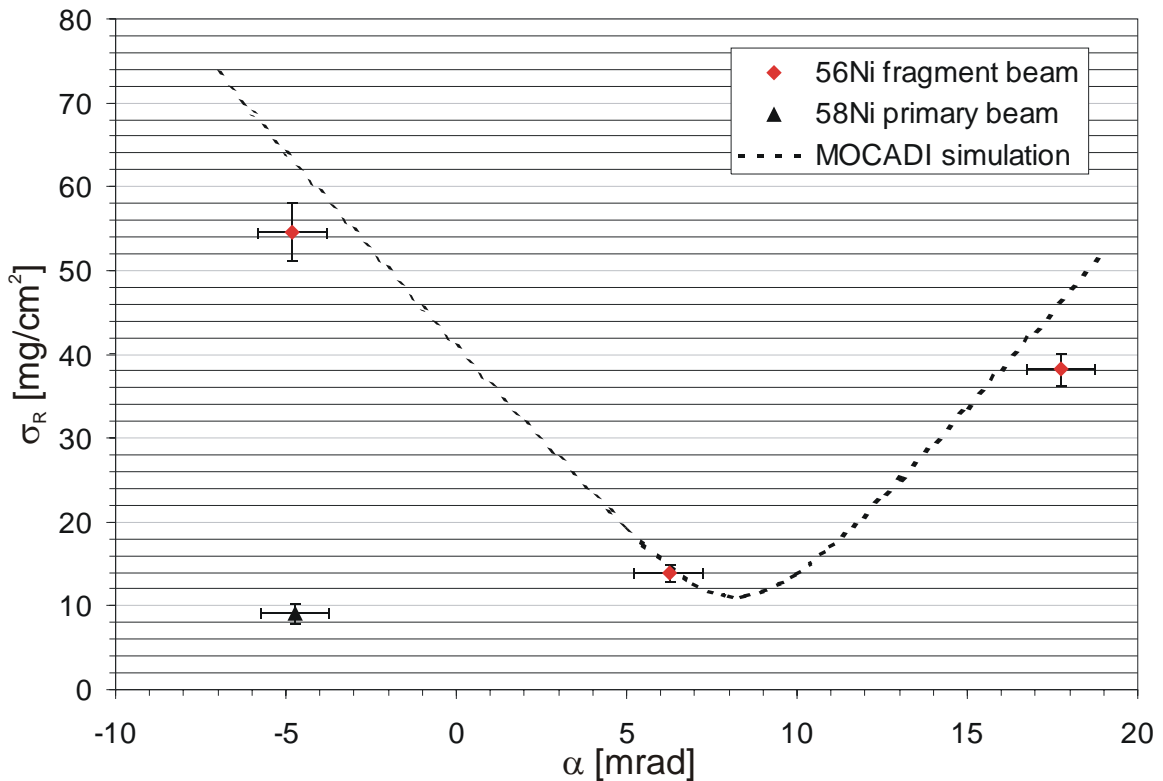


fig. 4-11 Measured range straggling σ_R for ^{56}Ni fragments using different degrader angles α . For comparison the primary beam of ^{58}Ni is shown as well as a prediction by the computer code MOCADI.

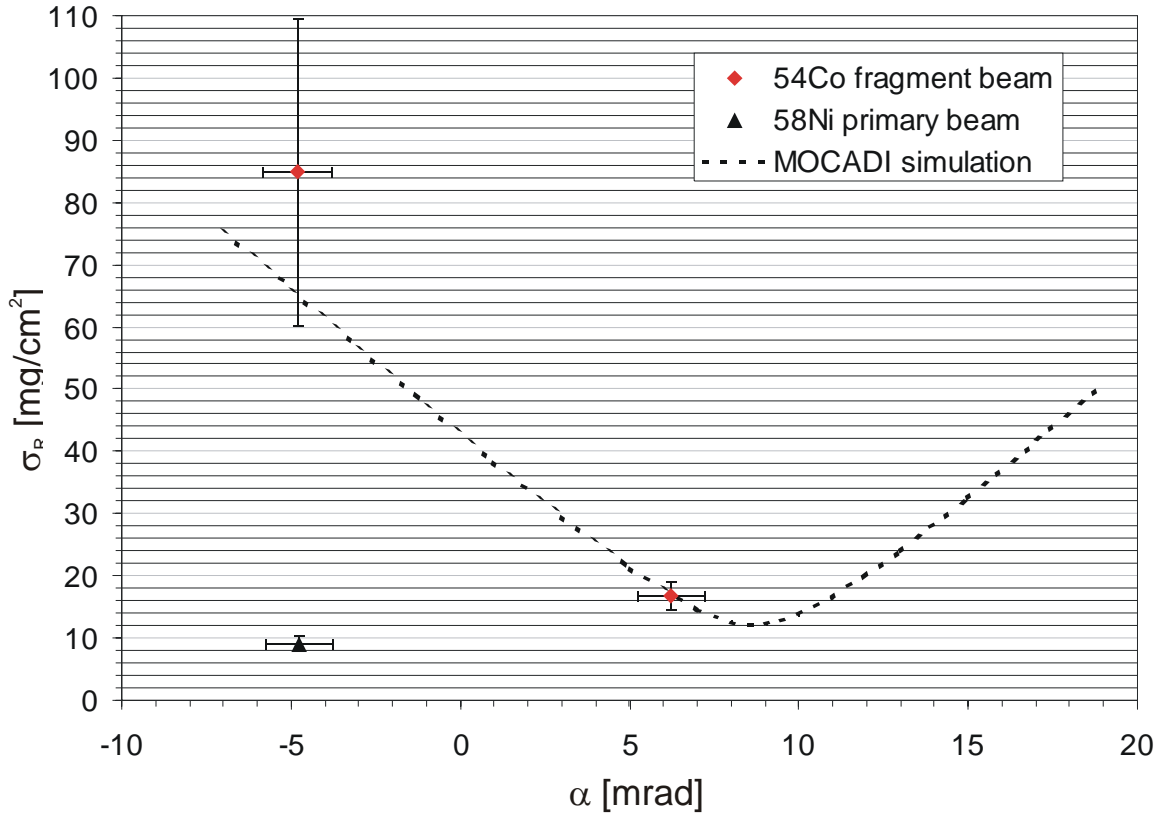


fig. 4-12 Measured range straggling σ_R for ^{54}Co fragments using different degrader angles α . For comparison the primary beam of ^{58}Ni is shown as well as a prediction by the computer code MOCADI.

The technique of range focusing was successfully demonstrated using two different fragment beams at the FRS. Almost a factor of four was obtained reducing the range straggling of ^{56}Ni for which this experiment was optimized. This is a promising result in the prospect of a planed gas cell behind the FRS as this will enhance the number of stopped ions in such a device drastically. Using a new disc degrader with a proper alignment should lead to a range straggling of fragment beams close to that of primary beams. Thus the next steps are to replace the disc degrader and to test different ion optical layouts [CHI03]. The ion optical setting has to be changed in order to have isotopic beams for the focusing experiments. These preparations are needed to finally perform high energy tests with sufficient yields of a gas cell and experiments using this expertise with the FRS-Ion-Catcher gas cell as proposed for the low energy branch of the SUPER-FRS [CDR01] and for the RIA project [RIA00].

5 FRS-Ion Catcher - a new instrumentation for research with exotic nuclear beams

As discussed in chapter 2.2 there are two main methods for the production and separation of exotic nuclei at present facilities:

- the ISOL approach where the exotic nuclei are created by a light ion beam impinging on a thick target and later extracted, ionized and accelerated.
- the in-flight separation, where a beam of energetic heavy ions impinges on a thin target and the reaction products are carried forward by the kinematics and separated in-flight.

A novel approach combining the positive aspects of both techniques (the high yields and beam quality of ISOL with the short delay times and universality of in-flight fragmentation) could significantly improve beam production for chemically challenging and very short-lived isotopes. Worldwide many institutes are currently developing techniques to stop and thermalize ions in gas-filled ion catchers.

GSI currently collaborates in this field with many different institutes to develop such a system for relativistic ions. Argonne National Laboratory (ANL) is on the forefront of research to develop and test a gas cell setup for implementation at future facilities. There, the gas cell was designed, tested off-line with a ^{252}Cf source and on-line with low energy beams before it was shipped to GSI. The IONAS group of Giessen is providing a 3-way **RFQ** system (**R**adio **F**requency **Q**uadrupole [DAW76]) and an orthogonal time of flight mass spectrometer. The extraction RFQ was provided by the LEBIT group at MSU and the purification station and the tape station will be provided by the University of Leuven.

5.1 Setup of the FRS-IC

The FRS-IC will stop, cool and bunch relativistic ion beams and further direct them to different high precision experiments as shown in fig. 1-3. To do this quickly and efficiently, different components are needed. A schematic overview of the required components is shown in fig. 5-1.

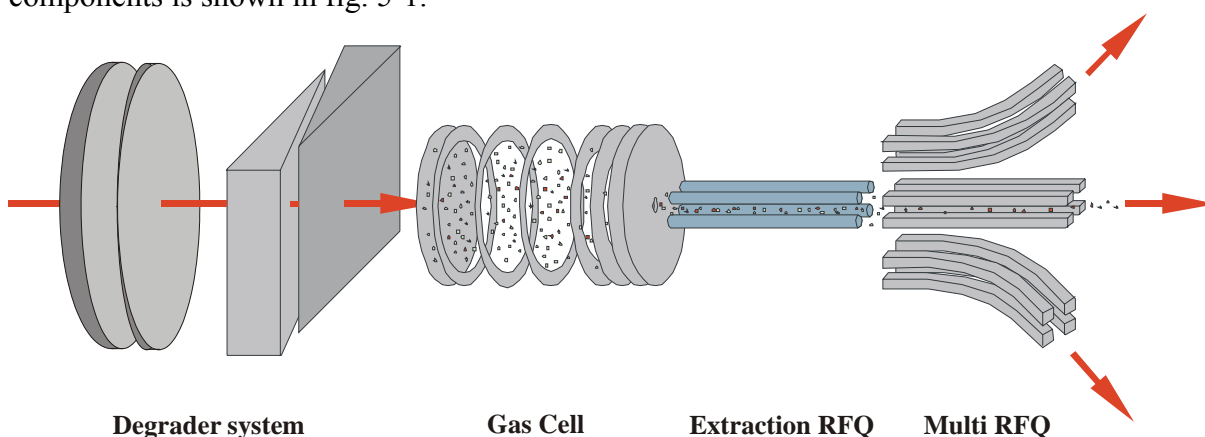


fig. 5-1 Schematic picture of the FRS-Ion Catcher setup. The high-energy ions delivered from the FRS are slowed down and energy bunched in the degrader system. They eventually enter a gas cell where they are stopped and, by means of applied AC and DC fields, directed and dragged towards the gas cell exit nozzle. The high gas flow pushes the ions through the nozzle into the extraction RFQ where

they are separated from the gas by differential pumping. The next stage, the Multi-RFQ, serves as a distribution device to three different experimental outlets and as a further differential pumping stage.

The degrader system and the ion optical mode of the FRS for range bunching was already described in detail in chapter 3.2. In the gas cell the ions are stopped and leave the cell together with the gas through the exit nozzle. In the extraction RFQ the ions are guided further and are separated from the gas by means of differential pumping. The ions then enter a Multi-RFQ with another differential pumping stage and they can be distributed to different experimental setups.

5.2 The gas cell

Basically, the gas cell is a volume filled with He gas of high purity. It has an entrance window of sufficient thickness to withstand the required gas pressures of up to 1 bar and an exit nozzle of 1.5 mm in diameter through which the ions and gas leave the cell. To increase the speed for extracting the ions and the efficiency of this device the FRS gas cell combines three forces as schematically shown in fig. 5-2.

To minimize the duration of the ions inside the cell, a longitudinal electric DC field is applied to drag the ions toward the exit nozzle. The shorter the time an ion needs to travel through the gas, the less probable are losses due to recombination with contaminants inside the gas.

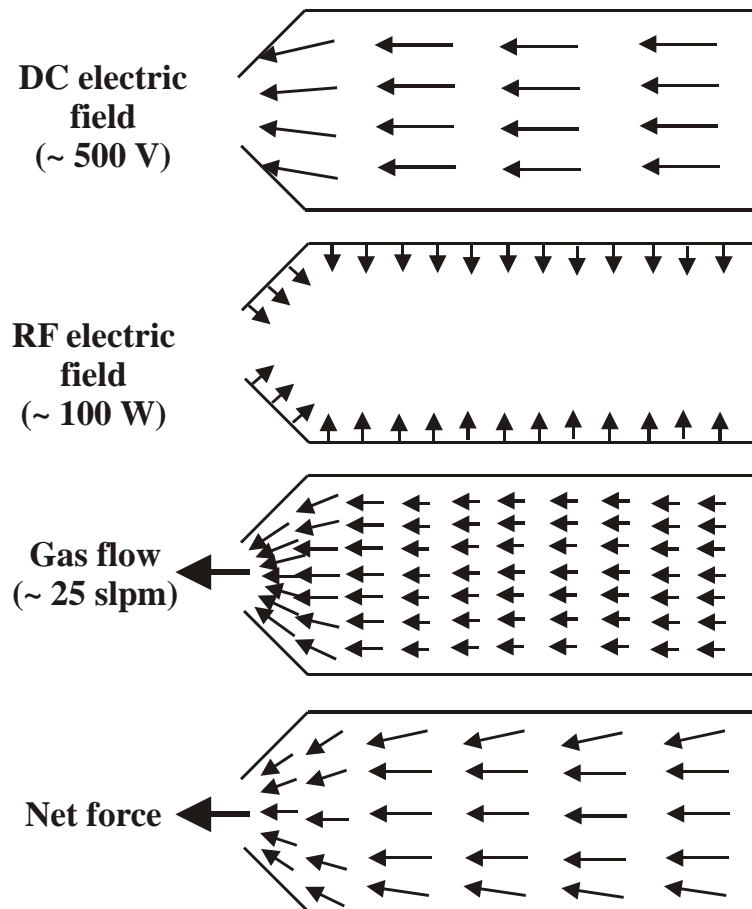


fig. 5-2 Illustration of the working principle of the FRS-IC gas cell. Over the entire length a DC field gradient is applied to drag the ions toward the exit nozzle. An additional AC field is used to repel the ions from the cell electrode surfaces, a process referred to as RF-focusing. The gas flow, being strongest at the exit nozzle, also drags the ions and finally pushes them through the nozzle. The bottom picture illustrates the net force an ion sees inside the cell.

To prevent the ions from hitting the cell surface and getting lost, an additional RF field is applied to the cell body superimposed upon the DC field. This technique is called RF-focusing. The stacked ring ion guide technique was introduced in 1969 by [BAH69]. When an RF voltage is applied between each pair of neighboring electrodes, an ion at rest on axis is subjected to an oscillating field whose time-varying instantaneous amplitude varies with axial and radial location. The time-averaged effect of a rapidly time-varying RF-potential on a slow moving ion is well represented by a static ‘pseudopotential’ that is nearly flat near the central axis and that increases steeply with radial displacement. Because of its flat steep-walled ‘pseudopotential’ well, this ring ion guide with only RF is very well suited to repel the ions from the gas cell surface.

Finally, in the vicinity (few *mm*) of the exit nozzle of the gas cell the dragging force of the gas becomes strong and pushes the ions through the nozzle.

A technical drawing of the cell is shown in fig. 5-3 and a photo of the gas cell after assembly at Argonne is shown in fig. 5-4. It has an overall inner length of 1.4 *m* and consists of more than 7400 single parts of which more than 4000 are prepared for ultra high vacuum conditions. The inner diameter of the cell is 25 *cm*. The base pressure reached inside the cell after bake out is routinely about 10^{-7} *mbar* even though the access port for pumping shown in the upper left of fig. 5-4 only has a diameter of 3 *cm*². The different sections of the gas cell are sealed with indium wire. The entrance window of the cell is a combination of 4.2 *mg/cm*² Mylar and 3.1 *mg/cm*² HAVAR.

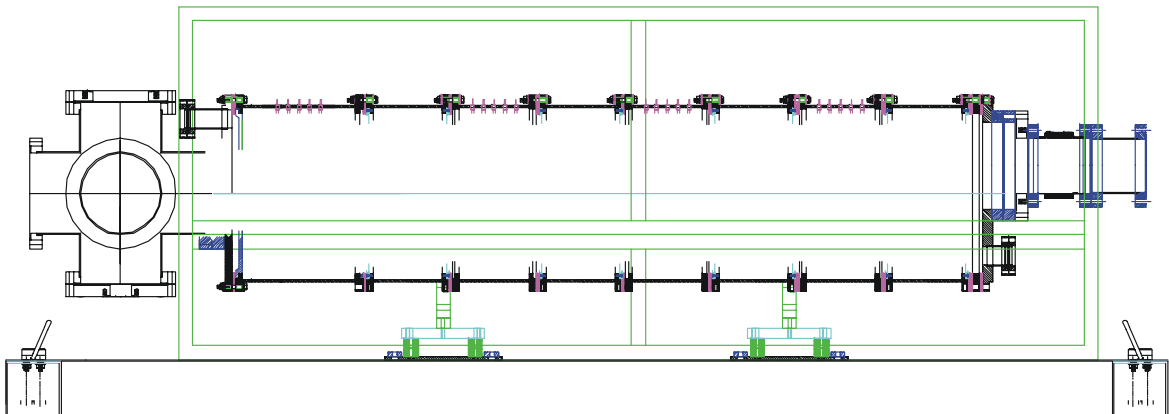


fig. 5-3 Schematic drawing of the FRS-Ion Catcher and extraction RFQ section. The ions enter the cell on the right through the window (blue) which is mounted off-center. Below the window is the pumping port used during bake out. The cell body itself is 1.4 *m* long. At the left is the vacuum chamber for the extraction RFQ. The green box around the cell is the high voltage case installed for safety reasons.

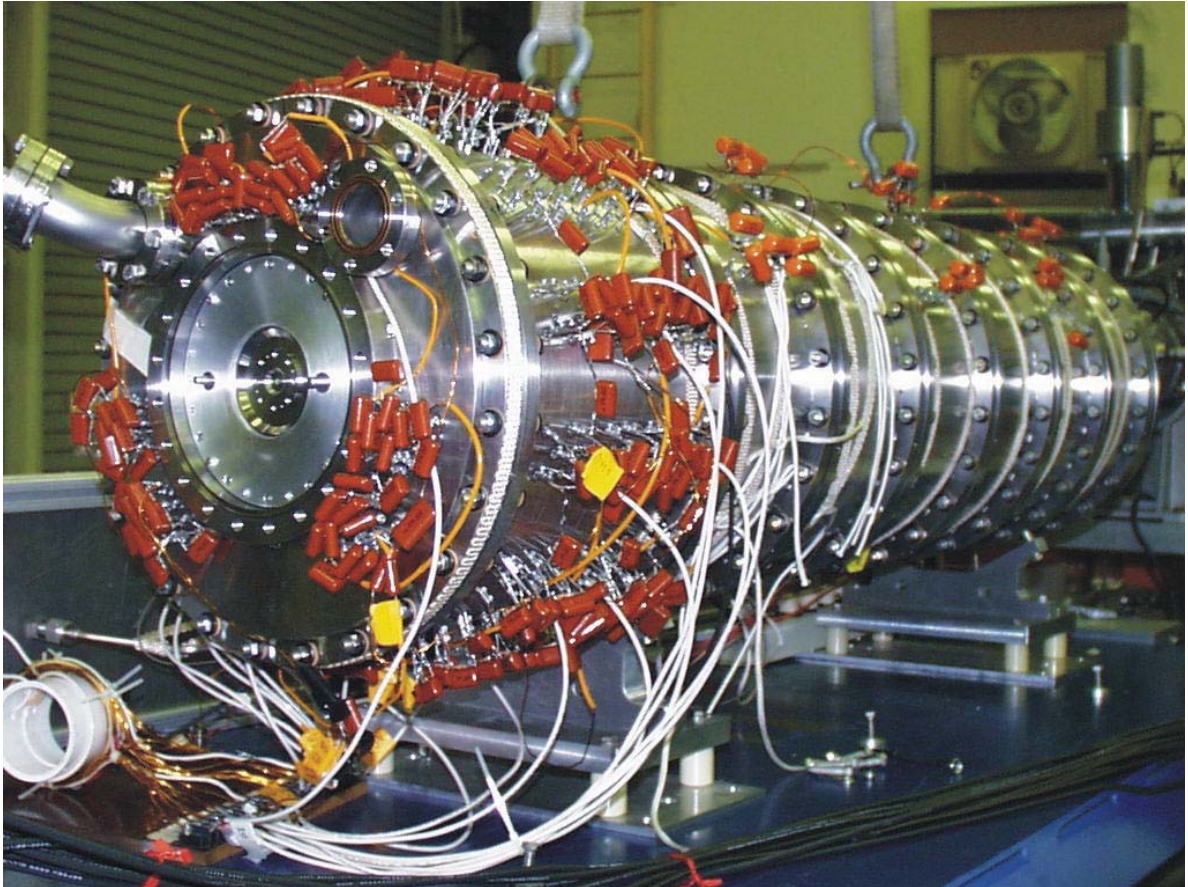


fig. 5-4 Photo of the gas cell after assembly at Argonne. At the back of the gas cell is the entrance window (hidden from view on the right) and in the front is the cone with the exit nozzle (shown on the left).

At the heart of this gas cell is the exit nozzle cone shown in fig. 5-5. It consists of 278 electrode rings with varying inner diameter. Each ring has a thickness of 0.43 mm with a surface flatness lower than 0.025 mm . The spacing between the electrode rings is 0.38 mm . The inner diameter of the first electrode is 25 cm , the same as the inner diameter of the gas cell, and tapers off to 1.5 mm which is the same diameter as the exit nozzle.



fig. 5-5 The exit nozzle cone of the gas cell. It consists of 278 electrode rings with varying diameter.

The gas cell was tested off-line with a $5 \mu\text{Ci}$ ^{252}Cf source and on-line at the ATLAS accelerator with low energy beams of ^{25}Al having 4.15 MeV/u and ^{37}K having 6.6 MeV/u [SAV04]. The advantage of characterizing the gas cell with these low energy beams is the well-defined stopping volume, as the range straggling associated with these beams is on the order of only a few *cm*. Thus it is possible to test the efficiency of the gas cell versus the position of the stopped ions. Also the delay time for extracting the ions from the cell can be obtained as a function of the stopping position.

The experimental setup for these tests is shown in fig. 5-6. The ions coming from the gas cell are retained in the extraction RFQ while the He gas is removed by differential pumping. The next differential pumping stage is also a RFQ, but the DC potential is shaped at the end of the stage to accumulate and bunch the ions in what is called a linear Paul trap. From this trap the ions are ejected and accelerated in an acceleration column to -1500 V for time of flight mass measurements. To measure the flight time, a micro-channel plate (MCP) detector system is placed at the end of the 1.5 m – long transfer line. With a mechanical feed through, it is possible to place instead a Silicon (Si) detector to detect the β -activity from the ions by first implanting the ions onto a biased foil in front of the detector. Thus one has two independent ways of measuring the transport efficiency of the system. A photo of the experimental setup as it was installed at Argonne is shown in fig. 5-7.

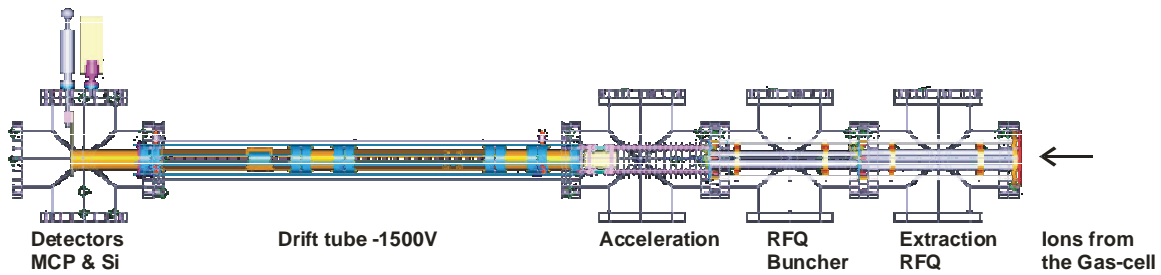


fig. 5-6 The experimental setup for the gas cell tests at Argonne. The ions enter the extraction RFQ at the right side of this figure behind the gas cell which is not shown here. In this first section the ions are retained by the RFQ field while the gas is removed by differential pumping. The 2nd section of the RFQ has a linear Paul trap for accumulating and bunching the ions. After the Paul trap is an acceleration column with a 1.5 m drift tube for time of flight mass measurements. At the end of the drift tube are micro-channel plates to measure the ions' TOF and a Si detector to monitor the β -activity.

The efficiency achieved in the off-line tests was on the order of 30 to 40% and 10 to 30% for the on-line tests. The extraction time was determined to be below 30 ms. As these tests were done at low energies to characterize the cell performance according to the position of the stopped ions, a gas pressure of 250 mbar inside the cell volume was sufficient.

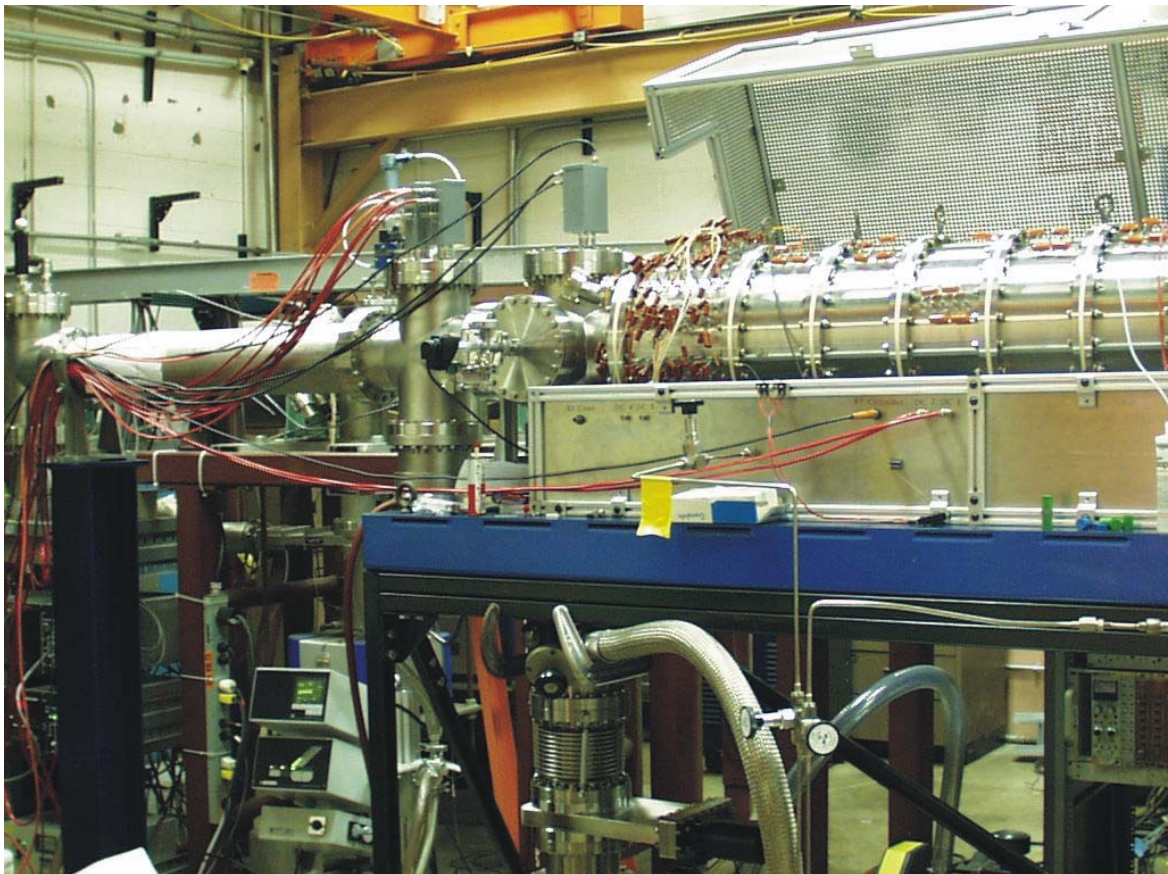


fig. 5-7 Photo of the gas cell setup at Argonne. The gas cell shown at the right is inside a HV-cage which is open in this picture.

For the on-line runs at GSI behind the FRS, the situation is somewhat different. The beams have much higher energies and even with the range bunching technique the range straggling is on the order of the gas cell length at a pressure of 500 mbar, or about 8 mg/cm². (Take ⁵⁶Ni fragments, for example, where $\sigma_R = 9 \text{ mg/cm}^2$ according to the results

in chapter 4.3.) The strength of the gas flow is determined by the pressure inside the cell, the diameter and length of the exit nozzle, as well as the pressure in the following extraction RFQ section. The flow in this high pressure regime can be calculated using [ROT76]

$$Q = AP_1 \left(\frac{P_2}{P_1} \right)^{\frac{1}{\gamma}} \cdot \sqrt{\left[\frac{2\gamma}{\gamma-1} \cdot \frac{R_0 T_1}{M} \cdot \left[1 - \left(\frac{P_2}{P_1} \right)^{\frac{\gamma-1}{\gamma}} \right] \right]}$$

eq. 5-1

where Q is the gas flow, A is the surface area of the nozzle, γ is the ratio of the specific heat at constant pressure to the one at constant volume, R_0 is the gas constant, T represents the temperature of the gas, P is the pressure and M is the molecular weight of the gas. The indices 1 and 2 refer to the two vacuum chambers with differing temperature and pressure.

For a gas cell pressure of 500 *mbar* with a nozzle diameter of 1.5 *mm*, the requirements for pumping are challenging. For efficient transport of the ions in the extraction RFQ, the pressure in the extraction RFQ should be at least three orders of magnitude lower, around 0.5 *mbar*. These gas pressures are suggested initial values and will be changed and optimized during the tests. So from eq. 5-1 a flow of about 25 standard liters per minute [*slpm*] is expected which has to be pumped by the first differential pumping stage.

These high flow rates need special consideration for all parts concerning the gas handling system, starting with the gas supply, the purification system, the flow controllers and, last but not least, the pumps.

The gas purification is a two-stage system consisting of a cold trap to freeze out contaminants and a commercially available purifier (Mono-Torr) (See fig. 5-8).

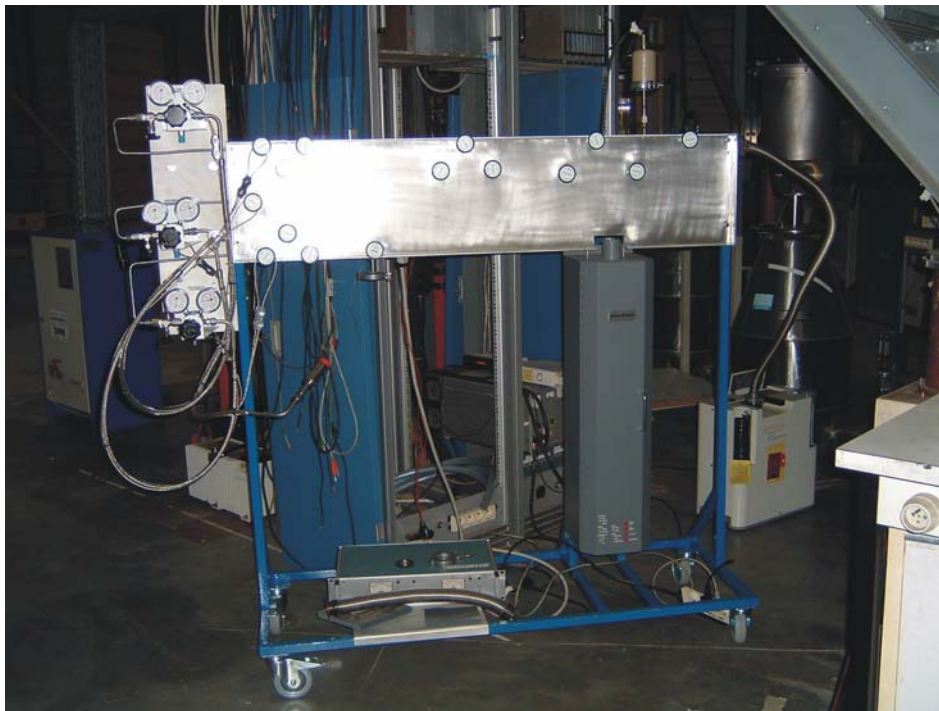


fig. 5-8 A photo of the two-stage purification system during assembly at Leuven. The first stage is a cold trap to freeze out most of the contaminants from the Helium buffer gas. The second stage is a

commercially available Mono-Torr purifier. The challenge and the high costs herein are due to the high flow rates of around 25 slpm.

5.3 The vacuum system

For the first differential pumping stage a roots-blower is used with $5000\text{ m}^3/\text{h}$ capacity. To prevent oil vapors from the roots blower pump entering the extraction RFQ region a water-cooled baffle is installed in the pumping line. The pump and the pumping line are shown assembled in fig. 5-9. Their performance have already been tested as shown in fig. 5-10.

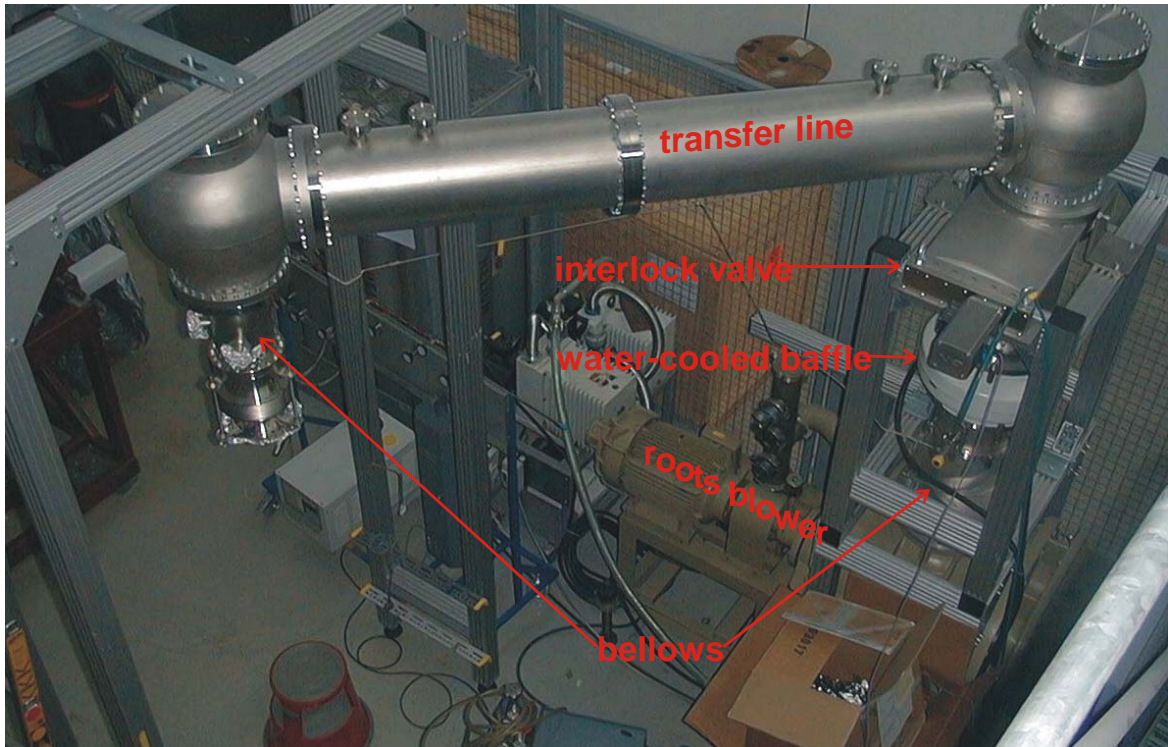


fig. 5-9 The roots blower pump and the transfer line. The transfer line has a bellows on each side to decouple the experimental setup from the vibrations of the pump. Just above the pump are the water-cooled baffle and a big interlock valve to shut off the pump in case of a failure.

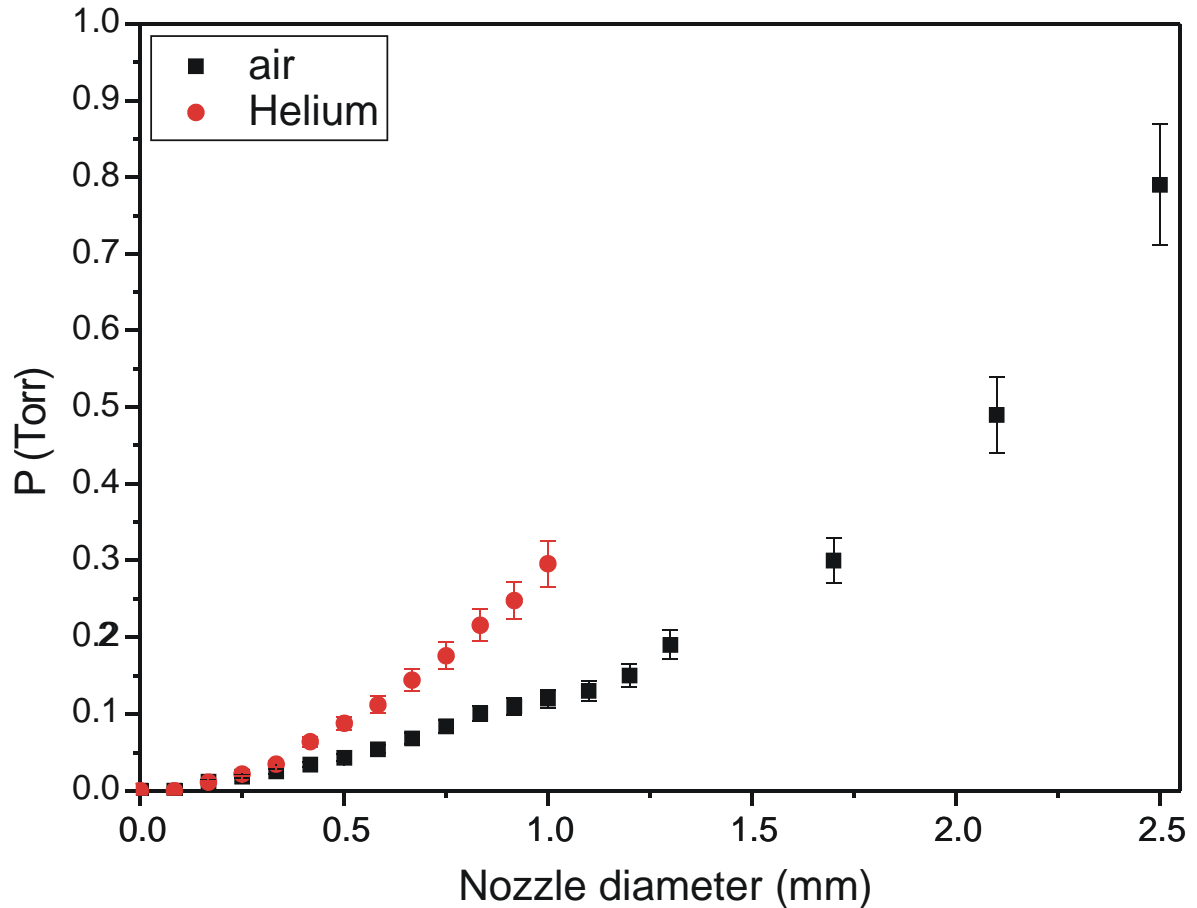


fig. 5-10 Performance test of the roots blower pump. The plot shows the pressure reached in a chamber with a nozzle of varying diameter. In all cases the inlet pressure was 1 bar. The exit nozzle was represented by a needle valve and was roughly adjusted to the corresponding nozzle sizes up to a 1 mm diameter. Above this value, a flange replaced the needle valve and the exit nozzle was represented by drilled holes of different diameters. Even though this was just a rough test, one can clearly see that for a gas cell pressure of 750 Torr or 1 bar, a 1.5 mm nozzle allows for a pressure in the extraction RFQ below 1 Torr.

The bigger challenge is to keep oil vapors from entering the vacuum system. The vapors from the roots blower pump can be seen with a rest gas analysis test as shown in fig. 5-11. To get the system cleaner a water-cooled baffle was installed in the pumping line between the pump and the extraction RFQ but was not yet tested.

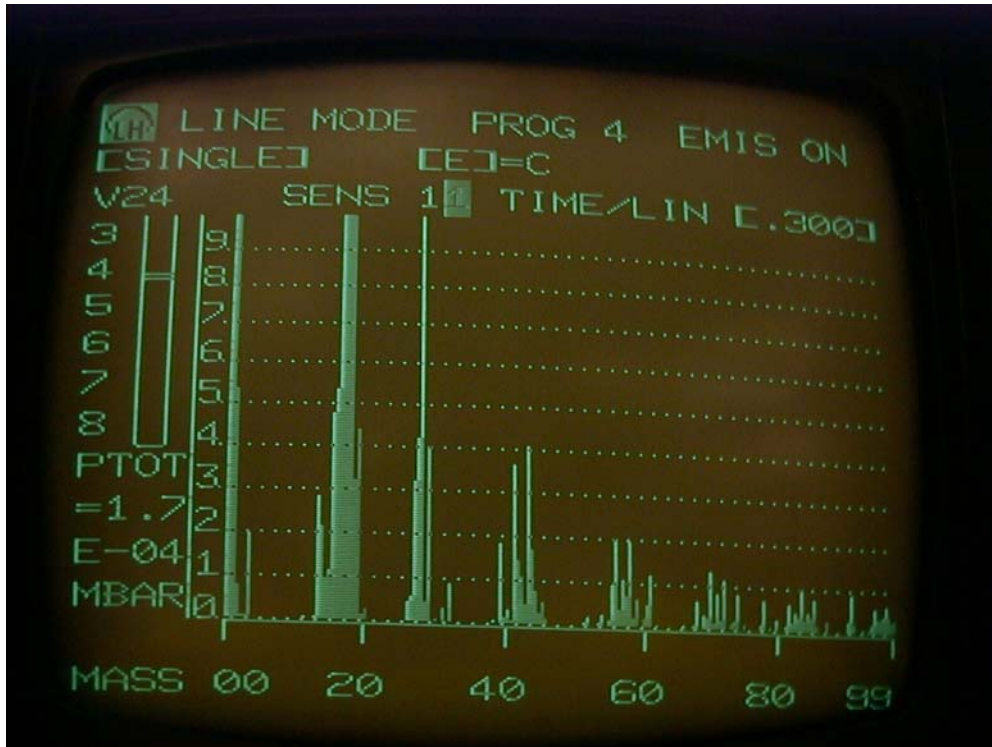


fig. 5-11 A rest gas analysis of a vacuum chamber directly attached to the roots blower pump. The plot shows the abundance of masses from 0 to 100 u with a sensitivity of 10^{-11} mbar. The base pressure in the chamber was $1.7 \cdot 10^{-4}$ mbar.

5.4 The planned setup

Before the entire FRS-Ion Catcher is ready to be tested with the high energy beams from the FRS, many off-line tests using a radioactive source will be performed in a very similar manner to the tests done at Argonne. Especially the compatibility of the new parts provided by GSI and other institutes will be tested. Once these checks are finished the whole setup has to be moved to the experimental area behind the FRS. How this setup will fit into the experimental area is shown in fig. 5-12.

The reason why the pumping line has to come from the top bridging almost the whole setup is due to space limitations behind the FRS. A design had to be found which does not only allow to fit together with the germanium γ -detectors of the RISING setup [RIS03] into area S4 behind the FRS, but also allows to quickly bring the system in and out in order to minimize the time between beam-times. The big advantage of this system is that everything can be assembled, aligned and tested at the off-line area. To do on-line runs one only has to bring in the three big pieces –roots pump, transfer-line and gas cell support table plus attached experimental setups via a crane through a hole in the roof of the S4 area. This minimizes the setup and therefore the shutdown time.

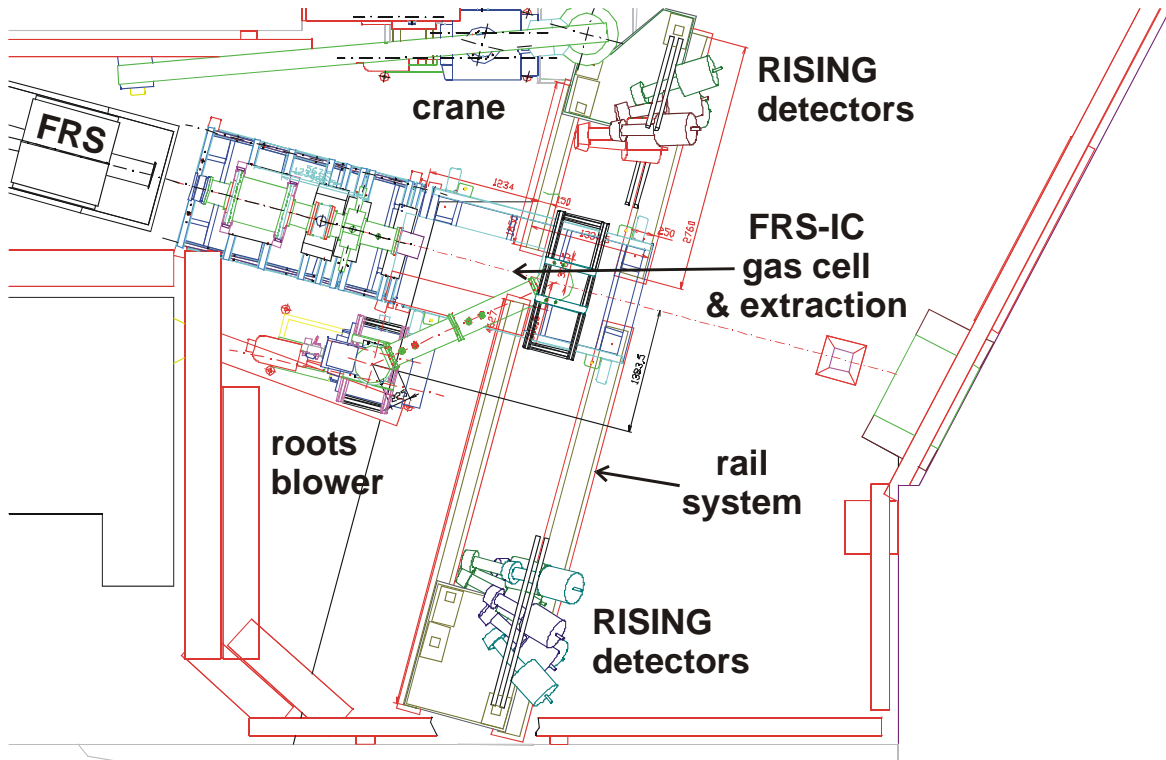


fig. 5-12 The S4 area behind the FRS. This is a possible scheme to fit the FRS-IC setup [FRS03] into the S4 area together with RISING [RIS03]. Behind the FRS there is one support table to place a MUSIC detector for identification and the degrader setup for range focusing. At the place where normally the RISING setup is placed the FRS-IC setup can be put in with the crane and beside the roots blower pumping station. For this the RISING detectors have to be moved apart on a rail system in the floor.

The complete FRS ion catcher setup will have a multi RFQ distributing the beam to three different experimental setups as shown in fig. 5-13.

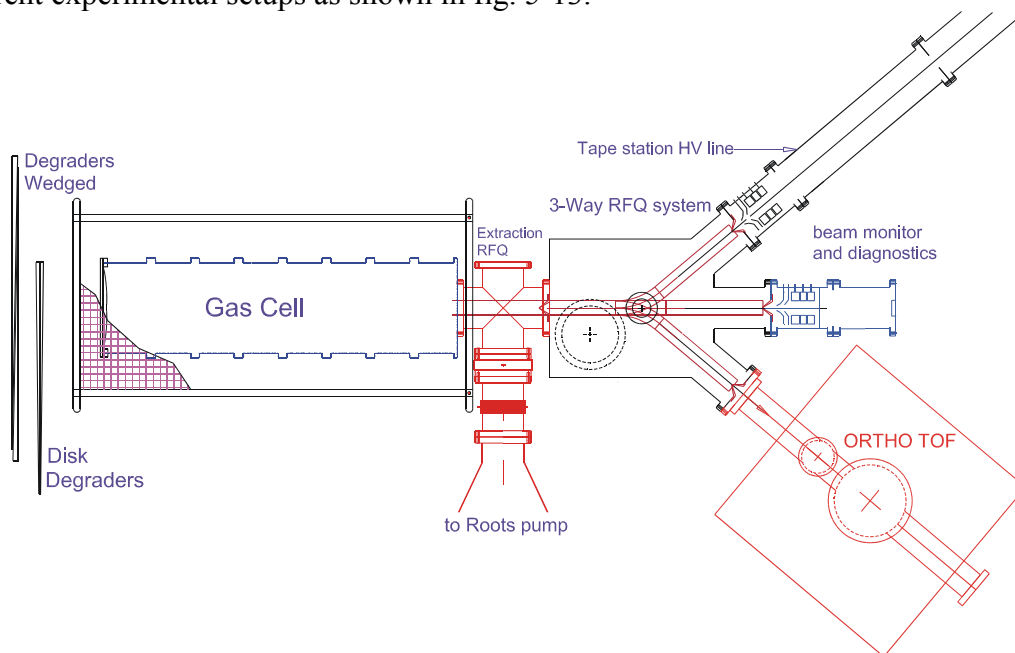


fig. 5-13 Schematic overview of the planned FRS ion catcher set up. After the degraders for range focusing the ions are stopped in the gas cell and extracted into the extraction RFQ. Behind this is a 3-way RFQ system which allows the ions to be distributed to three different experimental setups: a beam monitor and diagnostics section, a tape station for decay studies, and an orthogonal time of flight mass spectrometer (Ortho-TOF-MS).

The beam monitor and diagnostics section will be basically the same as the one used at Argonne for characterizing the cell and will be implanted first even before the development of the 3-way RFQ system.

The next step will be to couple the Ortho-TOF-MS delivered by the IONAS group at the University of Giessen to the system to perform precise mass measurements. (See fig. 5-14.)

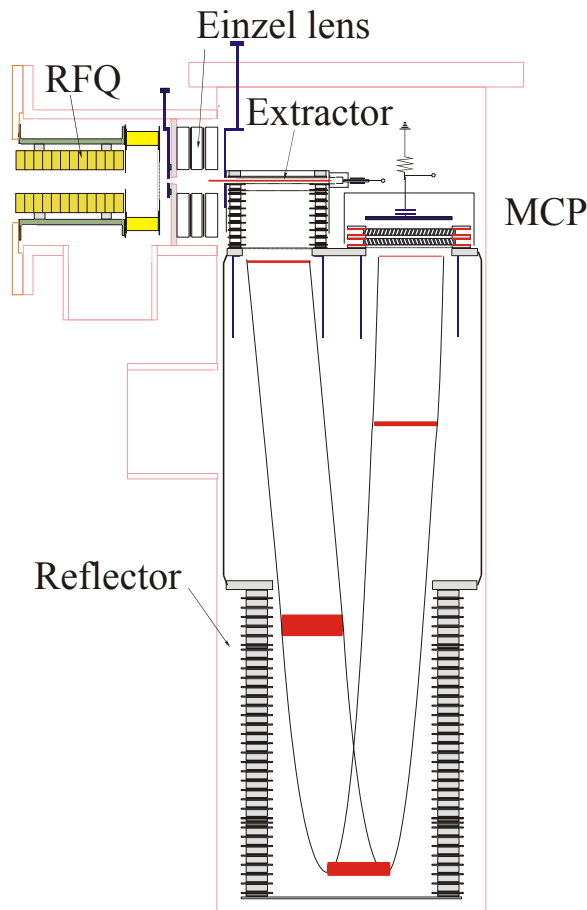


fig. 5-14 A schematic picture of the orthogonal time of flight mass spectrometer (Ortho-TOF-MS) developed at the JLU in Giessen.

The Ortho-TOF-MS consists of a buncher RFQ to cool and thermalize the ions. From there they are injected into the extractor region where they are accelerated in a perpendicular direction. At the bottom of the device the ions are deflected and end their parabolic flight by striking a MCP detector which determines their flight time.

Typically, a mass resolution (FWHM) of 20000 and a mass measurement accuracy of 1 *ppm* are achieved with the Ortho-TOF-MS. The duration of these measurement cycles is about 0.1 ms and is limited only by the time needed for the transfer of the ions and the cooling time.

The advantages of using this device with the FRS-Ion Catcher are that it gives access to short lived nuclei and already includes a gas filled RFQ device for bunching and cooling. Also, it is very compact and thus easy to fit into the strict space requirements of the FRS-Ion Catcher.

The tape station for decay studies of radioactive ion beams (See fig. 5-15.) behind the FRS will be delivered by a group at the university of Leuven.

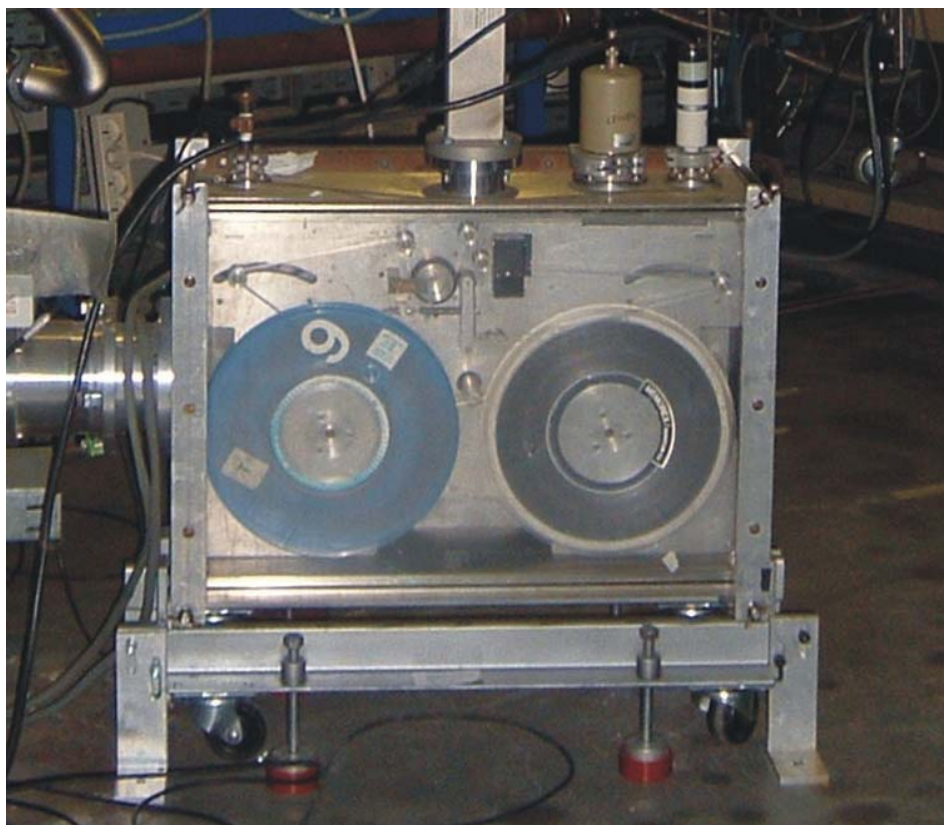


fig. 5-15 The foreseen tape station provided by KU Leuven for the decay studies.

6 Summary

The experiments presented in this work include charge-state distribution and stopping power measurements on Nickel and Xenon ions in the energy range from 500 MeV/u down to 30 MeV/u . Also a new method to reduce the momentum spread of in-flight separated Nickel and Cobalt fragments, the so called 'range focusing', was investigated. These experiments were performed in a couple of experimental runs at the fragment separator (FRS) at the Gesellschaft für Schwerionenforschung (GSI). And in parallel a device to thermalize, accumulate and distribute relativistic heavy ions, the FRS-Ion-Catcher was developed in an international collaboration.

- The charge-state distribution measurements were compared to the theoretical predictions of a charge parameterization by Pierce & Blann [PIB68] and the code GLOBAL [SCH98] based on the theoretical cross sections.

Above energies of 100 MeV/u the agreement with the simple Ansatz of P&B is already sufficient to predict the mean charge of Nickel with an accuracy of about 0.5% and 1% for Xenon.

For lower energies one has to use the theoretical cross sections used in GLOBAL to describe the measured charge-state distributions with the same accuracy. Still for Nickel ions on the high Z Materials Silver and Gold at energies below 50 MeV/u the deviations between measurement and the prediction are up to 1.6%. For the Xenon projectiles the deviations are even for the smallest measured energy of 40 MeV/u on Gold below 0.5%.

- The measured energy-loss and stopping powers of Nickel and Xenon ions were compared with the theoretical predictions of ATIMA [ATIMA], SRIM [ZIE85] and PASS [SIG02] as these simulation programs are based on different concepts.

The predictive power of ATIMA for energies above 100 MeV/u is better than 2% which is true for the other two codes as well. At lower energies already the theories start to differ for Nickel ions up to 5% and for Xenon ions even up to 10%. And thus the deviations from the experimental data is in the same order of magnitude.

While for the Xenon ions SRIM and PASS at least reproduce the general trend of the measured data, ATIMA drops back. This deviation was improved by including the measured charge-state distribution into the code ATIMA and partial integration of the stopping power up to a factor of two.

For the Nickel ions none of the theories shows the trend of the measured data correctly especially for the high Z materials. Also it was not possible to improve the situation by including the measured charge-state distribution, most likely because of the fewer charge states.

- The energy-straggling measurements on Nickel ions are unfortunately due to the quality of the used targets not sound. Even though the measurement agrees within the error bars for the high Z materials at high energies and the low Z materials at low energies there is also deviations up to a factor of 5. For the carbon targets it was possible to trace this down to a granularity effect in the material. Yet

altogether the error for this measurement is too large to judge on the quality of a theory.

- The range focusing technique was successfully employed on Ni and Co fragments and the measured range distributions fit very well to the predictions of simulation calculations. It was possible to reduce the initial range straggling of ^{56}Ni fragments from $\sigma_R = 55 \text{ mg/cm}^2$ by a factor 3.8 down to $\sigma_R = 14 \text{ mg/cm}^2$ very close to that of the ^{58}Ni primary beam which had $\sigma_R = 9 \text{ mg/cm}^2$. This experiment has proven the principle and feasibility of the range bunching technique and the mechanics used for the degrader systems. This essential feature will allow to stop relativistic heavy ions produced in fragmentation or fission reactions with large momentum spread more efficiently in thin layers of matter like foreseen for the FRS-Ion-Catcher [FRS03].
- In parallel to the experiments the FRS-IC [FRS03] setup, to thermalize, accumulate and distribute relativistic fragments for high precision experiments has been developed and build in an international collaboration of the Gesellschaft für Schwerionenforschung, the Justus-Liebig Universität Giessen, the Argonne National Laboratory, the Katholieke Universiteit Leuven, the Michigan State University and Riken. The FRS-IC will allow to stop the range-focused high-energy fragments in a noble gas stopper cell, distributing them cooled to high precision experimental setups. The assembly is currently tested at GSI with a ^{252}Cf source.

7 Zusammenfassung

In dieser Arbeit wurden die Ladungsverteilungen und Energieverluste von relativistischen Nickel- und Xenon-Ionen in Materie im Energiebereich von 30 MeV/u bis 500 MeV/u gemessen, und eine Methode untersucht, um die Impulsverteilung relativistischer Nickel- und Kobalt-Fragmente zu reduzieren, die so genannte „Reichweitenfokussierung“. Die Experimente wurden mit dem Magnetspektrometer FRS an der Gesellschaft für Schwerionenforschung (GSI) in mehreren Strahlzeiten durchgeführt.

- Um Vorhersagen über das Abbremsverhalten von Ionen zu machen ist es wichtig ihren Ladungszustand möglichst genau zu kennen, da das Bremsvermögen in etwa quadratisch vom Ladungszustand abhängt. Die gemessenen Ladungsverteilungen und die sich daraus ergebenden mittleren Landungen von Nickel und Xenon-Ionen wurden mit den theoretischen Vorhersagen der Ladungsparametrisierung von Pierce & Blann (P&B) [PIB68] und dem Computer Code GLOBAL [SCH98], basierend auf den theoretischen Querschnitten, verglichen.

Für Nickel wie Xenonionen zeigte sich, dass für Energien über 100 MeV/u ein simpler Ansatz wie P&B völlig ausreicht um die mittlere Ladung mit einer Genauigkeit von besser als 0.5% im Falle von Nickel Ionen und besser als 1% im Falle von Xenonionen vorhersagen zu können.

Die Messungen der Ladungsverteilung von Nickelionen im Energiebereich 30 bis 300 MeV/u zeigt eine gute Übereinstimmung mit den Vorhersagen von GLOBAL insbesondere auch bei Energien unter 100 MeV/u . Bei den Materialien mit niedrigem Z ergaben sich Abweichungen kleiner als 0.5%. Allerdings werden die Abweichungen für die Materialien mit hohem Z , also Silber und Gold bei Energien unter 50 MeV/u bis zu 1.6% groß.

Die Ladungsverteilungen der Xenonionen zeigen im Energiebereich 50 bis 500 MeV/u eine sehr gute Übereinstimmung mit der theoretischen Vorhersage von GLOBAL. Selbst bei der niedrigsten gemessenen Energie von 40 MeV/u und dem Target Material mit dem höchsten Z (Gold) bleiben die Abweichungen unter 0.5%.

- Die gemessenen Energieverluste der Nickel und Xenonionen wurden mit den theoretischen Vorhersagen von ATIMA [ATIMA], SRIM [ZIE85] und PASS [SIG02] verglichen da diese drei Theorien auf völlig verschiedenen Ansätzen beruhen.

Die Vorhersagekraft ATIMAs für die in diesem Experiment gemessenen Werte ist für Energien über 100 MeV/u besser als 2% wobei sich aber in diesem Energiebereich die Vorhersagen von PASS und SRIM im gleichen Bereich bewegen. Bei den Energien unter 100 MeV/u ergeben sich allerdings größere Abweichungen der Theorien untereinander und insbesondere vom Experiment. Schon die Theorien differieren für Nickelionen um 5% und bei Xenonionen sogar bis zu 10% voneinander. Ähnlich groß sind daher auch die Abweichungen zu den experimentellen Daten.

Während SRIM und PASS für die Xenonionen zumindest den generellen Trend der gemessenen Daten zeigen bleibt ATIMA deutlich hinter den Vorhersagen zurück.

Dies konnte durch die Berücksichtigung der gemessenen Ladungsverteilung und partielle Integration des Bremsvermögens um bis zu einen Faktor 2 verbessert werden.

Für die Nickelionen zeigt keine der drei Theorien den Trend der gemessenen Daten insbesondere für große Z und niedrige Energien unter 100 MeV/u . Außerdem ergab die partielle Integration des Bremsvermögens keine nennenswerte Verbesserung.

- Die Messungen der Energieverluststreuung von Nickelionen sind aufgrund der schlechten Targetqualität leider nicht aussagekräftig. Zwar stimmen die gemessenen Werte bei den Materialien mit niedrigem Z und niedrigen Energien sowie bei den Materialien mit hohem Z und hohen Energien innerhalb des Fehlers mit der theoretischen Vorhersage überein, aber es zeigen sich auch Abweichungen bis zu einem Faktor fünf welche sich zum Beispiel im Falle der Kohlenstofftargets auf eine Granularität des Targetmaterials zurückführen ließen. Insgesamt sind aber die Fehler dieser Messung zu groß um Aussagen über die Güte einer Theorie machen zu können.
- Um Präzisionsexperimente an gekühlten Projektilfragmenten durchführen zu können ist es notwendig die Energiebreite dieser Fragmente zu reduzieren um sie in dünnen Materieschichten abstoppen zu können. Um dies zu erreichen wurde eine dispersive Dipolstufe des Separators mit einem keilförmigen Abbremsler gekoppelt. Diese Technik, die Reichweitenfokussierung, wurde erfolgreich mit Ni- und Co-Fragmenten getestet und zeigt sehr gute Übereinstimmung mit den Simulationsrechnungen. So konnte zum Beispiel die anfängliche Reichweitenstreuung der ^{56}Ni Fragmente von $\sigma_R = 55 \text{ mg/cm}^2$ um einen Faktor 3.8 auf 14 mg/cm^2 reduziert werden. Dies ist sehr nahe an der Reichweitenstreuung des ^{58}Ni Primärstrahls mit gemessenem $\sigma_R = 9 \text{ mg/cm}^2$. Außerdem hat dieses Experiment gezeigt, dass die Technik der Reichweitenfokussierung entsprechend der Vorhersagen der Simulationsrechnung mit MOCADI [MOCADI] funktioniert.

Diese Technik erlaubt also eine drastische Reduzierung der Reichweitenstreuung von relativistischen Projektilfragmenten beim Abstoppen in dünnen Materie Schichten. Außerdem ist sie ein zentraler Baustein für zukünftige Niederenergie Experimente an exotischen Kernen wie zum Beispiel der FRS-Ion-Catcher [FRS03].

- Parallel zu den Experimenten wurde eine Anlage zum Abstoppen, Akkumulieren und Weiterleiten von relativistischen Schwerionen, der FRS-Ion-Catcher, entwickelt und in einer internationalen Kollaboration der Gesellschaft für Schwerionenforschung, der Justus-Liebig Universität Giessen, dem Argonne National Laboratory, der Katholieke Universiteit Leuven, der Michigan State University und Riken gebaut. Diese Anlage wird es in Zukunft erlauben die hochenergetischen, reichweitefokussierten Projektilfragmente in einer Edelgaszelle abzustoppen und gekühlt an Präzisionsexperimente zu verteilen. Zurzeit ist die Anlage unter Vakuum und wird mit einer ^{252}Cf Spaltquelle getestet.

8 Appendix

A: Target ladders

tab. 8-1 Overview of the three target ladders and the targets mounted for the slowing down experiment. Each ladder has 21 available positions and was completely removable from the beam. Two ladder had empty slots to measure the influence of the ladder structure itself .

Ladder/Position	Material	x [mg/cm ²]	Δx [mg/cm ²]
1.1	Al-81	81.21	1.23
1.2	Be-1199	1199.13	0.41
1.3	Be-20	19.76	0.38
1.4	Au-162	163.56	1.95
1.5	Be-100	100.46	0.28
1.6	Al-13	13.12	0.20
1.7	Be-215	215.33	1.52
1.8	Al-1205	1205.37	2.08
1.9	Cu-15	14.77	0.50
1.10	Cu-1010	1010.05	2.46
1.11	Al-254	253.61	0.59
1.12	Cu-152	160.79	2.16
1.13	Au-2	2.00	0.10
1.14	C-769	769.43	0.57
1.15	C-78	77.93	0.18
1.16	C-15	15.40	0.21
1.17	Au-945	944.93	28.93
1.18	Au-4026	4026.11	1.09
1.19	Au-20	18.34	0.75
1.20	Au-365	364.81	8.50
1.21	empty	0.00	0.00
2.1	Be-48	48.05	0.40
2.2	Cu-38	39.33	1.82
2.3	C-925	925.29	0.29
2.4	Au-41	48.26	1.05
2.5	C-473	472.65	0.24
2.6	Be-9.6	10.96	0.39
2.7	Be-448	448.08	1.29
2.8	Be-1798	1798.34	0.57
2.9	Al-1633	1632.99	1.52
2.10	Al-41	43.41	0.67
2.11	Al-521	520.68	0.56
2.12	Cu-1987	1986.57	2.92
2.13	Cu-76	79.60	1.01
2.14	Cu-440	440.09	0.63
2.15	C-151	150.69	0.17
2.16	C-23	23.00	0.18
2.17	Au-83	92.25	1.57
2.18	Au-5	9.29	1.14
2.19	Au-10	14.39	1.05
2.20	Au-582	581.53	4.92
2.21	Au-1667	1666.93	3.41

Ladder/Position	Material	x [mg/cm ²]	Δx [mg/cm ²]
3.1	Ag-4408	4407.77	3.93
3.2	Ag-2974	2973.90	2.36
3.3	Ag-2215	2215.03	2.70
3.4	Ag-1431	1431.49	2.81
3.5	Ag-637	637.06	1.31
3.6	Ag-450	450.25	1.53
3.7	Ag-317	316.76	1.41
3.8	Ag-175	175.71	1.32
3.9	Ag-120	138.42	7.96
3.10	Ag-88	95.30	3.25
3.11	Ag-45	49.49	1.03
3.12	Ag-19	21.66	0.60
3.13	empty	0.00	0.00
3.14	C	0,403	<5%
3.15	Ag	0,095	<5%
3.16	Ni	0,415	<5%
3.17	Ni	0,230	<5%
3.18	Al	0,390	<5%
3.19	Al	0,055	<5%
3.20	Au	0,375	<5%
3.21	Au	0,080	<5%

B: Data tables

In here all measured values, charge state distributions, energy losses, stopping powers, and ^{136}Xe primary beams, the energy straggling data for the ^{58}Ni beam and the range focusing of ^{56}Ni and ^{54}Co fragments are summarized in data tables.

Charge-state distributions

tab. 8-2 Measured charge-state distribution and mean charge of ^{58}Ni projectiles for all measured energy and target combinations. Shown is for the incident energy E_{in} and after the target E_{out} the proton number Z of the target the abundance of each charge state and the mean charge.

E_{in}	E_{out}	Z_2	$q=28+$	$q=27+$	$q=26+$	$q=25+$	\bar{q}
300	220.2	6	0.9982 (0.0003)	0.0177 (0.0003)			27.998 (0.0004)
300	201.1	47	0.9884 (0.0001)	0.0116 (0.0007)			27.9884 (0.0008)
300	284.5	79	0.996 (0.0001)	0.004 (0.0002)			27.996 (0.0002)
300	227.8	79	0.9906 (0.0001)	0.0094 (0.0007)			27.9906 (0.0008)
100	94.4	4	0.9926 (0.0001)	0.0074 (0.0008)			27.9926 (0.0011)
100	90.9	4	0.9925 (0.0001)	0.0075 (0.0009)			27.9925 (0.001)
100	80.6	4	0.9901 (0.0001)	0.0099 (0.0007)			27.9901 (0.0009)
100	96.3	6	0.9947 (0.0001)	0.0053 (0.0003)			27.9947 (0.0001)
100	92.8	6	0.9932 (0.0001)	0.0068 (0.0007)			27.9932 (0.0004)
100	86.2	6	0.9918 (0.0001)	0.0082 (0.001)			27.9918 (0.0002)
100	78.4	6	0.991 (0.0001)	0.009 (0.0009)			27.991 (0.0008)
100	95.7	13	0.9859 (0.0001)	0.0141 (0.001)			27.9859 (0.0011)
100	90.3	13	0.9815 (0.0002)	0.0185 (0.0012)			27.9815 (0.0008)
100	78.6	13	0.9687 (0.0003)	0.0313 (0.0019)			27.9687 (0.0012)
100	74.7	13	0.9683 (0.0003)	0.0317 (0.0017)			27.9683 (0.0014)
100	94.9	29	0.9417 (0.0006)	0.0583 (0.0025)			27.9417 (0.0025)

E_{in}	E_{out}	Z_2	$q=28+$	$q=27+$	$q=26+$	$q=25+$	\bar{q}
100	89.7	29	0.9301 (0.0008)	0.0699 (0.0028)			27.9301 (0.0024)
100	84.2	29	0.9205 (0.0012)	0.0795 (0.0039)			27.9205 (0.0033)
100	67.1	29	0.8593 (0.0029)	0.1407 (0.0071)			27.8593 (0.0041)
100	94.6	47	0.922 (0.0014)	0.078 (0.0047)			27.922 (0.0051)
100	89.3	47	0.9134 (0.0011)	0.0866 (0.0036)			27.9134 (0.0093)
100	79.9	47	0.8961 (0.0018)	0.1039 (0.0052)			27.8961 (0.0064)
100	70.4	47	0.8571 (0.0024)	0.1357 (0.0058)	0.0072 (0.0039)		27.8499 (0.0053)
100	94.6	79	0.9028 (0.0009)	0.0972 (0.0028)			27.9028 (0.0069)
100	89.3	79	0.8906 (0.0018)	0.1094 (0.0052)			27.8906 (0.0151)
100	80.3	79	0.8647 (0.0026)	0.1353 (0.0066)			27.8647 (0.004)
100	67.3	79	0.7768 (0.0056)	0.2069 (0.0103)	0.0163 (0.0083)		27.7605 (0.0084)
70	64.9	4	0.9865 (0.0001)	0.0135 (0.0009)			27.9865 (0.001)
70	59	4	0.9859 (0.0001)	0.0141 (0.0009)			27.9859 (0.0011)
70	53.2	4	0.9808 (0.0002)	0.0192 (0.0012)			27.9808 (0.0013)
70	65.4	6	0.988 (0.0001)	0.012 (0.0007)			27.988 (0.0008)
70	57.5	6	0.9824 (0.0001)	0.0176 (0.0006)			27.9824 (0.0006)
70	51.2	6	0.9753 (0.0001)	0.0247 (0.0009)			27.9753 (0.001)
70	65.8	13	0.9509 (0.0004)	0.0491 (0.0016)			27.9509 (0.002)
70	61.8	13	0.9404 (0.0003)	0.0596 (0.001)			27.9404 (0.0013)
70	57.1	13	0.9282 (0.0005)	0.0718 (0.002)			27.9282 (0.0025)
70	65.4	29	0.8383 (0.0012)	0.1617 (0.0027)			27.8383 (0.0039)
70	62	29	0.8177 (0.0013)	0.1722 (0.0028)	0.0102 (0.0011)		27.8075 (0.0062)

E_{in}	E_{out}	Z_2	$q=28+$	$q=27+$	$q=26+$	$q=25+$	\bar{q}
70	52.7	29	0.7233 (0.0021)	0.2531 (0.0033)	0.0236 (0.0024)		27.6997 (0.0095)
70	66.6	47	0.8226 (0.0011)	0.1657 (0.0024)	0.0117 (0.0009)		27.8109 (0.0052)
70	60.2	47	0.7902 (0.0012)	0.1962 (0.0024)	0.0135 (0.0008)		27.7767 (0.0051)
70	56	47	0.7595 (0.0014)	0.2206 (0.0025)	0.0199 (0.0014)		27.7395 (0.0064)
70	64.6	79	0.737 (0.0017)	0.238 (0.0028)	0.025 (0.0009)		27.712 (0.0061)
70	59.3	79	0.7099 (0.0022)	0.2633 (0.0034)	0.0268 (0.0013)		27.6831 (0.0078)
70	53.2	79	0.6328 (0.003)	0.3186 (0.004)	0.0486 (0.0023)		27.5841 (0.0107)
50	47.3	4	0.9763 (0.0003)	0.0237 (0.0017)			27.9763 (0.002)
50	45.9	4	0.9752 (0.0003)	0.0248 (0.0017)			27.9752 (0.002)
50	40.3	4	0.9681 (0.0003)	0.0315 (0.0018)	0.0004 (0.0003)		27.9677 (0.0028)
50	46.2	6	0.9691 (0.0003)	0.0306 (0.0018)	0.0004 (0.0002)		27.9687 (0.0025)
50	43.9	6	0.9646 (0.0005)	0.0354 (0.0024)			27.9646 (0.0028)
50	44.5	13	0.8477 (0.0018)	0.1435 (0.0041)	0.0087 (0.0015)		27.839 (0.0086)
50	42.6	13	0.83 (0.0022)	0.162 (0.0049)	0.0079 (0.0025)		27.8221 (0.0116)
50	45.9	29	0.6368 (0.003)	0.3171 (0.004)	0.0461 (0.002)		27.5907 (0.0101)
50	44.2	29	0.6163 (0.0032)	0.3348 (0.0041)	0.0488 (0.0028)		27.5675 (0.0117)
50	41.5	29	0.5822 (0.0041)	0.3585 (0.0049)	0.0579 (0.0037)	0.0014 (0.0008)	27.5216 (0.0166)
50	48.2	47	0.6571 (0.0032)	0.3016 (0.0044)	0.0414 (0.0035)		27.6157 (0.0133)
50	45.6	47	0.6188 (0.0043)	0.3315 (0.0056)	0.0498 (0.0049)		27.569 (0.0177)
50	41	47	0.5603 (0.0043)	0.3687 (0.005)	0.068 (0.0035)	0.0031 (0.0014)	27.4862 (0.0178)
50	45	79	0.5044 (0.0059)	0.398 (0.0064)	0.0928 (0.0054)	0.0047 (0.0026)	27.4022 (0.0261)
50	41.3	79	0.4224 (0.0072)	0.4358 (0.0072)	0.1329 (0.007)	0.0089 (0.0028)	27.2717 (0.0293)

tab. 8-3 Measured charge-state distribution and mean charge of ^{136}Xe projectiles for all measured energy and target combinations. Shown is for the incident energy E_{in} and after the target E_{out} the proton number Z of the target the abundance of each charge state and the mean charge.

E_{in}	E_{out}	Z_2	$q=54+$	$q=53+$	$q=52+$	$q=51+$	$q=50+$	$q=49+$	\bar{q}
500	439	4	0.9385 (0.0004)	0.0602 (0.0015)	0.0013 (0.0002)				53.9372 (0.0024)
500	401.8	4	0.9287 (0.0004)	0.0697 (0.0015)	0.0016 (0.0002)				53.9271 (0.0024)
500	339.7	4	0.9027 (0.0005)	0.0945 (0.0016)	0.0028 (0.0003)				53.9 (0.0027)
500	474	6	0.9657 (0.0004)	0.0337 (0.0021)	0.0005 (0.0003)				53.9652 (0.003)
500	447.7	6	0.9536 (0.0003)	0.0459 (0.0011)	0.0006 (0.0001)				53.953 (0.0017)
500	403.7	6	0.9478 (0.0003)	0.0517 (0.0015)	0.0006 (0.0002)				53.9472 (0.0021)
500	461.7	13	0.9783 (0.0001)	0.0216 (0.0008)	0.0001 (0.0001)				53.9782 (0.001)
500	413.3	13	0.9734 (0.0002)	0.0263 (0.0009)	0.0002 (0.0001)				53.9732 (0.0013)
500	352.1	13	0.9644 (0.0002)	0.0356 (0.0012)	0.0001 (0.0001)				53.9643 (0.0015)
500	454.6	29	0.9812 (0.0001)	0.0187 (0.0009)	0.0001 (0.0001)				53.9811 (0.0011)
500	413.2	29	0.9759 (0.0001)	0.024 (0.0007)	0.0002 (0.0001)				53.9757 (0.0009)
500	364.5	29	0.9671 (0.0002)	0.0328 (0.001)	0.0001 (0.0001)				53.9669 (0.0014)
500	443.2	47	0.967 (0.0002)	0.0328 (0.0009)	0.0002 (0.0001)				53.9668 (0.0013)
500	410.9	47	0.9585 (0.0002)	0.041 (0.0011)	0.0004 (0.0001)				53.9581 (0.0015)
500	378.5	47	0.947 (0.0003)	0.0525 (0.0013)	0.0005 (0.0001)				53.9465 (0.0018)
500	447.9	79	0.9517 (0.0003)	0.0475 (0.0011)	0.0008 (0.0002)				53.9509 (0.0017)
500	409.4	79	0.9351 (0.0003)	0.0639 (0.0013)	0.001 (0.0002)				53.9341 (0.002)
500	353.8	79	0.9137 (0.0004)	0.0841 (0.0013)	0.0022 (0.0002)				53.9115 (0.0021)
300	271.2	4	0.8619 (0.0007)	0.1342 (0.0017)	0.0039 (0.0003)				53.858 (0.003)

E_{in}	E_{out}	Z_2	$q=54+$	$q=53+$	$q=52+$	$q=51+$	$q=50+$	$q=49+$	\bar{q}
300	256.8	4	0.861 (0.0009)	0.1336 (0.0022)	0.0055 (0.0005)				53.8555 (0.0041)
300	256.8	4	0.8521 (0.0007)	0.1432 (0.0016)	0.0048 (0.0003)				53.8473 (0.003)
300	215.2	4	0.8231 (0.0013)	0.1678 (0.0028)	0.0091 (0.0008)				53.8139 (0.0056)
300	215.2	4	0.8107 (0.0009)	0.1799 (0.0019)	0.0094 (0.0005)				53.8014 (0.0038)
300	284	6	0.9034 (0.0005)	0.0943 (0.0016)	0.0023 (0.0003)				53.901 (0.0026)
300	260.7	6	0.8934 (0.0005)	0.1039 (0.0015)	0.0027 (0.0003)				53.8907 (0.0026)
300	225.9	6	0.8755 (0.0004)	0.1207 (0.0011)	0.0038 (0.0002)				53.8718 (0.0019)
300	281.7	13	0.9412 (0.0002)	0.0581 (0.0009)	0.0007 (0.0001)	0.00003 (0.00002)			53.9404 (0.0014)
300	250.6	13	0.9278 (0.0003)	0.0712 (0.0011)	0.001 (0.0001)				53.9267 (0.0017)
300	217.8	13	0.9111 (0.0004)	0.087 (0.0011)	0.0018 (0.0002)				53.9093 (0.0018)
300	276.1	29	0.9177 (0.0002)	0.0806 (0.0007)	0.0016 (0.0001)				53.9161 (0.0012)
300	243.5	29	0.8843 (0.0003)	0.1122 (0.0009)	0.0034 (0.0002)				53.8809 (0.0015)
300	216.7	29	0.838 (0.0005)	0.1552 (0.0011)	0.0068 (0.0003)				53.8312 (0.0021)
300	277.9	47	0.8545 (0.0004)	0.1402 (0.001)	0.0053 (0.0002)				53.8491 (0.0019)
300	268.4	47	0.8424 (0.0005)	0.1514 (0.0011)	0.0062 (0.0003)				53.8362 (0.0021)
300	226.2	47	0.7601 (0.0008)	0.2241 (0.0014)	0.0158 (0.0005)				53.7443 (0.0031)
300	275.5	79	0.8153 (0.0006)	0.1748 (0.0013)	0.0099 (0.0004)				53.8054 (0.0026)
300	255.9	79	0.7831 (0.0007)	0.2024 (0.0014)	0.0145 (0.0005)				53.7687 (0.0029)
300	218.8	79	0.6971 (0.0012)	0.2762 (0.0018)	0.0262 (0.0007)	0.0005 (0.0001)			53.6698 (0.0045)
100	91.4	4	0.4934 (0.0042)	0.4216 (0.0044)	0.0843 (0.0031)	0.0007 (0.0003)			53.408 (0.014)
100	80.7	4	0.446 (0.0032)	0.4483 (0.0032)	0.1038 (0.0025)	0.0018 (0.0004)			53.34 (0.01)

E_{in}	E_{out}	Z_2	$q=54+$	$q=53+$	$q=52+$	$q=51+$	$q=50+$	$q=49+$	\bar{q}
100	69.1	4	0.3539 (0.0033)	0.4919 (0.0031)	0.1513 (0.0029)	0.0029 (0.0005)			53.197 (0.011)
100	94.6	6	0.5674 (0.0025)	0.3778 (0.0029)	0.0542 (0.0017)	0.0006 (0.0002)			53.512 (0.0078)
100	85.5	6	0.5555 (0.0035)	0.383 (0.0041)	0.0604 (0.0025)	0.001 (0.0003)			53.4931 (0.012)
100	76.1	6	0.5041 (0.004)	0.4135 (0.0043)	0.0797 (0.003)	0.0027 (0.0006)			53.419 (0.014)
100	93.2	13	0.4724 (0.004)	0.4188 (0.0042)	0.1037 (0.0032)	0.0051 (0.0008)			53.359 (0.014)
100	84.9	13	0.3826 (0.0039)	0.4594 (0.0038)	0.1502 (0.0034)	0.0078 (0.0009)			53.217 (0.014)
100	66.2	13	0.1618 (0.0033)	0.4374 (0.0036)	0.362 (0.0037)	0.0388 (0.0018)			52.722 (0.016)
100	92.2	29	0.1841 (0.0028)	0.4484 (0.0029)	0.3231 (0.0031)	0.043 (0.0016)	0.0014 (0.0003)		52.771 (0.013)
100	84.2	29	0.1346 (0.0029)	0.4196 (0.0035)	0.3628 (0.0035)	0.0782 (0.0024)	0.0046 (0.0006)	0.0003 (0.0001)	52.601 (0.017)
100	75.7	29	0.0819 (0.0027)	0.3545 (0.004)	0.4263 (0.0039)	0.1247 (0.0032)	0.0116 (0.0011)	0.0009 (0.0003)	52.36 (0.02)
100	91.8	47	0.101 (0.0021)	0.4058 (0.0028)	0.4021 (0.0028)	0.0851 (0.002)	0.0058 (0.0006)	0.0003 (0.0001)	52.510 (0.013)
100	83.9	47	0.0686 (0.0018)	0.3547 (0.0028)	0.4607 (0.0026)	0.1072 (0.0021)	0.0082 (0.0006)	0.0006 (0.0002)	52.366 (0.025)
100	69.3	47	0.0304 (0.0013)	0.2246 (0.0028)	0.5191 (0.0026)	0.1958 (0.0027)	0.0275 (0.0012)	0.0025 (0.0004)	52.027 (0.013)
100	91.9	79	0.0833 (0.0018)	0.361 (0.0026)	0.4237 (0.0026)	0.1188 (0.0021)	0.0122 (0.0007)	0.0009 (0.0002)	52.382 (0.012)
100	84.1	79	0.0555 (0.0024)	0.3102 (0.0042)	0.4846 (0.0039)	0.1247 (0.0034)	0.0227 (0.0016)	0.0022 (0.0005)	52.245 (0.021)
100	70.1	79	0.0255 (0.0016)	0.1521 (0.0034)	0.5214 (0.0035)	0.248 (0.0038)	0.0514 (0.0022)	0.0016 (0.0004)	51.85 (0.02)
70	65.5	4	0.2183 (0.0024)	0.4956 (0.0023)	0.2791 (0.0025)	0.007 (0.0005)			52.9252 (0.0078)
70	59.5	4	0.2743 (0.0018)	0.4862 (0.0017)	0.2323 (0.0018)	0.0072 (0.0004)			53.0277 (0.0057)
70	52.5	4	0.2205 (0.0025)	0.4641 (0.0025)	0.3029 (0.0026)	0.0126 (0.0008)			52.8924 (0.0089)
70	63.7	6	0.3387 (0.0018)	0.476 (0.0016)	0.1803 (0.0016)	0.0051 (0.0003)			53.1482 (0.0056)
70	56.6	6	0.2682 (0.0024)	0.4883 (0.0022)	0.2435 (0.0023)				53.0247 (0.0065)

E_{in}	E_{out}	Z_2	$q=54+$	$q=53+$	$q=52+$	$q=51+$	$q=50+$	$q=49+$	\bar{q}
70	52.4	6	0.204 (0.0021)	0.4722 (0.0021)	0.3238 (0.0022)				52.8802 (0.0063)
70	64.1	13	0.1337 (0.0021)	0.4133 (0.0025)	0.397 (0.0025)	0.0559 (0.0015)			52.6248 (0.0099)
70	58.1	13	0.0775 (0.0012)	0.3382 (0.0018)	0.4767 (0.0017)	0.0996 (0.0013)	0.0079 (0.0004)		52.3778 (0.0082)
70	51.5	13	0.0334 (0.0012)	0.2258 (0.0026)	0.5399 (0.0024)	0.1804 (0.0024)	0.0205 (0.001)		52.071 (0.011)
70	63.5	29	0.0313 (0.0011)	0.2222 (0.0024)	0.502 (0.0023)	0.2105 (0.0024)	0.0339 (0.0012)		52.0065 (0.011)
70	58.6	29	0.0218 (0.0008)	0.1721 (0.0019)	0.5024 (0.0019)	0.2583 (0.002)	0.0453 (0.0011)		51.8668 (0.0093)
70	50.2	29	0.0104 (0.0006)	0.0939 (0.0017)	0.4505 (0.0023)	0.3503 (0.0024)	0.0948 (0.0017)		51.5749 (0.011)
70	65.1	47	0.0201 (0.0009)	0.17 (0.0023)	0.5506 (0.0022)	0.2211 (0.0025)	0.0381 (0.0013)		51.9129 (0.0108)
70	56.4	47	0.01 (0.0007)	0.085 (0.0019)	0.5105 (0.0025)	0.3202 (0.0027)	0.0743 (0.0018)		51.6363 (0.012)
70	49.5	47	0.0054 (0.0005)	0.0519 (0.0015)	0.4406 (0.0026)	0.3879 (0.0027)	0.1142 (0.0021)		51.4464 (0.0117)
70	64.4	79	0.0089 (0.0007)	0.1081 (0.0022)	0.4828 (0.0027)	0.3153 (0.0028)	0.0848 (0.002)		51.6409 (0.013)
70	60.5	79	()	0.082 (0.0018)	0.457 (0.0025)	0.3536 (0.0026)	0.1074 (0.002)		51.514 (0.011)
70	54.7	79	()	0.0444 (0.0014)	0.3928 (0.0027)	0.4073 (0.0027)	0.1555 (0.0024)		51.326 (0.011)

Stopping power

tab. 8-4 Measured stopping powers of ^{58}Ni and ^{136}Xe on various target materials Z_2 .

Z_1	Z_2	E [MeV/u]	$-dE/dx$ [MeV/(mg/cm ²)]	$\Delta(dE/dx)$
28	4	46	8.12	0.10
28	4	62	6.54	0.07
28	4	92	5.01	0.07
28	4	261	2.48	0.02
28	6	47	9.30	0.16
28	6	61	7.08	0.06
28	6	91	5.37	0.04
28	6	260	2.74	0.02
28	13	46	7.49	0.12
28	13	64	6.04	0.11
28	13	88	4.97	0.03
28	13	264	2.41	0.01
28	29	45	6.14	0.11
28	29	66	4.94	0.16
28	29	88	4.23	0.02
28	29	268	2.05	0.01
28	47	46	5.28	0.12
28	47	64	4.63	0.06
28	47	87	3.78	0.02
28	47	251	1.92	0.01
28	79	46	4.42	0.09
28	79	62	3.87	0.06
28	79	87	3.18	0.03
28	79	268	1.59	0.02
54	4	61	24.30	0.78
54	4	87	17.25	0.58
54	4	261	9.26	0.13
54	4	421	7.30	0.06
54	6	60	25.83	0.84
54	6	90	19.30	0.97
54	6	267	10.13	0.17
54	6	457	7.81	0.09
54	13	60	23.01	0.66
54	13	87	17.69	0.26
54	13	262	9.16	0.13
54	13	433	7.10	0.06
54	29	60	19.12	0.54
54	29	88	14.47	0.22
54	29	259	8.00	0.11
54	29	433	6.22	0.06
54	47	60	17.12	0.45
54	47	87	12.67	0.26

Z_1	Z_2	E [MeV/u]	$-dE/dx$ [MeV/(mg/cm ²)]	$\Delta(dE/dx)$
54	47	434	5.60	0.05
54	79	62	14.16	0.47
54	79	87	10.56	0.18
54	79	262	6.12	0.10
54	79	428	4.85	0.04

Range focusing

tab. 8-5 Measured range distribution of a ⁵⁸Ni primary beam, ⁵⁶Ni and ⁵⁴Co fragments, depending on the degrader angle.

Fragment	Degrader angle α [mrad]	Range distribution σ_R [mg/cm ²]
⁵⁸ Ni primary	- 4.8 (5)	9 (1)
⁵⁶ Ni	- 4.8 (5)	55 (4)
⁵⁶ Ni	6.2 (5)	14 (1)
⁵⁶ Ni	17.7 (5)	38 (2)
⁵⁴ Co	- 4.8 (5)	85 (25)
⁵⁴ Co	6.2 (5)	17 (2)

References

- [AHL78] S.P. Ahlen, Phys. Rev. **17** (1978) 1236.
- [AHL80] S.P. Ahlen, Rev. Mod. Phys. **52** (1980) 121.
- [AHL82] S.P. Ahlen, Phys. Rev. **A 25** (1982) 1856.
- [ANM85] R. Anholt, W.E. Meyerhof et al., Phys.Rev.A32 (1985) 3302.
- [ARM95] P. Armbruster, et al., Z. Phys. **A** (1995).
- [ATIMA] <http://www-aix.gsi.de/~weick/atima/> ATIMA homepage.
- [BAB64] W.H. Barkas, M.J. Berger, NASA Report **SP-3013** (1964).
- [BAH69] Bahr, R.; Gerlich, D.; Teloy, E. *E Verhandl. DPG (VI)* (1969).
- [BER88] C.A. Bertulani, G. Baur, Phys. Rep. (1988) 163-299.
- [BET32] H. Bethe, Z. Phys. **76** (1932) 293.
- [BET77] H.A. Bethe, E.E. Salpeter, *Quantum Mechanics of One- and Two-Electron Atoms*, Plenum Press, New York, (1977).
- [BEY03] G.J. Beyer et al., Nuclear Instruments and Methods **B 204** (2003) 225.
- [BLO33] F. Bloch, *Zur Bremsung rasch bewegter Teilchen beim Durchgang durch Materie*, Ann. Phys. (Leipzig) **16** (1933).
- [BOH13] N. Bohr, Phil. Mag. (6) **25** (1913) 10.
- [BOH15] N. Bohr, Phil. Mag. (6) **30** (1915) 581.
- [BOH48] N. Bohr, Dan. Mat. Fys. Medd. **18 No.8** (1948).
- [BoW39] N.Bohr, J.A.Wheeler, *The Mechanism of Nuclear Fission*, Physical Review **56** (1939) 426.
- [BRA82] W. Brand, M. Kitigawa, Phys. Rev. **B 25** (1982) 5631.
- [BRO89] Brosa Formel, Nucl. Phys. **A 505** (1989) 423C, 190402 HWE.
- [CDR01] http://www.gsi.de/GSI-Future/cdr/PDF/S2_Kap1.pdf
Conceptual Design Report, Sec.2, chapter 1.1.3.4
- [CHI03] V. Chichkine, Dissertation, II Physikalisches Institut, Justus Liebig Universität Giessen (2003).
- [CIR97] <http://www-aix.gsi.de/~bio/RESEARCH/therapy.html> Homepage of the “Carbon ion therapy at GSI”.
- [DAL60] A. Dalgarno, Proc. Phys. Soc. **A76**, (1960) 422.
- [DAW76] P.H. Dawson, *Quadrupole Mass Spectroscopy and its Applications*, Elsevier Scientific Publishing Company, New York (1976).
- [ECC95] <http://environmentalchemistry.com/yogi/periodic/> Data tables on the chemical elements.

- [EIM95] J. Eichler, W.E. Meyerhof, *Relativistic Atomic Collisions*, Academic Press (1995).
- [ENG67] H.A. Enge, *Nuclear Instruments and Methods* **49**, (1967) 181.
- [FER40] E. Fermi, The ionisation loss of energy in gases and in condensed materials, *Phys. Rev.* **57** (1940) 485.
- [FIR57] O.B. Firsov, *Sov. Phys. JETP* **5** (1957) 1192.
- [FRS03] <http://www-wnt.gsi.de/s258/main.htm> FRS ion catcher homepage.
- [GAS91] J.-J. Gaimard, K.-H. Schmidt, *Nucl. Phys.* **A531** (1991) 709.
- [GEI89] H.Geissel et al., *NIM A* **282** (1989) 247.
- [GEI92] H.Geissel et al., *NIM B* **70** (1992) 286.
- [GEI03] H. Geissel et al., *NIM B* **204** (2003) 71.
- [GICO] <http://www-aix.gsi.de/~weick/gico/> GICO Manual.
- [GOL74] A.S. Goldhaber, *Phys. Lett.* **53 B** (1974) 306.
- [GRE85] D.E. Greiner, H. Crawford, P.J. Lindstrom, J.M. Kidd, D.L. Olson, T.J.M. Symons, *Phys. Rev.* **C 31** (1985) 416.
- [HAS39] O. Hahn, F. Strassmann, *Über den Nachweis und das Verhalten der bei Bestrahlung des Urans mittels Neutronen entstehenden Erdalkalimetalle*, *Naturwissenschaften* **27** (1939) 11.
- [HOF00] S. Hofmann and G. Münzenberg, *Rev. Mod. Phys.* **72** (2000) 733 and ref. herein.
- [HUB80] F. Hubert, A. Fleury, R. Bimbot, Gardes, *Ann. Phys. (France)* **5 S** (1980) 1.
- [HUB90] F. Hubert, R. Bimbot, H. Gauvin, *Atom. Data and Nucl. Data Tables* **46** (1990) 1.
- [HVE71] P. Hvelplund, *Dan. Mat. Fys. Medd. Dan. Vid. Selsk.* **38 no.4** (1971).
- [ICR94] International Commission on Radiation Units and Measurements, *Stopping Powers and Ranges for Protons and Alpha Particles*, ICRU-Report No.49, Bethesda, Maryland (1994).
- [ICA03] <http://www.ha.physik.uni-muenchen.de/ioncatcher/> Homepage of the RTD project Ion catcher.
- [ICH94] A. Ichihara, T. Shirai, J. Eichler, *Phys. Rev.* **A 49** (1994) 1875.
- [IKG95] A.V. Ignatyuk, G.A. Kudyayev, A. Junghans, M. de Jong, H.-G. Clerc, K.-H. Schmidt, *Nucl. Phys.* **A593** (1995) 519.
- [IWA97] N. Iwasa et al., *NIM B* **126** (1997) 284.
- [JAC72] J.D. Jackson, R.L. Mc Carthy, *Phys. Rev.* **B 6** (1972) 4131.
- [JAC75] J.D. Jackson, *Classical Electrodynamics*, 2nd edition, John Wiley, New York (1975).
- [KOX87] S. Kox et al., *Phys. Rev.* **C 35** (1987) 1678.

- [Kra88] K.S. Krane, Introductory NUCLEAR PHYSICS, John Wiley & Sons (1988).
- [KRA88] G. Kraft et al., Proc. of the EULIMA Workshop, Nice (1988).
- [LET98] J. Lettry et al., Review of Scientific Instruments **69** (2) (1998) 761.
- [LIN68] J. Lindhard, V. Nielsen, M. Scharff, Dan. Mat. Fys. Medd. **36** (1968) 10.
- [LIN72] J. Lindhard, Nuclear Instruments and Methods **132** (1976)1.
- [LIN96] J. Lindhard, A.H. Sørensen, Phys. Rev. **A 53** (1996) 2443.
- [LIS02] D. Bazin et al., Nuclear Instruments and Methods **A 482** (2002) 307.
- [LIS03] <http://groups.nsl.msu.edu/lise/> Homepage of LISE++, a simulation package for fragment separators.
- [Mei39] L. Meitner, O.R. Frisch, Disintegration of uranium by neutrons: a new type of nuclear reaction, Nature **143** (1939) 239.
- [MIC00] „Abbremsen, Einfangen und Kühlen von radioaktiven Spaltfragmenten in einer Ionenfallenanlage“, Diplomarbeit, Michael Maier, Ruprecht-Karls-Universität Heidelberg (2000).
- [MOCADI] <http://www-linux.gsi.de/~weick/mocadi/> Monte Carlo simulation program to calculate the transport of projectiles through ion optical systems.
- [NOR60] L.C. Northcliffe, Phys. Rev. **120** (1960) 1744.
- [PAU03] <http://www.exphys.uni-linz.ac.at/stopping/> Collection of stopping power data by H. Paul.
- [PIB68] T.E. Pierce, M. Blann, Phys. Rev. **173** (1968) 390.
- [PFÜ94] M. Pfützner et al., NIM. **B 86** (1994) 213.
- [RAV79] Ravn HL, Phys. Rep. **54** (1979) 201.
- [RIA00] <http://www.phy.anl.gov/ria/index.html> Homepage of the Rare isotope accelerator.
- [RIK00] <http://apw.riken.go.jp/rf/> Homepage of the RF Ion guide, M. Wada.
- [RIS03] http://www-aix.gsi.de/~wolle/EB_at_GSI/main.html Homepage of the Rare Isotope Spectroscopic Investigation at GSI, RISING.
- [ROT76] A. Roth, Vacuum technology, North-Holland Pub. Comp. (1976).
- [SAV03] G. Savard et. al., NIM **B 204** (2003) 582.
- [SAV04] G. Savard, *private communication*.
- [SCH94] C. Scheidenberger, Dissertation, *Abbremsung relativistischer Schwerionen im Energiebereich (100-1000) MeV/u*, II. Physikalisches Institut, Justus Liebig Universität Gießen (1994).
- [SCH98] C. Scheidenberger et al., NIM **B 142** (1998) 441.

- [SCH03] C. Scheidenberger, *private communication*.
- [SIG02] P. Sigmund, A. Schinner, NIM **B 195** (2002) 64.
- [SIG98] P. Sigmund, NIM **B 135** (1998) 1.
- [SMI53] F. M. Smith, W. Birnbaum and W. H. Barkas, Phys. Rev. 91 (1953) 765.
- [STE71] R.M. Sternheimer, R.F. Peierls, Phys. Rev. **B 3** (1971) 3681.
- [STE84] R.M. Sternheimer, et. al., Atomic Data and Nuclear Data Tables (1984) 261.
- [STE91] Herbert Stelzer, Nuclear Instruments and Methods **A 310** (1991) 103.
- [STO30] M. Stobbe, Ann. Phys. **7** (1930) 601.
- [SÜM90] K. Sümmerer, W. Bruechle, D. J. Morrissey, M. Schaedel, B. Szweryn, Yang Weifan, Phys. Rev. **C 42** (1990) 2546.
- [SÜM00] K. Sümmerer and B. Blank, Phys. Rev. **C 034607** (2000).
- [VIO85] U.E.Viola et al., Phys. Rev. **C31**, (1985) 1550.
- [WAG91] C.Wagemans, ed., *'The Nuclear Fission Process'*, CRC Press, London, 1991.
- [WEI00] H.Weick, Dissertation, *Einfluss der Umladung beim Abbremsen von Schwerionen im Energiebereich (100-1000) MeV/u*, II. Physikalisches Institut, Justus Liebig Universität Gießen (2000).
- [ZIE80] J.F Ziegler *'Handbook of Stopping Cross Sections for Energetic Ions in all Elements'* Bd. 5 of *'The Stopping and Range of Ions in Matter'*, Pergamon Press, New York (1980).
- [ZIE85] J.F. Ziegler, J.P. Biersack, U. Littmark *„The Stopping and Range of Ions in Solids“* Vol.1, Pergamon Press, New York (1985).

List of figures

- fig. 1-1 Chart of nuclides showing the proton number versus the number of neutrons. The colored squares represent radioactive nuclei sorted according to their dominant mode of decay: red = β^+ / EC, light blue = β , yellow = α , green = spontaneous fission and orange = proton emitters. The dotted lines indicate the proton and neutron drip lines, yet unexplored but the existence of these nuclei is expected from model calculations. _____ 8
- fig. 1-2 Schematic overview of the Super-conducting Fragment Separator, Super-FRS [GEI03], behind the projected heavy-ion synchrotron SIS 100/300 as proposed for the future international facility at GSI [CDR01]. It consists of a Pre-separator and a Main-separator delivering beams to three different experimental areas: the Ring Branch, the High-Energy branch, and the Low-Energy branch. _____ 9
- fig. 1-3 Schematic view of the energy buncher stage for the Low-Energy Branch of the planned Super-FRS at GSI. It consists of a magnetic dipole stage to spatially separate the exotic nuclei according to their momentum. The momentum spread is compensated by a specially shaped monoenergetic degrader by variation of its thickness and respective energy loss. It will serve many high precision experiments like γ -ray-, laser- and decay spectroscopy and Penning trap mass spectrometry. _____ 10
- fig. 2-1 The chart of nuclei, showing schematically the different production mechanisms for exotic nuclear beams: fusion (red), fission (green), and fragmentation (yellow). _____ 12
- fig. 2-2 The fission yield for ^{252}Cf versus the mass number. The two humps correspond to fragments around ^{108}Tc with 103 MeV and ^{143}Xe with 78 MeV. A source of this type has been used at Argonne to investigate the properties of the prototype gas cell [SAV03] described later. _____ 15
- fig. 2-3 Schematic illustration of the working principle of a Wien filter. The ions enter the perpendicular magnetic and electric field and only the ions with a certain velocity pass through. _____ 17
- fig. 2-4 Gas filled magnetic separator ENGE [ENG67]. Due to the collisions of the projectiles with the buffer gas, ions of a mean charge are focused to the same position on the focal plane. _____ 18
- fig. 2-5 Illustration of the Isotope Separation On-Line (ISOL) technique [RAV79]. The light projectiles (protons) impinge on a thick target producing the radioactive nuclei which are stopped in the target. By heating the target they are released, transported to an ion source where they are re-ionized for post acceleration. _____ 19
- fig. 2-6 Illustration of the In-flight separation technique. The heavy ion beam from an accelerator impinges on a thin target where the nuclei of interest are produced in projectile fragmentation reactions. They leave the target with almost the same velocity as the primary beam and thus need not to be reaccelerated for separation. The two-stage separation allows the system to be kept achromatic while separating in mass and charge. _____ 20
- fig. 2-7 Calculated separation performance of the fragment separator FRS at GSI for the production of ^{78}Ni . A ^{86}Kr beam from the SIS with 500 MeV/u impinges on the 1 g/cm² Be production target to produce ^{78}Ni in a fragmentation reaction. The first stage selects nuclei with the same m/q from the chart of nuclei and the second cut reduces the selection to ^{78}Ni only. _____ 21
- fig. 2-8 Illustration of the ion catcher technique. Behind a fragment separator a degrader system is used to slow down the projectiles far enough to finally stop them in a noble gas. Due to the high ionization potential of the noble gas a large fraction of the projectiles can leave the cell through a nozzle in a single ionized state. From there they can be further directed to experimental setups or post-accelerated. _____ 22
- fig. 2-9 Schematic illustration of Ion catchers being a link between ISOL and in-flight technique. The main objective herein is to provide low energy, high quality exotic beams, chemistry independent and in a time of a few ms. _____ 22
- fig. 2-10 NRC and REC cross sections for the K-shell electrons of Ni ions with an incident energy of 300 and 100 MeV/u versus Z_2 . _____ 26

fig. 2-11 The contributions of nuclear and electronic stopping of ^{58}Ni ions in Copper depending on the energy of the projectile. The red curve shows the sum of the two contributions. For ^{58}Ni the Bohr criterion is

$$Z_1^{2/3} v_0 \approx 0.23 \frac{\text{MeV}}{u}. \text{ This calculation was done using SRIM [ZIE85].} \quad 28$$

fig. 3-1 The FRS in achromatic standard ion-optical mode. The upper two plots show the beam envelope in x- and y-plane for an incident phase space of $\varepsilon = 20\pi \text{ nm} \cdot \text{mrad}$. The lower plot shows the dispersion curve for this standard achromatic mode. _____ 36

fig. 3-2 Positions of the Multi wire proportional chambers (MWPC) for the charge-state and energy-loss measurements. For the charge-state distribution measurements MWPC31 was used. The energy loss for the materials placed at F2 was determined at F3 and F4 using MWPC31 and MWPC41 respectively. _____ 37

fig. 3-3 Detector setup at the end of the FRS. The detectors mounted are MUSICs, MWPCs and scintillators. For the slowing down experiments the beam focus was on the MW41 just 590 mm behind the last quadrupole. For the range focusing experiment the focus was on the disc degrader mounted between the two MUSICs. _____ 37

fig. 3-4 Scheme of the multiple sampling ionization chamber (MUSIC). All measures are in mm. _____ 38

fig. 3-5 Schematic layout of a the multi wire proportional chamber [STE91]. _____ 39

fig. 3-6 Side view of the second focal area of the FRS (top) and a zoomed in top view of the target chamber at the bottom. The collimator C was placed at the focus, 2125 mm after the quadrupole. The distance between ladder 1 and 2 was 4 mm while the target ladder 3 was 275 mm away from the collimator and thus from the focal plane. Just before the targets and collimator chamber a MWPC for beam monitoring could be inserted. _____ 40

fig. 3-7 Charge state distribution at F3 for Ni at 50 MeV/u beam on a 41 mg/cm² Cu target. As the charge-state distribution is too wide to fit at once into the acceptance window of the FRS three B ρ -settings were taken. The percentage given for each peak is already the fraction normalized to the total intensity. _____ 41

fig. 3-8 This plot shows the charge-state distribution of a 50 MeV/u Ni beam behind Cu targets of different thickness. The measured charge-state ratios are plotted versus the beam energy behind the targets. The lines are to guide the eye. _____ 42

fig. 3-9 Mean charge of Ni projectiles as a function of energy behind all measured Cu targets. The solid line represents the prediction by the computer code GLOBAL [SCH98]. _____ 43

fig. 3-10 Schematic illustration of the energy loss measurement method. Without target (left) the primary beam with a magnetic rigidity B ρ_0 is centered in x direction on the MWPC while a beam component with the rigidity B ρ would be out of the acceptance. With a target and after scaling the magnets (right) the beam with the magnetic rigidity B ρ is centered except for a little displacement Δx . _____ 44

fig. 3-11 Calibration points for B ρ determined via the measured currents versus BL $_0$ and a 2nd order polynomial fit function. _____ 45

fig. 3-12 The difference between the measured energy loss ΔE_{exp} and the predicted energy loss by the computer code ATIMA ΔE_{ATIMA} as a function of the energy after the targets for the three different methods to determine B ρ . _____ 46

fig. 3-13 Emergent energy of ^{58}Ni ions with 50 MeV/u incident energy as a function of the Cu target thickness. The solid line shows a linear fit to the data points. _____ 47

fig. 3-14 The same values for the energy of ^{58}Ni with 50 MeV/u incident energy versus the Cu target thickness as in fig. 3-13. But this time after subtraction of the theoretical prediction by ATIMA. Also included a linear approximation function and the error of this linear approximation. _____ 48

fig. 3-15 Measured width profile of the ^{58}Ni beam at F4 with an initial energy of 50 MeV/u with (green) and without (red) a 76 mg/cm² Cu target at F2. _____ 49

- fig. 3-16 Gauss fit of the above case with the Cu target at F2. The background on the left (low energy side) is due to ions striking the collimator. The background to the right has the same origin yet belongs to the next charge state. Both contributions are interpolated due to eq. 3-17 and subtracted for the fit. _____ 50
- fig. 3-17 Variance of the energy straggling σ of Ni ions in various beryllium targets versus the energy loss in these targets for four different initial beam energies. The solid lines show the prediction by ATIMA. _____ 53
- fig. 3-18 Variance of the energy straggling σ of Ni ions in various carbon targets versus the energy loss in these targets for four different initial beam energies. The solid lines show the prediction by ATIMA. _____ 53
- fig. 3-19 Variance of the energy straggling σ of Ni ions in various aluminum targets versus the energy loss in these targets for four different initial beam energies. The solid lines show the prediction by ATIMA. _____ 54
- fig. 3-20 Variance of the energy straggling σ of Ni ions in various copper targets versus the energy loss in these targets for four different initial beam energies. The solid lines show the prediction by ATIMA. _____ 54
- fig. 3-21 Variance of the energy straggling σ of Ni ions in various silver targets versus the energy loss in these targets for four different initial beam energies. The solid lines show the prediction by ATIMA. _____ 55
- fig. 3-22 Variance of the energy straggling σ of Ni ions in various gold targets versus the energy loss in these targets for four different initial beam energies. The solid lines show the prediction by ATIMA. _____ 55
- fig. 3-23 Calculated range straggling σ_R of ^{56}Ni ions in helium for 1% initial momentum spread (dashed line) and 0.1% initial momentum spread (dashed dotted line) versus the beam energy E_{in} using the computer code MOCADI [IWA97]. The straight solid line corresponds to a stopping volume of a 1.25 m long gas cell filled with helium at 400 mbar corresponding to 8.9 mg/cm^2 . _____ 57
- fig. 3-24 Calculated yield of bare ions after the intermediate aluminium degrader which undergo no nuclear reactions during the stopping process up to the final focus as a function of their exit energy. Transmission through the second stage of the FRS is not included in the calculation. _____ 58
- fig. 3-25 Illustration of the range focusing principle. The projectiles dispersed in momentum enter a magnetic dipole stage which spatially separates the projectiles in x-direction according to their momentum difference δp . The monoenergetic degrader [GEI89] compensates the momentum distribution by adjusting the thickness via the degrader angle α and therefore the energy loss according to the dispersion of the magnetic dipole. _____ 59
- fig. 3-26 Three dimensional technical drawing of the monoenergetic degrader. The two widdershins rotatable discs are held in place by four wheels each to avoid tilting of the discs. Around the discs there are teeth in order to drive them with cock wheels via a stepper motor drive. _____ 60
- fig. 3-27 The prototype degrader system as used for the experiment (top) and schematically (bottom). This two stage degrader system consists of a degrader to vary the angle α by rotating two wedge shaped discs by the angle β , and a degrader to adjust the total thickness d . _____ 61
- fig. 3-28 Ion optical setting (upper) and dispersion plot (lower) used for the range focusing experiment on ^{54}Co and ^{56}Ni . The dispersion function shows the mode of the FRS and reached a value of $6.84 \text{ cm}/\%$ from F2 to F4. _____ 62
- fig. 3-29 Fragments yield at F3 versus the x-position with ^{56}Ni centered according to LISE [LIS03] simulation. The vertical lines indicate the slit position to cut off none $A/Z=2$ fragments. The reason for the lighter $A/Z=2$ fragments not being centered is due to the different energy loss in the target. _____ 63
- fig. 3-30 Schematic view of the experimental setup for the range focusing measurements. Two Multi Sampling Ionization Chambers (MUSIC) were used for particle identification and counting their number N_1 and N_2 respectively. In between the MUSIC detectors the two stage degrader system to vary the angle α and the total thickness d is located as well as the slits to select the $A/Z=2$ fragments _____ 63
- fig. 3-31 Yield of $A/Z=2$ fragments at F4 versus the x-position. 88.5% of ^{56}Ni are passing the slits, while for the not centered ones the losses are larger. _____ 64

<i>fig. 3-32</i> Counts in the 1 st music detector as a function of energy deposition. A gate is set to select a certain species. In this case ⁵⁶ Ni was selected. _____	65
<i>fig. 3-33</i> Counts in the 2 nd music detector as a function of energy deposition only counting those ions which were previously identified and gated in the 1 st music. _____	65
<i>fig. 3-34</i> NDC obtained using three Anodes of the 2 nd music varying the degrader thickness Δx for one fixed degrader angle α . The drawn lines are fits with the error function to the data points. _____	66
<i>fig. 3-35</i> The derivatives of the NDC's shown in <i>fig. 3-34</i> as a measure for the Gaussian range distribution of the stopped fragments. _____	67
<i>fig. 3-36</i> Range focusing of ⁵⁶ Ni fragments. The upper graph shows the error-function fit to the number distance curves measured for a focusing angle of $\alpha=6.24$ mrad (solid line) and with $\alpha=-4.8$ mrad (dashed line). The lower graph shows the corresponding range distributions. The gain in range straggling in the case of ⁵⁶ Ni is almost a factor of four. _____	68
<i>fig. 4-1</i> Measured mean charge of ⁵⁸ Ni versus the Energy E after the targets (top) and measured mean charge of ¹³⁶ Xe versus the Energy E after the targets. The lines are drawn to guide the eye only. _____	69
<i>fig. 4-2</i> Measured mean charge of ⁵⁸ Ni divided by the prediction of the Pierce and Blann formula versus the Energy E_{out} after the target. _____	70
<i>fig. 4-3</i> Measured mean charge of ¹³⁶ Xe divided by the prediction of the Pierce and Blann formula versus the Energy E. _____	71
<i>fig. 4-4</i> Measured mean charge of ⁵⁸ Ni divided by the prediction of the computer code Global versus the energy E. _____	71
<i>fig. 4-5</i> Measured mean charge of ¹³⁶ Xe divided by the prediction of the computer code Global versus the energy E. _____	72
<i>fig. 4-6</i> The measured stopping power of ⁵⁸ Ni projectiles versus the energy. The green line is the prediction by SRIM 2003 and the blue line the prediction by ATIMA down to 30 MeV/u. The black data points are taken from the collection of stopping-power measurements by Helmut Paul [PAU03]. The red data points are the ones taken from this work. _____	73
<i>fig. 4-7</i> The measured stopping power of ¹³² Xe projectiles versus the energy. The green line is the prediction by SRIM 2003 and the blue line the prediction by ATIMA down to 30 MeV/u. The black data points are taken from the collection of stopping-power measurements by Helmut Paul [PAU03]. The red data points are the ones taken from this work. _____	74
<i>fig. 4-8</i> Measured stopping power of ⁵⁸ Ni normalized to the prediction of ATIMA plotted versus the energy. For comparison, also shown are the predictions of Ziegler and PASS. _____	75
<i>fig. 4-9</i> Measured stopping power of ¹³⁶ Xe normalized to the prediction of ATIMA versus the energy. For comparison also shown the predictions of Ziegler and PASS. _____	76
<i>fig. 4-10</i> Stopping power of ¹³⁶ Xe calculated with ATIMA with partial stopping powers (red) and using the Pierce and Blann formula (blue) for the mean charge versus Z_2 of the target normalized to the experimental values. There is a plot for each initial beam energy. _____	77
<i>fig. 4-11</i> Measured range straggling σ_R for ⁵⁶ Ni fragments using different degrader angles α . For comparison the primary beam of ⁵⁸ Ni is shown as well as a prediction by the computer code MOCADI. _____	78
<i>fig. 4-12</i> Measured range straggling σ_R for ⁵⁴ Co fragments using different degrader angles α . For comparison the primary beam of ⁵⁸ Ni is shown as well as a prediction by the computer code MOCADI. _____	79
<i>fig. 5-1</i> Schematic picture of the FRS-Ion Catcher setup. The high-energy ions delivered from the FRS are slowed down and energy bunched in the degrader system. They eventually enter a gas cell where they are stopped and, by means of applied AC and DC fields, directed and dragged towards the gas cell exit nozzle. The	

high gas flow pushes the ions through the nozzle into the extraction RFQ where they are separated from the gas by differential pumping. The next stage, the Multi-RFQ, serves as a distribution device to three different experimental outlets and as a further differential pumping stage. _____ 80

fig. 5-2 Illustration of the working principle of the FRS-IC gas cell. Over the entire length a DC field gradient is applied to drag the ions toward the exit nozzle. An additional AC field is used to repel the ions from the cell electrode surfaces, a process referred to as RF-focusing. The gas flow, being strongest at the exit nozzle, also drags the ions and finally pushes them through the nozzle. The bottom picture illustrates the net force an ion sees inside the cell. _____ 81

fig. 5-3 Schematic drawing of the FRS-Ion Catcher and extraction RFQ section. The ions enter the cell on the right through the window (blue) which is mounted off-center. Below the window is the pumping port used during bake out. The cell body itself is 1.4 m long. At the left is the vacuum chamber for the extraction RFQ. The green box around the cell is the high voltage case installed for safety reasons. _____ 82

fig. 5-4 Photo of the gas cell after assembly at Argonne. At the back of the gas cell is the entrance window (hidden from view on the right) and in the front is the cone with the exit nozzle (shown on the left). _____ 83

fig. 5-5 The exit nozzle cone of the gas cell. It consists of 278 electrode rings with varying diameter. _____ 84

fig. 5-6 The experimental setup for the gas cell tests at Argonne. The ions enter the extraction RFQ at the right side of this figure behind the gas cell which is not shown here. In this first section the ions are retained by the RFQ field while the gas is removed by differential pumping. The 2nd section of the RFQ has a linear Paul trap for accumulating and bunching the ions. After the Paul trap is an acceleration column with a 1.5 m drift tube for time of flight mass measurements. At the end of the drift tube are micro-channel plates to measure the ions' TOF and a Si detector to monitor the β -activity. _____ 85

fig. 5-7 Photo of the gas cell setup at Argonne. The gas cell shown at the right is inside a HV-cage which is open in this picture. _____ 85

fig. 5-8 A photo of the two-stage purification system during assembly at Leuven. The first stage is a cold trap to freeze out most of the contaminants from the Helium buffer gas. The second stage is a commercially available Mono-Torr purifier. The challenge and the high costs herein are due to the high flow rates of around 25 slpm. 86

fig. 5-9 The roots blower pump and the transfer line. The transfer line has a bellows on each side to decouple the experimental setup from the vibrations of the pump. Just above the pump are the water-cooled baffle and a big interlock valve to shut off the pump in case of a failure. _____ 87

fig. 5-10 Performance test of the roots blower pump. The plot shows the pressure reached in a chamber with a nozzle of varying diameter. In all cases the inlet pressure was 1 bar. The exit nozzle was represented by a needle valve and was roughly adjusted to the corresponding nozzle sizes up to a 1 mm diameter. Above this value, a flange replaced the needle valve and the exit nozzle was represented by drilled holes of different diameters. Even though this was just a rough test, one can clearly see that for a gas cell pressure of 750 Torr or 1 bar, a 1.5 mm nozzle allows for a pressure in the extraction RFQ below 1 Torr. _____ 88

fig. 5-11 A rest gas analysis of a vacuum chamber directly attached to the roots blower pump. The plot shows the abundance of masses from 0 to 100 u with a sensitivity of 10^{-11} mbar. The base pressure in the chamber was $1.7 \cdot 10^{-4}$ mbar. _____ 89

fig. 5-12 The S4 area behind the FRS. This is a possible scheme to fit the FRS-IC setup [FRS03] into the S4 area together with RISING [RIS03]. Behind the FRS there is one support table to place a MUSIC detector for identification and the degrader setup for range focusing. At the place where normally the RISING setup is placed the FRS-IC setup can be put in with the crane and beside the roots blower pumping station. For this the RISING detectors have to be moved apart on a rail system in the floor. _____ 90

fig. 5-13 Schematic overview of the planned FRS ion catcher set up. After the degraders for range focusing the ions are stopped in the gas cell and extracted into the extraction RFQ. Behind this is a 3-way RFQ system which allows the ions to be distributed to three different experimental setups: a beam monitor and diagnostics section, a tape station for decay studies, and an orthogonal time of flight mass spectrometer (Ortho-TOF-MS). _____ 90

fig. 5-14 A schematic picture of the orthogonal time of flight mass spectrometer (Ortho-TOF-MS) developed at the JLU in Giessen. _____ 91

fig. 5-15 The foreseen tape station provided by KU Leuven for the decay studies. _____ 92

Acknowledgements

First of all I thank Professor Hans Geissel for the opportunity to join the FRS group and especially for these exciting experiments.

I thank Professor Guy Savard for being the one who got me into the whole gas cell and stopping of ions business in the first place. It was always a pleasure and very instructive to work with and for him. In this context I also would like to use this opportunity to apologize for the unfortunate trouble I caused him.

I'd like to thank the post-doctorial staff of the KP II for fruitful discussions and nudges in the right direction when I was thick or slow. I thank especially Dr. Christoph Scheidenberger and Dr. Helmut Weick for their help in getting and analyzing the slowing down data, Dr. Jens Stadlmann for all his help concerning computers, Dr. Fairouz Hammache, Dr. Faouzi Attalah, Dr. Maurico Portillo and David Boutin for a great but too short of a time together in the office and outside. And also many thanks to all other members of KP II which are too many to name them all.

The group of people which are essential for any experiment at the FRS I especially mention here. These are the technicians at the FRS (Adolf Brünle, Karl-Heinz Behr and Charly Burkhard) and the target lab staff. Talking about target preparations, experimental setups, the degrader system, gas supplies and much more it would all not go as smoothly without them.

Apart from work, but for company and many good times at GSI are so many people I can not name them all here but there is Dr. Vladimir Chichkine who deserves some special gratitude for many good Binding times in the GSI Lobby! And I'd like to thank Dr. Hidemi Ogawa for many good lectures in the Japanese language in return for good lectures of Bavarian culture! A very special thanks goes to Dr. Denis Bertini whom I'm very grateful having him for a real friend and companion.

I also have to thank the Bundesanstalt für Arbeit for their unselfish support, allowing me to finish my PhD in peace and with a roof over my head. Last but not least I would like to thank my parents for their mental and financial support whenever it was necessary.

Thank you very much, vielen Dank, merci beaucoup, domo arigato!